Optical Limits in Left-Handed Media

Philip Charles Ingrey, BEng
Division of Applied Mathematics

School of Mathematical Sciences
University of Nottingham

Thesis submitted to The University of Nottingham for the degree of Doctor of Philosophy

April 2010

Abstract

This thesis determines the response of Left-Handed Media (LHM) to surface effects.

A LHM half-space with a roughened interface, modelled by a graded index boundary, is shown to give rise to an analytical solution for the propagation of electromagnetic radiation through this inhomogeneous layer. Significant field localization is generated within the layer, caused by the coherent superposition of evanescent waves. The localization is shown to greatly deteriorate transmission when losses are present. The addition of a second interface to the LHM, creating a perfect lens configuration, allows for the exploration of evanescent mode propagation through a perfect lens with roughened boundaries. The effects of the field localisations at the boundaries serves to diminish the resolving capability of the lens. Specifically the layers produce an effect that is qualitatively similar to nonlinearly enhanced dissipation.

Ray-optics is used to analyse negative refraction through a roughened interface, prescribed by Gaussian statistics. This shows that rays can focus at smaller distances from the interface due to the negative refractive effects. Moreover, a new reflection mechanism is shown to exist for LHM. Consequently an impedance matched configuration involving LHM (such as the perfect lens) with a roughened interface can still display reflection.

A physical-optics approach is used to determine the mean intensity and fluctuations of a wave passing into a half-space of LHM through a roughened interface in two ways. Firstly through the perturbation analysis of Rice theory which shows that the scattered field evolves from a real Gaussian process near the surface into a complex Gaussian process as distance into the second media increases. Secondly through large-scale Monte-Carlo simulations that show that illuminating a roughened interface between air and a LHM produces a regime for enhanced focussing of light close to the boundary, generating caustics that are brighter, fluctuate more, and cause Gaussian speckle at distances closer to the interface than in right-handed matter.

Acknowledgements

I would like to thank my academic supervisors Keith Hopcraft and Eric Jakeman: Keith for the numerous discussions and for never being afraid to speak his mind, without it this thesis would have been infinitely worse off. And to Eric whose comprehensive and far-reaching knowledge has helped guide and inform the course of this PhD. I also thank Oliver French for invaluable discussions and input throughout. I would like to acknowledge the EPSRC for the funding of this project. I also give thanks to the following: Mum and Dad for their unconditional support throughout the years; Friends and family - too numerous to mention, but that have filled my days with laughter; God for the grace that has and will see me through and to Antonia without whom I would be completely lost - for any shred of sanity I have left is due to her. Finally to those who have frequented the tea room, past and present, for the varied and sometimes bizarre conversations that have never failed to entertain.

"Science is wonderfully equipped to answer the question 'How?' but it gets terribly confused when you ask the question 'Why?'" - Erwin Chargaff

Contents

Chapter 1

Introduction

1.1 Motivation

Having been investigated for over a millennia the subject of optics is one of the most ancient and well researched of any scientific area. So it is somewhat surprising that a completely new avenue of exploration could open up after all this time; yet that is the case. With two papers [1, 2] the field of negative index media (NIM) was born. The interesting fact is that it has not involved an overhaul of classical optics: Snell's law and Maxwell's equations remain unchanged, the problem has been lying dormant for hundreds of years. Yet the technology to realise these solutions, and therefore the impetus to investigate the area, has only become within our grasp during the last decade.

Negative index media, or left-handed media (LHM), are substances which have simultaneously negative electric permittivity, ϵ, and magnetic permeability, μ, over a range of frequencies [1, 2]. Causality then leads LHM to have a negative effective refractive index, n, within that frequency range. Using the science of metamaterials, devices which derive their material properties from man-made constituent elements rather than their atomic structure, has enabled LHM to be manufactured and their novel optical properties have been experimentally demonstrated at ever increasing frequencies [3, 4, 5, 6]. The pivotal result pertaining to LHM, as detailed in [2], is that a slab of the material acts as a lens which both brings to focus the propagating modes and also restores the evanescent components of the source, in contrast to a conventional lens where only the propagating modes contribute to the image. Such a configuration of LHM has been named a "Perfect Lens" due to the perfect nature of the image obtained.

However, this faultless lens is highly singular in its operation: varying any of a multitude of parameters introduces imperfections into its operation. It is not the case, as some early

on argued, that any deviation leads to sub-diffraction imaging [7]; instead the resolution decreases smoothly, though not necessarily slowly, as the conditions deviate from optimal. This thesis focuses on the investigation and quantification of some limits upon the optics of LHM, namely the constraints of non-ideal boundaries and their effects on the perfect lens' performance.

1.1.1 Inception: The concept of left-handed media

In 1968 Veselago published a mathematical paper detailing the theoretical results of a medium having simultaneously negative ϵ and μ [1]. The paper begins with the definition of the refractive index of a medium

$$n^2 = \epsilon\mu \tag{1.1.1}$$

with the sign of n chosen so that electromagnetic field within the medium decays through losses at infinity; a lossless medium can be interpreted as a limiting case of a lossy one. It will be shown that when the real parts of ϵ and μ are simultaneously negative, with losses incorporated, causality forces the choice of n such that it has a negative real part. Firstly considering the permittivity ϵ, then clearly the positive square root is taken whenever ϵ is positive. As ϵ decreases its square root approaches a branch point at $\epsilon = 0$. However, all media contain some form of loss which manifest themselves in the imaginary part of ϵ, with $\mathrm{Im}(\epsilon) > 0$, forcing the path above the branch point giving the square root of a negative ϵ as $i\left(-\epsilon\right)^{1/2}$. A similar reasoning gives the square root of μ to be $i\left(-\mu\right)^{1/2}$ when $\mu < 0$. Combining these

$$n = i^2\sqrt{-\epsilon}\sqrt{-\mu} = -\sqrt{\epsilon\mu}, \quad \epsilon < 0,\, \mu < 0. \tag{1.1.2}$$

For plane waves in a homogeneous and isotropic medium with an electric field of the form $\mathbf{E}(\mathbf{r}, t) = \mathbf{E}_0 \exp\left(i\left(\mathbf{k}\cdot\mathbf{r} - \omega t\right)\right)$, Maxwell's equations reduce to the following (in SI units):

$$\mathbf{k}\times\mathbf{E} = \omega\mu\mu_0\mathbf{H}, \tag{1.1.3a}$$

$$\mathbf{k}\times\mathbf{H} = -\omega\epsilon\epsilon_0\mathbf{E}, \tag{1.1.3b}$$

$$\mathbf{k}\cdot\mathbf{D} = 0, \tag{1.1.3c}$$

$$\mathbf{k}\cdot\mathbf{B} = 0, \tag{1.1.3d}$$

where $\mathbf{B}$ is the magnetic field, $\mathbf{k}$ the wavevector, $\mathbf{D} = \epsilon\epsilon_0\mathbf{E}$ and $\mathbf{B} = \mu\mu_0\mathbf{H}$. The initial two equations demonstrate that when $\epsilon > 0$ and $\mu > 0$ the set of vectors $\{\mathbf{k}, \mathbf{E}, \mathbf{H}\}$ form

a right-handed triad, conversely when $\epsilon < 0$ and $\mu < 0$ the triplet form a left-handed set leading to the terminology "left-handed media" or LHM. Strictly the set $\{\mathbf{k}, \mathbf{E}, \mathbf{H}\}$ being left-handed does not have to imply a negative refractive index, however the term "left-handed media" has become synonymous with negative refracting media. Within this thesis wherever the term left-handed media is used, a negative refractive index is implicit. A further characteristic of LHM involves the energy flow within a medium, which can be measured by the Poynting vector [8]:

$$\mathbf{S} = \mathbf{E} \times \mathbf{H}. \tag{1.1.4}$$

It can be seen that if the medium is left-handed then the energy flow, $\mathbf{S}$, and wavevector, $\mathbf{k}$, are anti-parallel; this leads to the appearance of waves travelling 'backwards' within LHM. Before the creation of LHM the direction of energy flow and the wavevector have always been parallel in bulk media, this has lead to the occasional misunderstanding about the correct application of causality with LHM and unfortunately still does to this day. For example in a recent paper by Ferrari *et al* [9] it is argued that negative refraction cannot occur, partially due to the following reasoning: on writing the wavevector as $\mathbf{k} = \mathbf{k}' + i\mathbf{k}''$ with $\mathbf{k}'$ and $\mathbf{k}''$ being real vectors, Ferrari states for electromagnetic waves to be "progressively attenuated" by dissipation requires that

$$\mathbf{k}' \cdot \mathbf{k}'' > 0. \tag{1.1.5}$$

It is correctly argued that if the medium is a LHM then

$$2\,\mathbf{k}' \cdot \mathbf{k}'' = \mathrm{Im}(\mathbf{k} \cdot \mathbf{k}) = \mathrm{Im}\big(n^2 k_0^2\big) = k_0^2 \left(\epsilon'\mu'' + \epsilon''\mu'\right) < 0 \tag{1.1.6}$$

as the causal choices when $\epsilon' < 0$ and $\mu' < 0$ force $\epsilon'' > 0$ and $\mu'' > 0$, with $\epsilon = \epsilon' + i\epsilon''$ and $\mu = \mu' + i\mu''$. However the propensity of a medium should be to attenuate along the direction of energy transfer which in double-negative medium, as seen above, is anti-parallel to the the direction of the wavevector. Therefore the correct causal constraint for LHM is not (1.1.5) but rather

$$\mathbf{k}' \cdot \mathbf{k}'' < 0 \tag{1.1.7}$$

in complete agreement with (1.1.6).

Other effects detailed by Veselago are that the Doppler shift is reversed within LHM and also that at a boundary between conventional "right-handed media", RHM, and LHM that negative-refractive would occur (these media still obey Snell's law). Veselago also showed

that such a medium would have to be dispersive and as a result could only sustain this negative refractive index for a finite band of frequencies. At the time of its writing the paper had little impact as there was no viable way to manufacture these materials and the paper was viewed as a interesting mathematical oddity.

1.1.2 Formation: The genesis of perfect lensing

In October 2000 the seminal paper in this area was published by Pendry [2]. This paper highlighted two key points. The first described how a slab of LHM with $\epsilon = \mu = n = -1$ could be used as a lens through the negative refraction of light, c.f. Fig. 1.1. But beyond this, the paper also shows a very interesting result: for an evanescent wave incident upon the lens, the evanescent wave that is generated on the far side of the lens is *amplified* when compared with the evanescent wave entering the lens. Comparing this to a conventional lens where evanescent waves inexorably decay throughout the lens such that they are virtually undetectable on the far side of the lens highlights the importance of the discovery. This amplification does not violate causality as evanescent waves do not themselves transmit energy but as Pendry himself states "nevertheless it is a surprising result" [2]. This result occurs through the consideration of the path an evanescent wave takes through the lens: each time an evanescent wave reaches an interface there is a transmitted and reflected component, with the sign of the exponential chosen so that each decays away from the interface. By summing the multiple reflections of an evanescent wave within a slab of general ϵ and μ and then taking the limit as both tend to -1 the transmission coefficient for the s and $p-$wave states are found to be:

$$\lim_{\substack{\epsilon\to-1\\ \mu\to-1}} T_s = \lim_{\substack{\epsilon\to-1\\ \mu\to-1}} \frac{t_s t_s' \exp(ik_z' d)}{1 - {r_s'}^2 \exp(2ik_z' d)} = \exp(-ik_z' d) = \exp(-ik_z d), \tag{1.1.8a}$$

$$\lim_{\substack{\epsilon\to-1\\ \mu\to-1}} T_p = \lim_{\substack{\epsilon\to-1\\ \mu\to-1}} \frac{t_p t_p' \exp(ik_z' d)}{1 - {r_p'}^2 \exp(2ik_z' d)} = \exp(-ik_z' d) = \exp(-ik_z d), \tag{1.1.8b}$$

where d is the slab thickness, r and t are the reflection and transmission coefficients from a vacuum into the medium, with r' and t' being the similar coefficients from the medium into vacuum, the subscripts denote the s and p-polarised waves. Here k_z is the component of the wave vector perpendicular to the slab in vacuum, taken to be a positive imaginary number such that the wave decays as $z \to \infty$. Similarly k_z' is the component of the wave vector within the slab, also taken to be a positive imaginary number so that if the second interface was not present (a LHM half-space) then the evanescent wave within the medium

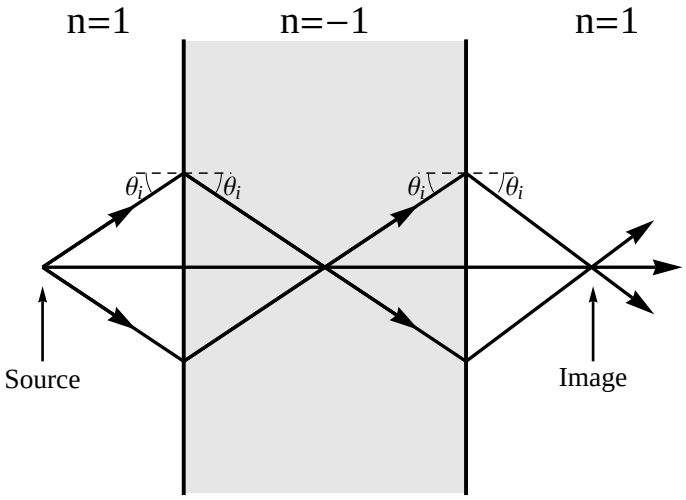

Figure 1.1: Ray tracing within a slab of negative refracting media with $n = -1$ in a perfect lens configuration, that is one where the slab thickness is twice the distance from the source to the slab. With this structure the source is perfectly reconstructed at the second image on the other side of the slab.

would still decay as $z \to \infty$, in accord with causal considerations. With this view-point it is clear that the infinite sum of reflected evanescent wave within the lens gives rise to a large evanescent wave decaying from the second interface towards the first, rather than an evanescent wave growing from the first to the second interface.

The 'amplification' of the evanescent waves by a factor of $\exp(-ik_z d)$ and the negative refraction of propagating modes is such that if a slab width of $2l$ is placed a distance l from a source of electromagnetic radiation then there is an image formed at a distance l on the far side of the LHM, c.f. Fig. 1.1 and Fig. 1.2. This image is different to that formed by a conventional diffraction limited lens where the image has no near-field (evanescent contributions). Instead the image formed by a LHM lens restores both the near- and far-field components of the electromagnetic field, perfectly reproducing the source. As such the term "perfect-lens" was coined for LHM used in this configuration. With later papers this effect can be seen in a more profound way - that the LHM optically annihilates the space between the source and image [10].

The second key part of Pendry's paper was to suggest "a practical scheme for implementing such a lens" [2]. Pendry's paper was quite counter-intuitive and as such the scientific community barraged the ideas with questions and arguments against perfect-lens theory. The most worthy of note are 't Hooft's comment on the paper (with Pendry's response) [11, 12], a paper by Garcia and Nieto-Vesperinas [7] and later another paper by

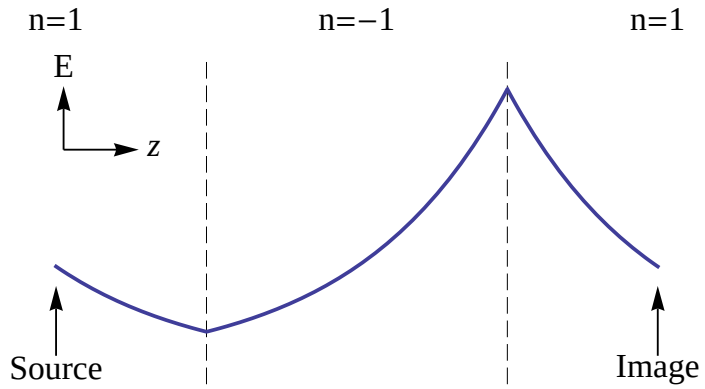

Figure 1.2: An example field profile for an evanescent mode propagating through a perfect lens.

Nieto-Vesperinas [13].

The arguments mostly centered around the application of causality constraints [10]. 't Hooft's arguments centered around the choice of sign for the wave vector across the interface and Garcia *et al* argued that any absorption would make a decaying evanescent wave dominate over the growing evanescent wave destroying the perfect imaging. By the time of publication of Nieto-Vesperinas' paper in 2004 [13] attitudes had started to soften towards the feasibility of perfect-lensing, partly fuelled by the incoming experimental verifications of negative refraction [14, 15, 16] (although this was refuted for a time [17]). Nieto-Vesperinas focused more on the resolution of a perfect lens in the presence of absorption rather than trying to attack the idea of negative-refraction per se.

1.1.3 Realisation: Creating viable doubly negative media

Over time the causality constraints in Pendry's original paper where shown to be the correct choice [18, 19]. From this juncture on the focus shifted onto applications of LHM, their manufacture and analyses of their constraints rather than discussions of their existence.

Since the 1950s artificial dielectrics have been manufactured to have properties differing from those of naturally occuring dielectrics [20], made by the construction of regular arrays of elements much smaller than the wavelength of interest e.g. for microwaves these can be of the order of centimeters, while for optical wavelengths tens of nanometers are required. An incoming wave cannot resolve these fine-scale sub-wavelength effects and averages over the inhomogeneities to perceive an "effective medium" [21]. The appellation "metamaterials" has replaced "artificial dielectrics" and has become the encompassing term for all media manufactured in this way. Using the techniques of metamaterial fabrication, dielectrics can

be created which have a negative effective average for ϵ and μ, and therefore act as a LHM for radiation of suitable wavelength. The material science problem is now to construct LHM at higher frequencies, create broadband negative refraction and lower losses within the media. A good report on the situation up until early 2007 is given by Soukoulis [3] ending with the work by Dolling that achieved negative refraction at the edge of the visible spectrum (780nm) [22]. Since then there has been work claiming to have negative refraction in the green/blue part of the visible spectrum ($\approx$ 514nm) [4].

In 2008 Zhang's research group at the University of California created a negatively refracting bulk metamaterial, that is to say a material which demonstrates negative-refraction in three-dimensions. Up to this point all experimental results had used metamaterials placed in two-dimensional waveguides so as to nullify the third dimension of the metamaterial used. Zhang's group simultaneously released two papers which confront the problem in different ways. The first [5] uses arrays of nanowires where the diameter and spacing between the nanowires controls the effective refractive index, in the paper a bulk metamaterial demonstrating negative refraction at 660nm with a wavelength range of 120nm is shown. The second [6] uses stacks of a fishnet structure to similar effect, giving negative refraction at 1500nm with a 300nm range in wavelength.

1.1.4 Digression: Transformation optics

Before progressing it is interesting to consider the sister field of transformation optics, another burgeoning field developed at a similar time. Metamaterials allow for new, and previously impossible designs to be imagined and one very powerful tool is for realising concepts is transformation optics. This method takes as its input a specified coordinate transformation in optical space and returns the required anisotropy in $\underline{\underline{\epsilon}}$ and $\underline{\underline{\mu}}$, possibly (but not necessarily) involving LHM. The usefulness of this method is demonstrated in Pendry's first paper on cloaking where it is used to render an area invisible to an outside observer [23]. After this paper the area of cloaking captivated the scientific community's and public's imagination. A myriad of shapes now have cloaking designs: as well as the original sphere [23], there is a more general paper on coordinate transformations which details a square cloak [24], alongside these are cloaks for toroids [25], elliptic cylinders [26], cloaks with a twin cavity [27] and general two dimensional cloaks [28, 29].

In each case the material requirements are exacting, e.g. [30, 31], such that their manufacture is an ongoing materials engineering problem. The first experimental testing of the

cloak used simplified material parameters to avoid the large parameter values needed in the original design [32], but this simplification can never lead to a perfect cloak [33], although other incremental improvements to this design have also been suggested [34].

The experiments into cloaking now revolve around the ground-plane cloak [35] which conceals an object on a flat conducting plane. This design is advantageous as it does not require the singular values of the spherical cloak and, under set conditions, the cloak can be made isotropic: a major boon for manufacturing. Shortly after the publication of the theoretical paper, experimental confirmation was made in the range 13 to 16 GHz [36], then in the range 1400-1800nm [37], the closest cloaking has been to working in the visible spectrum.

Transformation Optics has also inspired many other interesting designs: superantenna [38], tunneling waves through open space [39], electromagnetic wormholes and virtual magnetic monopoles [40], steerable antenna [41], beam splitters [42], cloaking at a distance [43] and inserting the illusion of a secondary object [44], to name but a few.

1.1.5 Limitations

Although not as numerous, various useful LHM applications have also surfaced [45, 46, 47, 48]. However, for every paper that is published on an application of LHM there seems to be corresponding paper that shows limitations on the implementation of these devices, for example that the surfaces must be highly smooth [49, 50] or that there must be no deformation to a boundary [51], *inter alia*. Here two limitations are highlighted, firstly that left-handed media are necessarily dispersive [1], which is demonstrated through consideration of the total energy per unit volume, W, within a system [52]:

$$W = M\left(\frac{\partial(\epsilon\omega)}{\partial\omega}\left|E\right|^2 + \frac{\partial(\mu\omega)}{\partial\omega}\left|H\right|^2\right). \tag{1.1.9}$$

where M is a positive constant dependent on the system of units used [52, 53]. In order to ensure that W be positive it is required that at least one of the conditions

$$\frac{\partial(\epsilon\omega)}{\partial\omega} > 0 \quad \text{or} \quad \frac{\partial(\mu\omega)}{\partial\omega} > 0 \tag{1.1.10}$$

is true for each frequency, ω. This does not preclude doubly negative media but introduces a frequency dependence into the permittivity and permeability of the media.

More recently it was shown by French *et al* [54] that a slab with lossless permittivity and permeability and a refractive index of $n = -1$ can still suffer from diminished resolution.

That analysis takes

$$\epsilon = \frac{-1}{1+\delta} \quad \text{and} \quad \mu = -(1+\delta), \tag{1.1.11}$$

where δ is a real but not necessarily small parameter. Under these conditions the refractive index is unperturbed from -1 whilst ϵ and μ can deviate greatly from unity. Within this imperfect, but lossless, situation it is found that the resolution converges logarithmically, with δ, to that of the perfect lens. This result shows that even if losses can be controlled, e.g. by introducing gain into the system, the constraints upon the material parameters are still exacting. The perfect lens is singular in terms of its physical operation and is consequently very sensitive to any abberation that moves it away from that singularity.

1.1.6 Conclusions

Metamaterials and in particular LHM offer a wealth of previously unobtainable applications, but understanding the limitations and finding how to minimize these effects will be vital for attaining their full potential. The limitations detailed above have mainly dealt with the material imperfections of a LHM device in a perfect lens configuration. However, this is only one aspect of the problem. Creating a material with perfectly smooth, planar, boundaries is impossible; roughness, perturbations and deformations of any surface is unavoidable.

This thesis focuses on the latter problem, modelling surface effects to understand the interplay between surface deformation and doubly-negative media to ascertain if negative refraction is a robust and resilient effect, and if not, to quantify the extent of the degradation to the resolution. This will be done, in two ways. The first is by modelling the surface as a transitional effective medium between right- and left-handed media for which an exact solution to Maxwell's equations can be found. The second is to model the interface by a random process which can be analysed using either the geometrical- or physical-optics approximations.

1.2 Thesis Outline

The overall aim of this thesis is to determine the response of LHM, and specifically the perfect lens configuration, to imperfect boundaries. This will be done in the first instance though an analytical graded-index (GRIN) model and secondly through consideration of true realisations of a roughened interface between conventional right-handed media (RHM) and LHM, studied through ray- and physical-optics approaches. The structure of the thesis

is as follows.

Chapter 2 presents analytical calculations for the propagation of electromagnetic radiation through an inhomogeneous layer whose refractive index varies in one dimension situated between bulk right- and left-handed media. Significant field localization is generated in the layer that is caused by the coherent superposition of evanescent waves. The strength of the field localization and the transmission properties of the layer are investigated as a function of the layer width, losses and defects in the refractive index; the former two being modelled by continuous changes, and the latter by discontinuous changes, in the index profile.

Chapter 3 develops this inhomogeneous layer model for the boundary and applies it to consider the perfect lens configuration. The field localisations at the boundaries are not independent of each other and their effect combines to affect the resolving capable of the lens. Specifically the layers produce an effect that is qualitatively similar to a lens with nonlinearly increased losses. The quality of the boundary closest to the image is shown to have a greater effect on the resolution of the lens.

Chapter 4 considers the action of a rough, but differentiable, interface upon the passage of rays between air and a left-handed medium. Negative refraction brings rays to a focus at distances closer to the boundary than can be attained by conventional refraction. This effect enables a new mechanism for reflection to occur, even in media that are impedance matched, caused principally by rays undergoing two interactions with the interface via paths that pass exclusively through air or the left-handed medium.

Chapter 5 develops the physical-optics approximation for LHM to show that the illumination of a roughened interface between air and a LHM produces a regime for enhanced focussing of light. This verifies the findings of Chapter 4 that the focusing occurs at distances closer to the boundary than can be attained in conventional matter. Caustics generated by the surface are brighter, fluctuate more, and interfere to produce Gaussian speckle at distances closer to the interface than occurs in equivalent right-handed materials. This is contrasted with Rice (perturbation) theory where scintillations derive from a real Gaussian process which then evolves into a complex Gaussian process at large distances from the interface.

The final chapter summarizes the conclusions to be drawn from this thesis along with potential areas for further research. Technical details are assigned to Appendices.

Chapter 2

Between Right- and Left-Handed Media

2.1 Introduction

In this chapter a Graded-Index (GRIN) model is introduced as a model for a diffuse surface comprising a layer between bulk left- and right-handed materials. This layer has a graded refractive index profile, prescribed by some analytical function, to smoothly connect the refractive indices of the bulk media. An excellent book that examines and summarises GRIN research in right-handed media (RHM) was published by Lekner in 1987 [55].

In previous research the assumption that the medium is non-magnetic, i.e. $\mu = 1$, is prevalent. Introducing the magnetic permeability in the GRIN model complicates matters and during the course of the work undertaken in this thesis, several teams have concurrently and independently attempted the task of adding μ into GRIN modelling [56, 57]. Nevertheless the model described within this chapter is the most general and applicable solution found to date. An exact, analytical solution will be derived that smoothly connects the bulk media by a linear profile across the layer. Within this chapter the derivation, and study, of these GRIN solutions is presented, and the next chapter will apply this technique to examine the perfect lens with imperfect boundaries.

Graded-index modeling of a boundary between bulk media has been used in conventional RHM for many years [55] and is tantamount to considering the properties of waves that

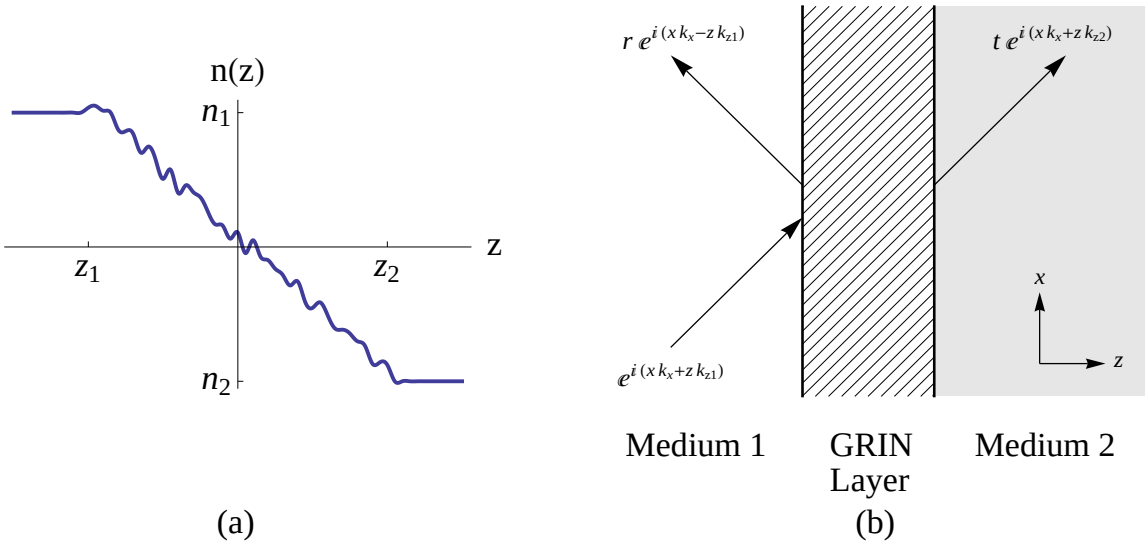

Figure 2.1: (a) A generic one-dimensional GRIN layer profile: $n = n_1$ for $z < z_1$, $n = \nu(z)$ for $z_1 < z < z_2$ and $n = n_2$ for $z > z_2$. (b) Pictorial representation of the incoming planar wave and the resulting reflected and transmitted waves.

interact with a one-dimensional refractive index profile

$$n(z) = \begin{cases} n_1 & z < z_1 \\ \nu(z) & z_1 < z < z_2 \\ n_2 & z_2 < z \end{cases}, \tag{2.1.1}$$

where $\nu(z_1) = n_1$, $\nu(z_2) = n_2$, with n_1 and n_2 being the bulk refractive indices in media 1 and 2 respectively[1], an example profile is given in Fig. 2.1 (a). In what follows, there is little restriction on the profile of $\nu(z)$, but it will be shown that only a few analytical solutions of Maxwell's equations exist for problems involving LHM.

To proceed we envisage an incoming planar s-wave so that the electric field $\mathbf{E}(x, y, z) = E_y(x, y, z)\,\hat{\mathbf{y}}$ (a harmonic time dependence, ω is assumed throughout) and with the p-wave state following analogously. Further to this, and using the fact that the refractive index is a function of z only, Maxwell's equations lead to separable solutions of the form $E_y(x, y, z) = \exp(ik_x x)\,E(z)$, where k_x is the wave number in the x direction which is in the plane of the interface between the bulk media. It follows, in line with classical optics techniques [53], that the planar wave entering the GRIN layer will give rise to a transmitted and reflected wave, shown in Fig. 2.1 (b):

[1]Specifically both ϵ and μ should be matched to the bulk media at each interface.

$$E(z) = \begin{cases} \exp(i\,k_{z_1}\,z) + r\exp(-i\,k_{z_1}\,z) & z < z_1 \\ \tilde{E}(z) & z_1 < z < z_2 \\ t\exp(i\,k_{z_2}\,z) & z_2 < z \end{cases}, \tag{2.1.2}$$

where $\tilde{E}$ is the electric field in the layer, k_{z_1} and k_{z_2} are the components of the wavevector projected in the z direction in media 1 and 2 respectively. The unknown reflection and transmission coefficients, r and t, can be found through knowledge of $\tilde{E}$ with appropriate boundary conditions applied at z_1 and z_2. The electric field in the layer, $\tilde{E}$, will be strongly affected by the choice of profile for $\nu(z)$, or more precisely by the choice profiles for the permittivity and permeability, $\epsilon(z)$ and $\mu(z)$, across the layer. The result of this chapter form the basis for the paper [49].

2.2 Construction of the magnetic-GRIN problem

Here the formal derivation of the magnetic-GRIN model is presented. The profile for the refractive index in the layer that can model the greatest range of scenarios is shown to be a linear connection between the refractive indices of the bulk media. In all that follows an incident electromagnetic s-wave is used, the p-wave case follows analogously.

2.2.1 The s-wave GRIN equation

Starting with Maxwell's equations:

$$\nabla \times \mathbf{H} = \frac{\partial \mathbf{D}}{\partial t} \tag{2.2.1a}$$

$$\nabla \times \mathbf{E} = -\frac{\partial \mathbf{B}}{\partial t} \tag{2.2.1b}$$

$$\nabla \cdot \mathbf{D} = \mathbf{0} \tag{2.2.1c}$$

$$\nabla \cdot \mathbf{B} = \mathbf{0} \tag{2.2.1d}$$

and the constitutive equations:

$$\mathbf{D} = \epsilon\epsilon_0\mathbf{E} \quad \text{and} \quad \mathbf{B} = \mu\mu_0\mathbf{H},$$

with the electric field polarized in the y direction (s-wave) and the refractive index changing in only the z direction:

$$\mathbf{E} = (0, E_y, 0)\,, \qquad \epsilon = \epsilon(z), \quad \mu = \mu(z),$$

it follows from (2.2.1b) that

$$\nabla \times \mathbf{E} = \left(-\frac{\partial E_y}{\partial z}, 0, \frac{\partial E_y}{\partial x} \right) = (i\omega B_x, i\omega B_y, i\omega B_z)$$

$$\Rightarrow \qquad \frac{\partial E_y}{\partial z} = -i\omega B_x, \qquad \frac{\partial E_y}{\partial x} = i\omega B_z, \qquad B_y = 0$$

$$\Rightarrow \qquad H_x = \frac{-1}{i\omega\mu\mu_0}\frac{\partial E_y}{\partial z}, \qquad H_z = \frac{1}{i\omega\mu\mu_0}\frac{\partial E_y}{\partial x}, \qquad H_y = 0 \tag{2.2.2}$$

assuming a $e^{-i\omega t}$ time dependence. The y component of (2.2.1a) provides another equation:

$$(\nabla \times \mathbf{H})_y = \frac{\partial H_x}{\partial z} - \frac{\partial H_z}{\partial x} = -i\omega\epsilon\epsilon_0 E_y. \tag{2.2.3}$$

Combining (2.2.2) and (2.2.3) gives

$$\frac{1}{i\omega\mu_0}\frac{\partial}{\partial z}\left(\frac{1}{\mu}\frac{\partial E_y}{\partial z}\right) + \frac{1}{i\omega\mu\mu_0}\frac{\partial^2 E_y}{\partial x^2} \;=\; i\omega\epsilon\epsilon_0 E_y$$

$$\Rightarrow \quad \frac{\partial}{\partial z}\left(\frac{1}{\mu}\frac{\partial E_y}{\partial z}\right) + \frac{1}{\mu}\frac{\partial^2 E_y}{\partial x^2} \;=\; \frac{-\omega^2\epsilon}{c^2}E_y. \tag{2.2.4}$$

Since the refractive index changes in only the z-direction we are free to seek a separable solution of the form

$$E_y = e^{i(k_x x - \omega t)}E(z),$$

where $E(z)$ satisfies

$$\frac{d}{dz}\left(\frac{1}{\mu}\frac{dE}{dz}\right) + \left(\frac{\omega^2\epsilon}{c^2} - \frac{k_x^2}{\mu}\right)E(z) = 0. \tag{2.2.5}$$

Equation (2.2.5) has few analytical solutions and these are detailed in Appendix A, the result being that the most versatile magnetic GRIN model is that which utilises a linear profile:

$$\mu = m\,z + d, \quad \epsilon = \eta\mu, \tag{2.2.6}$$

with m, z and η being, possibly complex, constants. The electric field in the layer is then

$$E(z) = \frac{\exp\left(\frac{-i\,\gamma\,\Psi(z)}{2}\right)\Psi(z)}{4\,c^2\,m^2}\left(\alpha F(z) + \beta G(z)\right), \tag{2.2.7}$$

where α and β are constants of integration,

$$F(z) = \mathrm{M}\left(1 - \frac{ik_x^2}{4\,m^2\,\gamma}, 2, i\,\gamma\,\Psi(z)\right),$$

$$G(z) = \mathrm{U}\left(1 - \frac{ik_x^2}{4\,m^2\,\gamma}, 2, i\,\gamma\,\Psi(z)\right),$$

$$\gamma = \frac{\eta^{1/2}\,\omega}{c\,m}, \quad \Psi(z) = (d + m\,z)^2$$

with M and U being the confluent hypergeometric functions of the first and second kind [58], respectively.

2.3 A GRIN layer between half-planes of RHM and lossless LHM

The most concise, non-trivial, problem that can be considered is that of a transition between air, $n = 1$, and its LHM equivalent, $n = -1$. Without loss of generality the origin of z can be chosen to be at the centre of this transitional region with a being the layer half-width. Equation (2.2.7) then provides the field in the layer with $d = 0$ and $m = -1/a$ in the model for $\mu(z)$. Within this chapter situations will be examined where $\epsilon(z) = \mu(z)$ for all z, therefore η is set to unity throughout.

2.3.1 Boundary Conditions

Viewing (2.2.5) it would seem that the continuity of

$$E(z) \quad \text{and} \quad \frac{1}{\mu(z)}\frac{dE(z)}{dz} \tag{2.3.1}$$

gives logical boundary conditions, and indeed the formal derivation through the continuity of the tangential components of **E** and **H** verifies this choice.

Thus application of (2.3.1) at the boundaries of the layer, $z = \pm a$ (c.f. (2.1.2)), gives four equations for the four unknowns: the reflection coefficient r from the layer, the transmission coefficient t from the layer, together with the constants of integration α and β.

2.3.2 Results

Utlizing the boundary conditions (2.3.1) gives the reflection and transmission from a transitional layer and allows the electric field to be evaluated throughout the entire region. Figure 2.2 shows a three dimensional and contour representation of the real part of the electric field when a plane wave, at an angle of incidence of $\pi/8$, impinges on the transitional layer[2].

The most prominent feature of this solution is the large peaks in the electric field inside the transition region. Before examining the localisations, there are a number of underpinning features that can be overlooked in the face of these large electric fields, but which are still interesting in their own right. The first of which is that it is clear from the phase fronts of Fig. 2.2 (b) that the transmitted wave has indeed undergone negative refraction. Further to this the solution gives $|t| = 1$, i.e. the interface is fully transmissive, indeed it is

[2]The time dependent animations of these graphs are included within the addition media CD attached to the thesis.

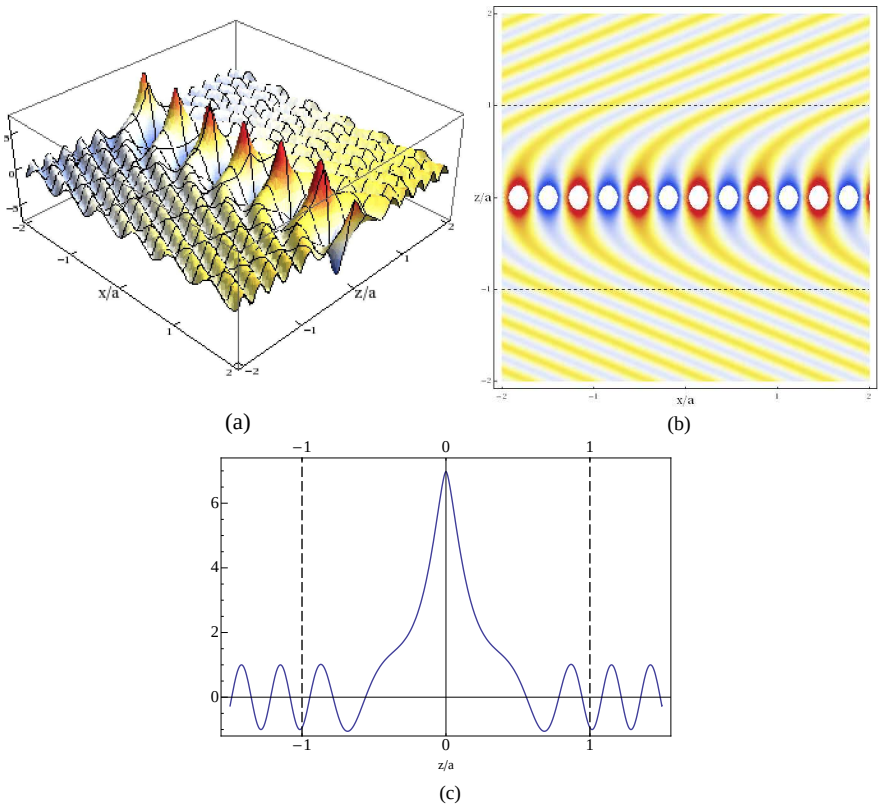

Figure 2.2: The real part of E that results for a dimensionless layer width, $ka = 8\pi$ for an angle of incidence $\theta = \pi/8$ to the normal of the surface from a vacuum ($z < -1$) to a bulk medium with $\epsilon = \mu = -1$ ($z > 1$). (a) shows a 3D representation of the real part of the electric field, note the localizations move with speed ω/k_x in the x direction, (b) the same situation in contour form and (c) a cross section of part (a) in the constant x plane. The amplitude of the field is taken to be unity in the homogeneous media. Animated version of (a) and (b) can be found on the additional media CD.

impedance-matched throughout the layer. Moreover, not only is t of unit magnitude, it is equal to unity; this is to say that a lossless transitional layer creates *no amplitude or phase discrepancy of the wave into the LHM*. Put another way, if measurements could only be taken in medium 2 then it would be impossible to distinguish whether a GRIN transition was used or if there was a planar interface between the media at $z = 0$.

The localisations of the field within the transition layer derive from evanescent waves that are set up within the layer and amplified within the LHM as illustrated in Fig. 2.3, which is meant for illustrative purposes alone. This depicts the field through the layer, within which $|n| < 1$. In the region $-1 < z/a < 0$, both ϵ and μ are positive and so when the value of $|n|$ falls below that value which allows a propagating mode to exist, i.e.

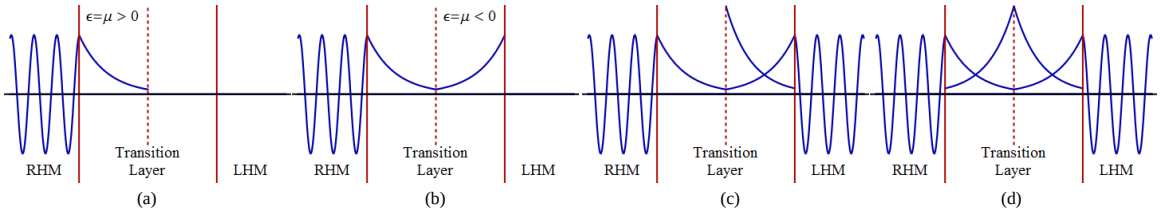

Figure 2.3: Within the inhomogeneity layer there is a band where an incoming wave become evanescent in nature, $|n|$ being too low to allow propagation (a). These evanescent modes decay within the RHM and exponentially grow in the LHM [2] (b). When an evanescent wave reaches a point where it can propagate again the boundary conditions cause an evanescent wave to be reflected back into the layer (c). This propagates to the other side where another reflection occurs (d). It is the summation of each of these evanescent reflections that gives rise to the structure seen in Fig. 2.2 (a).

$|n(z)| < \sin\theta$ (where θ is the incident angle), an evanescent mode is established that decays with increasing z. This evanescent mode has a finite amplitude at $z = 0$. For $0 < z/a < 1$, both ϵ and μ are negative, with result that the evanescent wave is amplified out to a distance z_c satisfied by $|n(z_c)| = \sin\theta$, whereupon the wave can propagate once again for $z > z_c$. An evanescent wave is reflected back into the layer that *increases* with decreasing z, until $z < 0$, where the mode then decreases in the right-handed medium. Thus a coherent structure is established in the region $|n(z)| < z_c$ contained within the layer through the interference of these evanescent modes. This prompts questioning how the peak magnitude of the field scales with the layer width. This dependence is shown in Figure 2.5 (a) by the red (triangles) curve, and shows an exponential growth with the layer thickness. This dependence obtains from the complicated nature of the confluent hypergeometric functions and their derivatives, that are contained within the integration constants α and β. Clearly this unbounded increase is unphysical and will be corrected by the incorporation of losses into the model, as will be considered in the next section.

2.4 A GRIN layer between half-planes of RHM and lossy LHM

In this section losses are incorporated into the bulk left-handed medium, which is assumed to have refractive index $n = -1 + \kappa i$ with $\kappa > 0$. The inhomogeneous layer is also assumed

to be lossy with profile:

$$\mu(z) = \epsilon(z) = \left(-1 + \frac{\kappa}{2}i\right)\frac{z}{a} + \frac{\kappa}{2}i \tag{2.4.1}$$

According to this model, the refractive index is purely imaginary at the origin. This implies that the field will no longer grow without bound with increasing layer width and that a reflected wave may exists in the right-handed half-space, $z < 0$. Indeed the presence of losses implies that for $z \gg 0$, the wave will have decayed completely. The structure of the solution within the layer is also substantially modified by the losses, for the second confluent hypergeometric function possesses a branch cut which must be crossed as the layer is traversed.

2.4.1 Locating the branch-cut of the hypergeometric U

Given the emphasis of this thesis on impedance matched media ($\eta = 1$) the explict calculation of the branch-cut localization in this case is given, this can be generalized to any η but resulting in more convoluted algebra. The branch cut occurs within the hypergeometric U function

$$\mathrm{U}(a,\, b,\, Z) \tag{2.4.2}$$

when

$$\Re e(Z) < 0, \quad \Im m(Z) = 0 \tag{2.4.3}$$

for the case of $\eta = 1$

$$Z = i(mz + d)^2 \frac{\omega}{m\,c} = in^2 \frac{\omega}{m\,c}. \tag{2.4.4}$$

Using this and (2.4.3) gives

$$\Im m\left(\frac{n^2}{m}\right) > 0, \quad \Re e\left(\frac{n^2}{m}\right) = 0, \tag{2.4.5}$$

which can be simplified by noting that

$$\Im m\left(\frac{n^2}{m}\right) = \Im m\left(\frac{n^2\, m^*}{|m|^2}\right) = \frac{\Im m\left(n^2\, m^*\right)}{|m|^2}$$

and similarly $\Re e\left(n^2/m\right) = \Re e\left(n^2\, m^*\right) / |m|^2$ so that (2.4.5) is equivelent to

$$\Re e\left(n^2\, m^*\right) = 0, \quad \Im m\left(n^2\, m^*\right) > 0 \tag{2.4.6}$$

i.e. that

$$n^2 = i\,\mathbb{X}\,m \tag{2.4.7}$$

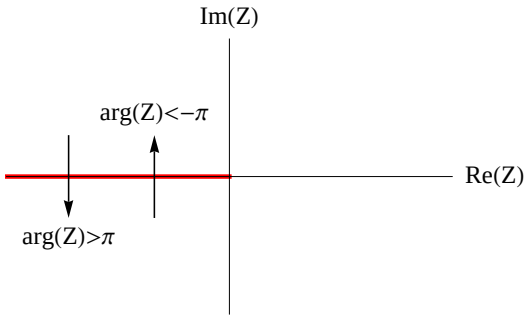

Figure 2.4: A diagram showing the branch cut of the hypergeometric U and the two directions that it can be crossed with the resulting argument shown in each case.

for some real valued $\mathbb{X} > 0$. The real and imaginary parts of (2.4.7) give two equations for the unknowns z and $\mathbb{X}$. Solving these equations and choosing the solution for which $\mathbb{X} > 0$ (by using $|m| \geq \Im m(m)$) gives

$$z_b = \frac{m_{\mathbb{R}}\, d_\partial - d_{\mathbb{R}}\,(m_\partial + |m|)}{m_{\mathbb{R}}\,|m|} \tag{2.4.8}$$

where z_b is the location of the branch cut, $m = m_{\mathbb{R}} + i\, m_\partial$ and $d = d_{\mathbb{R}} + i\, d_\partial$. If the refractive index is $n_1 = \phi_1 + \kappa_1 i$ at z_1 and $n_2 = \phi_2 + \kappa_2 i$ at z_2 then

$$m = \frac{\phi_2 - \phi_1}{z_2 - z_1} + \frac{\kappa_2 - \kappa_1}{z_2 - z_1}\, i = m_{\mathbb{R}} + i\, m_\partial \tag{2.4.9}$$

$$d = \frac{z_2\,\phi_1 - z_1\,\phi_2}{z_2 - z_1} + \frac{z_2\,\kappa_1 - z_1\,\kappa_2}{z_2 - z_1}\, i = d_{\mathbb{R}} + i\, d_\partial \tag{2.4.10}$$

in terms of these variables the full form for the location of the branch cut is

$$z_b = \frac{(\kappa_1\,\phi_2 - \kappa_2\,\phi_1)\,|\Delta z| + \left(\Delta\kappa^2 + \Delta\phi^2\right)^{1/2}(z_1\,\phi_2 - z_2\,\phi_1)}{\left(\Delta\kappa^2 + \Delta\phi^2\right)^{1/2}\Delta\phi} \tag{2.4.11}$$

with $\Delta\psi = \psi_2 - \psi_1$ for any ψ. Although (2.4.11) is not quite as elegant as (2.4.8), it is far more amenable to programming.

2.4.2 Classifying the Branch Cut

Although the position of the branch cut has been found, the direction that it is traversed is not yet known. With reference to Figure 2.4, the direction the branch cut is crossed can be found through the third argument of the hypergeometric U, Z, specifically through the sign of $\frac{d}{dz}\left(\Im m(Z)\right)$:

$$\text{Sign}\left[\frac{d}{dz}\left(\Im m\Big(i\, n^2 \frac{\omega}{m\, c}\Big)\right)\Big|_{z=z_b}\right] = \text{Sign}\left[\frac{d}{dz}\left(\Re e\left(\frac{n^2}{m}\right)\right)\Big|_{z=z_b}\right]$$

now

$$\frac{d}{dz}\left(\Re e\left(\frac{n^2}{m}\right)\right) = \frac{d}{dz}\left(\frac{\Re e\left(n^2\, m^*\right)}{|m|^2}\right) = \frac{\Re e\left(\frac{d}{dz}\left(n^2\, m^*\right)\right)}{|m|^2}$$

as $|m|^2 \geq 0$. Therefore the whole problem is determined by

$$\frac{d}{dz}\left(n^2\, m^*\right) = \frac{d}{dz}\left(n^2\right) m^* = \left(2\, n\, m\right) m^* = 2\, n\, |m|^2$$

given the form, (2.2.6), of n. Consequently we have that

$$\text{Sign}\left[\frac{d}{dz}\left(\Im m\left(i\, n^2\, \frac{\omega}{m\, c}\right)\right)\Big|_{z=z_b}\right] = \text{Sign}\left[\Re e\left(n|_{z=z_b}\right)\right]. \tag{2.4.12}$$

The analytic continuation of the Hypergeometric U, given [58] by

$$\text{U}\left(a,\, 2,\, Z\, e^{2\pi i p}\right) = \frac{2\,\pi\, i\, p}{\Gamma(a-1)}\text{M}(a,\, 2,\, Z) + \text{U}(a,\, 2,\, Z) \tag{2.4.13}$$

where Γ is the gamma function. With reference to (2.4.13) and Fig. 2.4 it can be seen that if $\frac{d}{dz}\left(\Im m(Z)\right) < 0$ $\left(\Re e\left(n|_{z=z_b}\right) < 0\right)$ the $p = 1$ contribution is required and similarly if $\frac{d}{dz}\left(\Im m(Z)\right) > 0$ $\left(\Re e\left(n|_{z=z_b}\right) > 0\right)$ the $p = -1$ contribution is needed. Altogether this gives

$$\text{U}(a,\, 2,\, Z(z)) = \overline{\text{U}}(a,\, 2,\, Z(z)) - \text{H}(z - z_b)\, \frac{2\,\pi\, i\ \text{Sign}\left[\Re e\left(n|_{z=z_b}\right)\right]}{\Gamma(a-1)}\text{M}(a,\, 2,\, Z(z)) \tag{2.4.14}$$

where z_b is given in (2.4.11), H is the Heaviside step function and $\overline{\text{U}}$ is the principal branch of the hypergeometric function ($-\pi < \arg Z \leq \pi$).

2.4.3 Results

Equations (2.4.11) and (2.4.14) allows for calculations involving losses to be performed in a similar way to the previous sections. Figure 2.5 details the peak height of the electric field from various situations including the addition of losses. The main point to note is that figure 2.5 (a) shows the exponential dependence of the localisations on layer width is suppressed by the addition of losses.

A careful treatment of the branch-cut shows, as detailed in the previous section, that the form of the solution is affected. The blue (squares) curve in Figure 2.5 (a) shows that the peak value of the field in the layer now decreases exponentially with increasing layer width for a modest value of $\kappa = 10^{-3}$, which is also the case for the variation with the angle of incidence, θ, as shown in Figure 2.5 (b). Indeed the peak value of field within the layer is less than that outside it, so that the localization effect is entirely suppressed. This

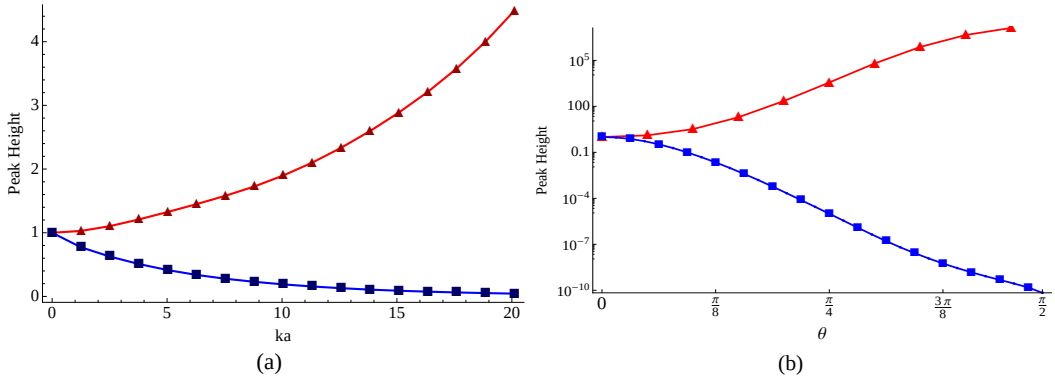

Figure 2.5: A wave of wave number k, propagating at an angle θ to the normal, passes from a vacuum through the inhomogeneity region, of width $2a$, into a medium where $\mu = -1 + \kappa i$. (a) shows the magnitude of the localisation in the medium relative to the incident wave with $\theta = \pi/8$ for $\kappa = 0$ (lossless) [Red Triangles] and $\kappa = 10^{-3}$ [Blue Squares]. (b) shows the magnitude of the localisation but as a function of the incident angle, θ, for no losses [Red Triangles] and $\kappa = 10^{-5}$ [Blue Squares]

is because the evanescent modes are dissipated by the losses. Despite these losses, the field within the layer is still finite once the location where the modes can propagate again is attained, and so there is still transmission of radiation into the bulk left-handed medium.

Figure 2.6 (a) shows the transmission coefficient at $z = a$ for $\kappa = 10^{-3}$ as a function of the angle of incidence for a selection of values of the dimensionless layer width, $ka = 0.1$ (brown triangles), $ka = 1$ (blue circles) and $ka = 5$ (red squares). The layer becomes opaque to radiation at progressively smaller angles of incidence as the layer thickness increases. Figure 2.6 (b) shows the negative exponential dependence of the transmission coefficient as a function of ka for different values of the loss, $\kappa = 10^{-1}$ (red squares), $\kappa = 10^{-3}$ (blue circles) and $\kappa = 10^{-10}$ (blue triangles), the latter two being essentially indistinguishable within the model used. Hence for losses of the order 10^{-3} or lower the transmission coefficient is insensitive to the precise value of κ: this is caused by the dampening of the evanescent reflections within the transition layer. It can also be noted that the transmission coefficient, for fixed ka, increases as the losses increase. This effect occurs because large losses quickly damp all but the first reflection of the evanescent mode within the layer which leads to a larger ratio between the transmitted and reflected wave. The total transmitted and reflected power, however, steadily decreases as losses increase.

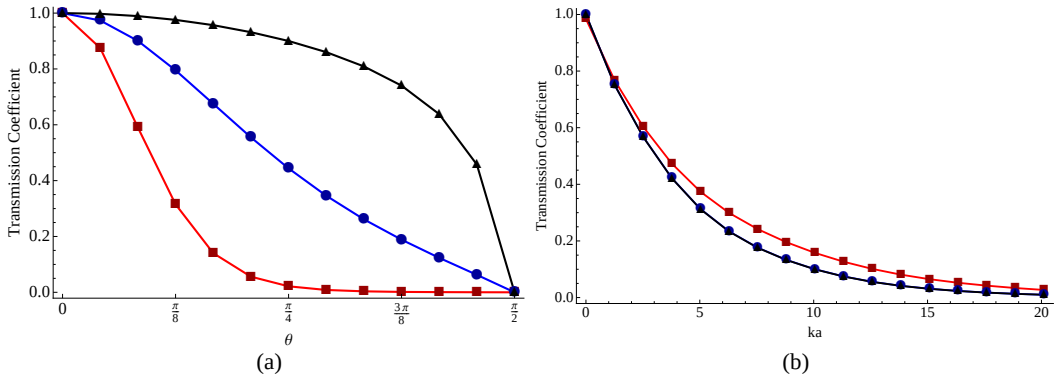

Figure 2.6: For the situation detailed in figure 2.5, (a) displays the dependence of the transmission coefficient on θ for various ka, this is obtained with $\kappa = 10^{-3}$ for $ka = 5$ [Red Squares], 1 [Blue Circles] and 0.1 [Black Triangles] and (b) shows the transmission coefficient as a function of ka at $\theta = \pi/8$ for $\kappa = 10^{-1}$ [Red Squares], 10^{-3} [Blue Circles] and 10^{-10} [Black Triangles] (The latter two are indistinguishable within the model used)

2.5 Generalizing the GRIN model

2.5.1 The 'Staircase' model - An alternate approximation

This previous section showed that the lossless results are very different from those where losses are included and this is principally because the refractive index vanishes at $z = 0$ in the former case, whereas there is a branch-cut in the solution for the latter. This section will examine the robustness of these two classes of solution by modelling the refractive index in the layer by a staircase, as depicted in Fig. 2.7 (a). Within each plateau of the staircase, the refractive index is constant and so the solution to Maxwell's equations is comprised of two independent exponentials. Using the boundary conditions (2.3.1) at the end of each of the N steps gives $2N$ equations for the $2N$ constants that determine the amplitudes and phases throughout the layer [55].

Figure 2.8 contrasts the solutions obtained from the continuum models of sections 2.2-2.4 and the discrete staircase model. Figure 2.8(a) is for a lossless medium and is repeated from figure 2.2(c) for ease of comparison. This should be compared with 2.8(b), which is for a staircase with $N = 2^7$ equally spaced plateaus throughout the layer, and there is no discernible difference between the two solutions. Figure 2.8(c) shows the GRIN model solution for $\kappa = 10^{-5}$ - the localization has been suppressed entirely by the losses. Note however that the solution of the lossy staircase model shown in 2.8(d) retains the localization feature and is essentially an attenuated form of the solution shown in 2.8(b). Hence the

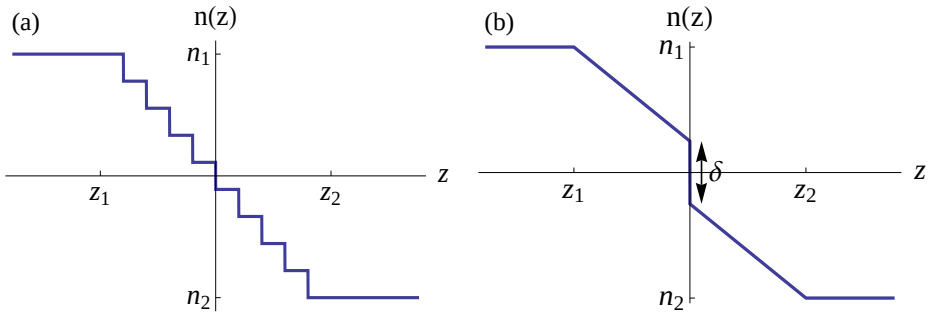

Figure 2.7: (a) An example staircase profile for the refractive index. (b) The δ-GRIN model interoperating the advantages of the staircase and GRIN models.

staircase model is quantifiably different from the lossy version of the GRIN model. This prompts investigating whether a simple element can be incorporated into the GRIN model that captures both the lossless and lossy behaviours shown by the staircase model.

2.5.2 The effect of discontinuities in the refractive index profile - the δ-GRIN model

A new model can now be envisioned, based on the previous GRIN model, that is qualitatively consistent with the staircase model for low loss. This is done by the addition of a (single) discontinuity of size δ located at $z = z_b$, given by (2.4.11), and an example refractive index profile is shown in Fig. 2.7 (b). Whilst more discontinuities could be placed throughout the layer, the additional discontinuities cause far smaller alterations to the transmission, reflection and field structure as compared to the primary discontinuity placed at (2.4.11). The field is more sensitive to discontinuities near this point, and as such numerous discontinuities can be encapsulated, to first order, with a single discontinuity at (2.4.11). Clearly further discontinuities can be added within the layer to refine the approximation, but this adds little to the understanding of the problem and is not considered here.

Figure 2.9 quantifies the sensitivity of this δ-GRIN model with the size of δ for an angle of incidence $\theta = \pi/8$. Figure 2.9(a) shows the dependence of the size of the peak value of the localized field with the dimensionless layer width. The blue (stars) and green (diamonds) curves are the lossless and lossy ($\kappa = 10^{-3}$) cases respectively, as previously seen in figure 2.5(a), and these act as bounds for the lossy δ-GRIN model, where the value of $\delta = 0.1$ dark yellow (squares), $\delta = 0.05$ purple (triangles) and $\delta = 0.01$ blue (circles). It can be seen that these results match smoothly to the lossless results for small values of ka, and for sufficiently small values of ka are independent of δ. Figure 2.9(b) shows the dependence of

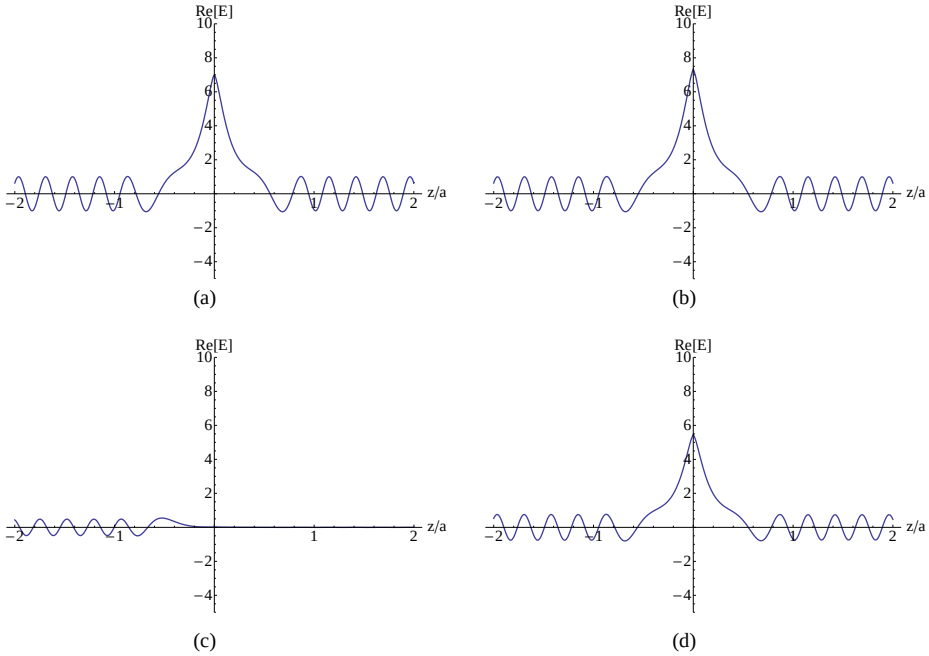

Figure 2.8: (a) A typical electric field for a lossless GRIN, (b) for a lossless staircase with $N = 2^7$, (c) for a lossy ($\kappa = 10^{-5}$) GRIN and (d) for a lossy staircase with $N = 2^7$.

the transmission coefficient as a function of δ (note, a value of $\delta = 2$ is equivalent to step change between the bulk right- and left-handed media without a diffuse layer). The curves displayed are for different values of the dimensionless layer width, $ka = 1$ purple (triangles), $ka = 10^{-1}$ dark yellow (squares) and $ka = 10^{-2}$ green (circles). Thus the more diffuse the layer is, the less radiation is transmitted to the left-handed medium.

To achieve the smooth transition into lossless LHM, both the losses and the discontinuity size must be simultaneously reduced to zero, but their relative ordering matters. Letting the losses tend to zero first leads to greater transmission across a range of transitional layer sizes as compared with letting the discontinuity step tend to zero first. This will now be quantified.

2.5.3 The simultaneous limit $\delta \to 0^+$ and $\kappa \to 0^+$

We have shown that the GRIN model displays different behaviour according to whether $\kappa = 0$ or is finite, but that the latter case can be made consistent with the staircase model with the inclusion of a discontinuity δ in the refractive index profile, and this we have termed the δ-GRIN model. There is clearly singular behaviour in the nature of the solutions obtained with these models as δ and κ both tend to zero, which recovers the

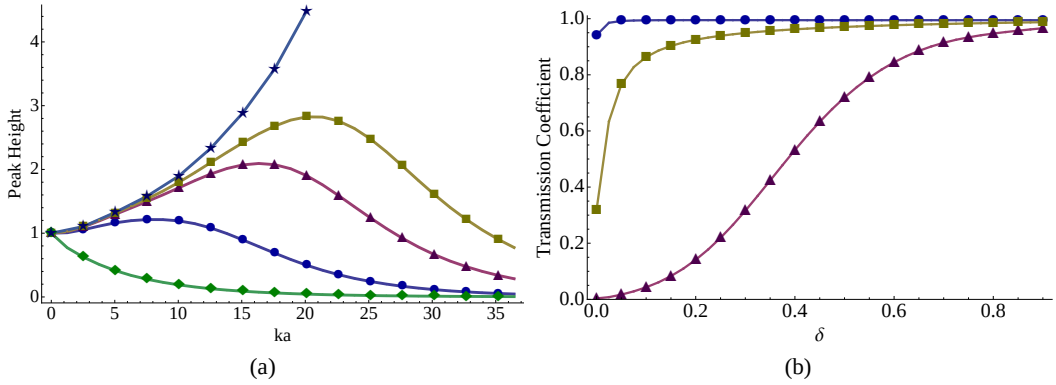

Figure 2.9: (a) Peak localisation height with the parameter values of figure 2.5 (a) but with the addition of a discontinuity, δ. The case shown are $\kappa = 10^{-3}$ and $\delta = 0$ [Green Diamonds], $\kappa = 10^{-3}$ with $\delta = 0.01$ [Blue Circles], $\kappa = 10^{-3}$ with $\delta = 0.05$ [Purple Triangles], $\kappa = 10^{-3}$ with $\delta = 0.1$ [Dark Yellow Squares] and $\kappa = 0$ with no δ [Light Blue Stars]. (b) Transmission as a function of δ for $ka = 1$ [Purple Triangles] , $ka = 10^{-1}$ [Dark Yellow Squares] and $ka = 10^{-2}$ [Blue Circles].

lossless GRIN model. This section discusses the reason for the discrepancy.

We may define two classes of solution obtained in terms of whether or not there exists localization of the field within the layer, and the class that the solution adopts is different according to whether we take $\delta \to 0$ followed by $\kappa \to 0$ (which produces no localization), or $\kappa \to 0$ followed by $\delta \to 0$ (which does produce localization). If $\delta \gg \kappa$ (in magnitude) as $\delta \to 0$, then the field will show pronounced localization features.

The terminology of Leonhardt [59] provides an alternative way to view the behaviour of the two models, depending on whether the branch cut of the U hypergeometric function is crossed. The quantity that determines this is the third argument of U, which is $\Lambda(z) = i\gamma\Psi(z)$, see equation (2.2.7). In the lossless case the path of $\Lambda(z)$ causes the third argument of U to touch its branch cut at the origin, but not necessarily cross it, this gives rise to the two distinct solutions seen previously. The axes of figure 2.10(a-b) are the real and imaginary parts of $\Lambda(z)$ and the curves are the loci of $\Lambda(z)$. The branch cut of U is $\mathrm{Re}(\Lambda(z)) < 0$ and $\mathrm{Im}(\Lambda(z)) = 0$, which is shown by the thick black lines. Figure 2.10(a) is for the GRIN model, and the paths of $\Lambda(z)$ must cross the branch-cut, so that the solutions move to the next Riemann sheet, and give rise to the non-localized solutions as depicted in figure 2.10(c). Figure 2.10(b) is appropriate for the δ-GRIN model, and the presence of a non-zero value of δ means that the locus of $\Lambda(z)$ does not cross the branch cut, but can 'jump' across it with the solution remaining on the same Riemann sheet - hence the localization form of the solution is obtained as shown in Figure 2.10(d).

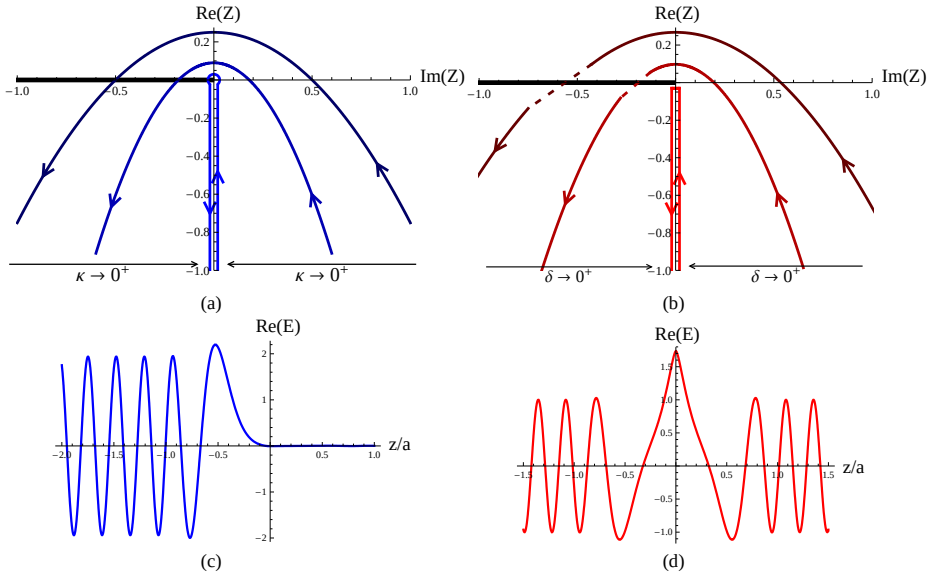

Figure 2.10: An illustration of the complex path for the third argument of the hypergeometric U function as the layer is traversed. The thick black line indicates the branch cut and the paths are for different losses. (a) shows the situation that pertains to the GRIN solution and that as $\kappa \to 0$ the path becomes parallel with the negative imaginary axis whilst including the branch cut contribution. (b) shows that the introduction of the discontinuity causes the branch cut to be avoided (dashed line) leading to a lossless solution along the negative imaginary axis that does not include the branch cut. The real parts of the electric field across a lossless layer are shown in (c) and (d) for the limit of (a) and (b) respectively, where a is the layer half-width.

2.6 Conclusion and discussion

In this chapter we have introduced a model to account for smooth changes of permittivity and permeability across a diffuse boundary between bulk right- and left-handed metamaterials as an effective medium model for a surface. A full-wave, exact analytical solution to this problem leads to a strong localisation of the field in the transition region whilst being fully transmissive. In the lossy case the strong localisation is removed and a reflected wave exists. Consideration of another analytical model leads to the inclusion of a discontinuity in the refractive index profile which restores qualitatively the features of the lossless case. In all cases the reflected and transmitted wave properties have been determined analytically.

The reason for the localization in the layer is the constructive interference of evanescent modes that are stimulated whenever $|n| < \sin\theta$ as illustrated in Figure 2.5. It should be stressed that these modes are not a conventional plasmon mode which is generated by a discontinuous change in the refractive index [60]. Rather the diffuse layer causes the

coherent addition of a plasmon and an anti-plasmon [61] throughout the *volume* of the metamaterial for which $|n| < \sin\theta$.

Although not detailed here, equation (2.2.6) can also be used to model changes between two right-handed media or indeed two left-handed media. Altogether this method can model a diffuse boundary between any combination of left- and right-handed media, with or without losses in either medium.

Having exhausted the physics of a single interface, the interplay of two interfaces is deserving of consideration. The next chapter will investigate the perfect lens configuration with the boundaries being modelled by GRIN layers.

Chapter 3

Perfect lens with not so perfect boundaries

3.1 Introduction

In the last chapter a half-space of LHM with a GRIN boundary onto a vacuum was investigated. Although the half-space of LHM gave rise to novel results, it cannot encapsulate evanescent wave restoration because this requires a decaying evanescent wave from a second interface [2]. This feature is unique to the perfect lens and warrants further investigation. This chapter is principally concerned with the perfect lens' ability to resolve evanescent modes in the presence of GRIN boundaries. The super-resolving ability of the lens is governed by evanescent waves, and their behaviour will be quantified as a function of the properties of the GRIN layer and the bulk LHM. In particular it will be shown that there is a qualitative similarity between the effects produced by diffuse boundaries and those caused by loss in the bulk medium. The result of this chapter form the basis for the paper [50].

3.2 Model

We model the lens as a slab of LHM of refractive index $n = -1 + \kappa i$ with a diffuse layer on both interfaces with air, for which $n = 1$. The permeability and permittivity change linearly through the layer according to $\mu(z) = mz + d$ with $\epsilon(z) = \mu(z)$, c.f. chapter 2, as shown in Fig 3.1 (b). The model adopted for the material parameters allow m and d to be complex and enables an exact analytical solution to Maxwell's equations to be obtained. The results are not therefore limited by any computational restrictions or artifacts.

In the last chapter a transitional layer between half-spaces of RHM and LHM was

studied. The solution led to localization of the field within the layer and it was found that the inclusion of a discontinuity, δ, in the refractive index at a point within the layer enabled the GRIN model to more flexibly allow for surface defects and rapid changes in the refractive index. However the semi-infinite half-plane model, whilst illustrating the novel effects introduced by the layer, does not permit evanescent modes to be amplified within the LHM, and it is therefore necessary to consider a finite thickness of LHM.

We assume a s-polarized wave is incident upon the slab from the left, as shown in Fig. 3.1 (a), and the solution to Maxwell's equations in each of the regions has the form $\mathbf{E} = E(z)\exp(i(k_x x - \omega t))\,\hat{\mathbf{y}}$, where

$$E(z) = \begin{cases} e^{(ik_{z_1}z)} + r\,e^{(-ik_{z_1}z)} & z < -h-ah \\ \tilde{E}_1(z) & -h-ah < z < -h \\ \tilde{E}_2(z) & -h < z < -h+ah \\ s\,e^{(ik_{z_2}z)} + q\,e^{(-ik_{z_2}z)} & -h+ah < z < h-ah \\ \tilde{E}_3(z) & h-ah < z < h \\ \tilde{E}_4(z) & h < z < h+ah \\ t\,e^{(ik_{z_1}z)} & h+ah < z \end{cases}, \tag{3.2.1}$$

q, r, s and t are dependent on the boundary conditions, k_{z_1} and k_{z_2} are the z components of the wave numbers outside and inside the lens respectively and $\tilde{E}_{1/2/3/4}(z)$ are the electric fields in the diffuse layers which are expressible in terms of hypergeometric functions as detailed in the last chapter, (2.2.7).

The slab is illuminated by a planar source located at $z = -2h$ with phase function of the form $\exp(i(k_x x + k_z z))$. Such waves form the building blocks of more complicated sources, for example multipoles. The problem can be defined entirely by the following non-dimensional variables: the wavenumber from the source, $kh = \left(k_x^2 + k_z^2\right)^{1/2} h$; the wavenumber directed parallel to the lens, $k_x h$; the layer half-widths, a; the loss in the LHM, κ; and the discontinuity size, δ. The two layer sizes and discontinuities need not have the same value, but making them equal simplifies the problem without losing the essential novel effects introduced by the layers.

3.3 Results

First the behaviour of the evanescent waves within a perfect lens is examined and two localizations are found to occur, one within each layer. Transmission across both propagating and evanescent modes are then investigated showing that attenuation to transmission due to transitional layers is, for evanescent modes, qualitatively similar to increased losses within

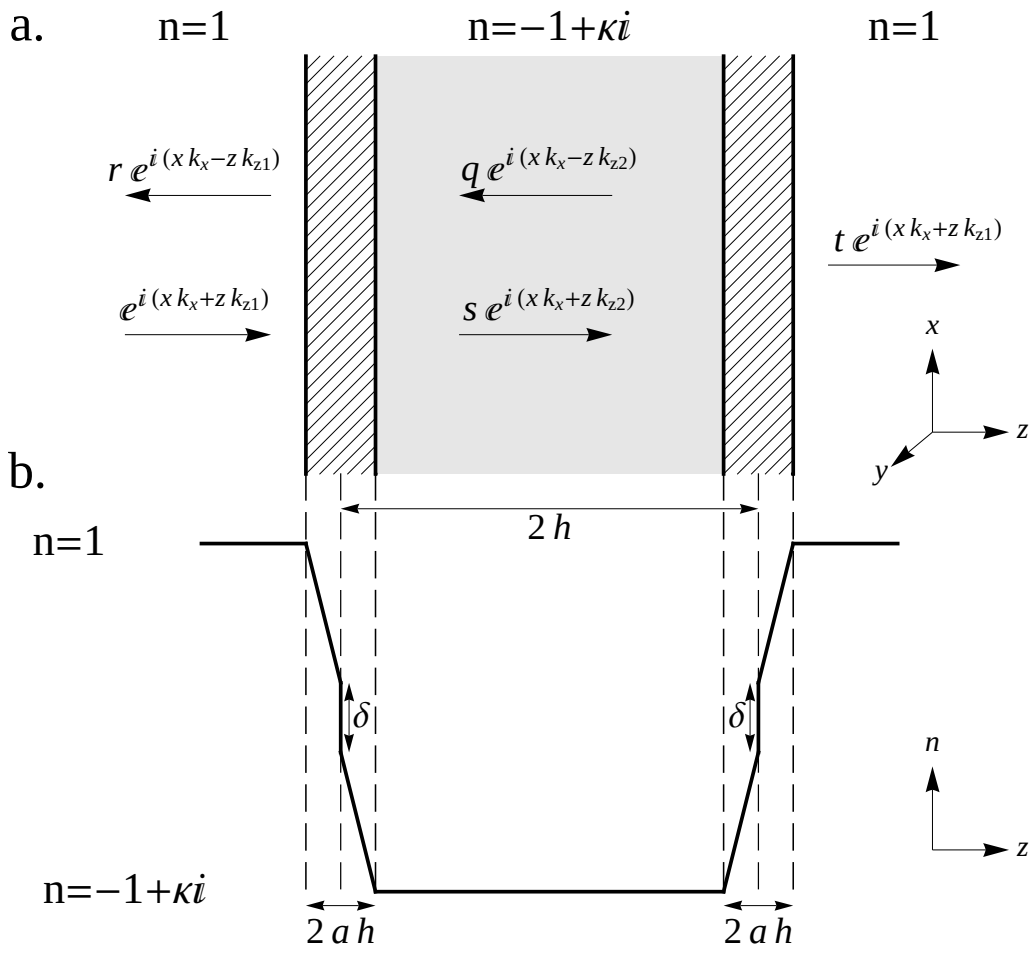

Figure 3.1: An illustration of (a) the physical set-up and (b) the refractive index profile for a lens with diffuse boundaries.

the lens. The quality of the lens' boundaries are shown to be of paramount importance as attenuation due to these boundaries combines with the high losses of current metamaterials to quench transmission, unless boundaries are of the highest quality.

3.3.1 Behaviour of evanescent waves in the lens

When $k_x > k$ the incoming wave is evanescently decaying in the z direction, i.e. k_z becomes imaginary, and a typical field distribution from the source point to the primary focus at $z = 2h$ is shown in Fig. 3.2. Field localizations can be seen in each layer. These have larger peak values than would be anticipated by continuation of the evanescent modes from the source (as shown by the dashed lines). The enhancement is due to the reduction in $\mathrm{Re}(n)$ within the layer magnifying the amplification (or decay) of evanescent waves, see Fig 2.3.

The *gradient* of the evanescent field is also enhanced in the layers. Consequently the most localized modes, corresponding to larger values of $k_x h$, will be dissipated if the LHM is lossy. It can therefore be anticipated that resolution will be adversely affected by the presence of the layers, and this is demonstrated in the next section.

3.3.2 Transmission of propagating and evanescent modes

A measure of the super-resolving capability of a lens for a fixed wavenumber, kh, is the maximum value of $k_x h$ that can be accommodated at the focus. Fixing kh and allowing $k_x h$ to vary from 0 to ∞ allows the study of the full range of propagating and evanescent waves. Figure 3.3(a) shows the relationship between $k_x h$ and $k_z h$. If the lens is lossless, the presence of the layers have no effect on its perfect resolving ability. However, if the LHM has any finite (positive) value of the loss, the layers serve to deteriorate the lens performance by a margin in excess of that caused by dissipation alone. This is illustrated in Fig. 3.3(b) which shows the transmission plotted as a function of $k_x h$ for different values of a, where the transmission is defined as the amplitude of the field at the focus normalized by that at the source.

The curves in Fig. 3.3 (b) annotated with circles, squares and triangles correspond to layer widths $a = 0$, 0.01 and 0.05 respectively. For $k_x < k$, the waves are propagating, and the transmission falls to zero as the modes approach grazing incidence, beyond which they are purely evanescent. Evanescent modes are transmitted by the lens, but the efficiency decreases with increasing $k_x h$. The effect of a thicker layer is to reduce the maximum transmission and the value of $k_x h$ for which the transmission coefficient becomes small.

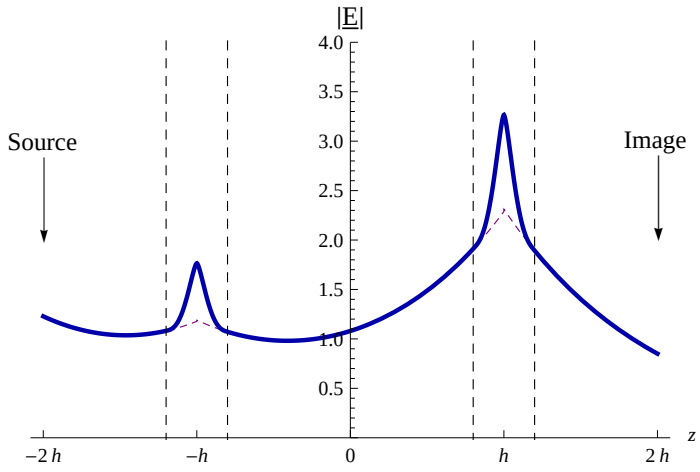

Figure 3.2: Typical field profile across the lens normalized against $|\mathbf{E}|$ for the incoming wave at $z = -2h$. Here $\kappa = 10^{-5}$, $\delta = 0.01$, $a = 0.2$, $kh = 10$, $k_x h = 10.05$. The dotted vertical lines denote the GRIN layers at the surfaces of the lens.

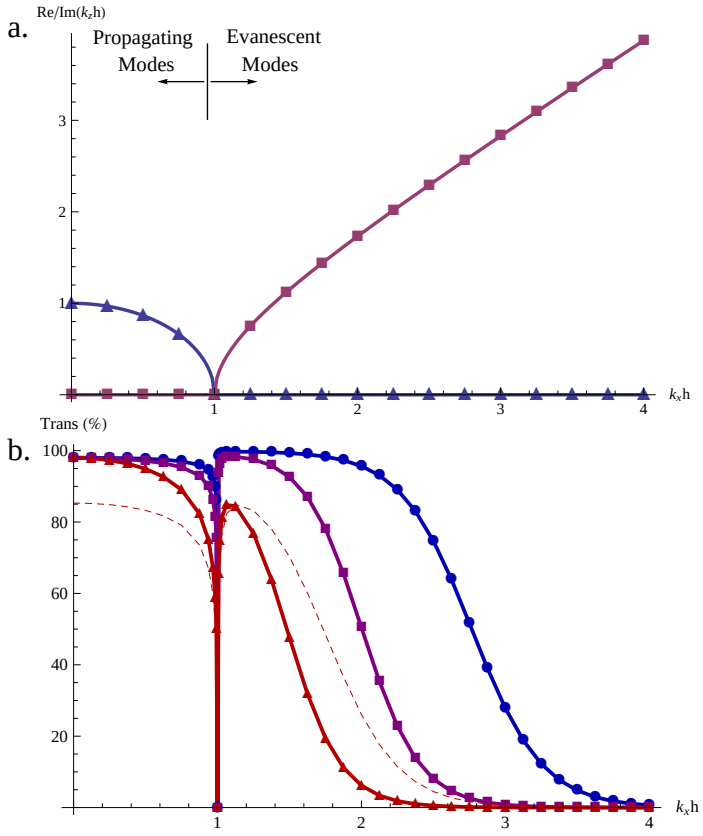

Figure 3.3: (a) Real (Triangle) and Imaginary (Square) parts of $k_z h$ and (b) transmission against $k_x h$ for $a = 0$ (Circle), 0.01 (Square) and 0.05 (Triangle), $\kappa = 10^{-2}$, $hk = 1$ and $\delta = 0.01$. Also shown in (b) by the dashed line is $a = 0$ and $\kappa = 0.08$.

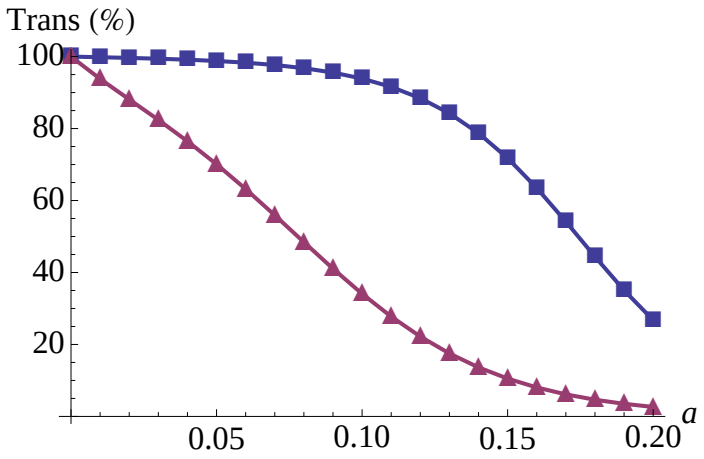

Figure 3.4: Transmission against a for a perfect lens with only one GRIN layer, of size a, plotted for a perfect lens with a GRIN front, nearest the source, boundary and planar rear boundary (blue squares) or for a perfect lens with a planar front boundary and a GRIN rear boundary (purple triangles) for $\kappa = 10^{-5}$, $k_x h = 10.3$, $k_z h = 1.95i$ and $\delta = 0.01$.

The dotted line shows the transmission coefficient for a lossy ($\kappa = 0.08$) LHM slab without layers ($a = 0$). Comparing this curve with that marked by triangles, it can be seen that a LHM with $\kappa = 0.01$ and large layer widths is out-performed by a LHM with a larger loss ($\kappa = 0.08$) but with smooth surfaces.

3.3.3 The perfect lens with asymmetric boundaries

Figure 3.4 illustrates the effects of having a single GRIN boundary on the perfect lens, whether that be on the front (closest to the source) or rear (closest to the image) surface of the lens. For every value of GRIN boundary size, a, the rear GRIN layer has a greater detrimental effect, showing that the perfect lens is far more sensitive to perturbations on its rear surface. The reasons for this are two-fold: firstly the electric field and its gradient are much greater at the rear surface (c.f. Fig. 3.2) and as such more sensitive to ohmic dissipation, secondly the evanescent amplification crucial to perfect lensing is due to a decaying evanescent wave from the rear surface, whilst this requires a primary boundary to set-up the restorative effect the dominant evanescent wave is generated by the second surface. Therefore in the construction of perfect lens', the rear surface will warrant greater attention as abnormalities there will have the greatest effect on transmission of evanescent modes.

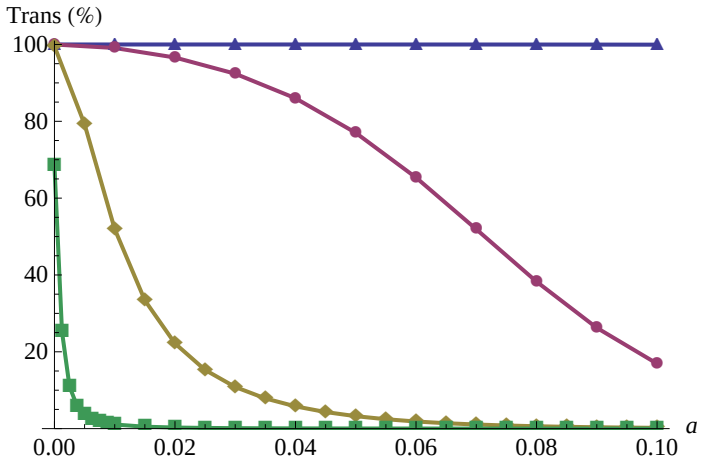

Figure 3.5: Transmission as a function of a for Figure of Merit ($= 1/\kappa$) $= 10^7$ (triangle), 10^5 (circle), 10^4 (diamond) and 10^3 (square), $k_x h = 10.3$, $k_z h = 1.95i$ and $\delta = 0.01$.

3.3.4 The perfect lens dependence on boundary quality and loss

Figure 3.5 shows the dependence of transmission on the diffuse layer width for different values of the loss. For losses of the order 10^{-4} or more, the presence of a small transitional layer causes a large drop in transmission but further increases in layer width have a diminishing effect. This is reminiscent of the logarithmic dependence exhibited by perturbations to the material parameters of LHM, as shown in [54, 13, 62].

To put the results of Fig. 3.5 into perspective, current LHM have figures of merit (FOM $= |\mathrm{Re}(n)/\mathrm{Im}(n)|$) $\sim$20, making even the green square curve (for which FOM $= 100$, $\kappa = 10^{-2}$) very optimistic. To add context to Fig. 3.5 if the wavelength of light used to generate the evanescent mode was from a red light source (650nm) then each increment of 0.01 in a represents a 52nm boundary layer width, for a violet light source (400nm) this increment represents a 32nm boundary layer. Therefore for use in the optical regime the boundaries of a perfect lens will need to be controlled down to the single nanometer scale. Hence until such a time that FOM's of $10^5 - 10^6$ are attained, the quality of a lens' boundaries will be vitally important to the recovery of evanescent modes.

3.4 Conclusion

This chapter has investigated the effect of imperfect boundaries upon a LHM lens using a GRIN model for the material parameters within transitional layers located at its surfaces. The resolving capacity of the lens has been quantified in terms of the layer thickness, which

is a proxy for the surface roughness. If the LHM is lossless, then the layers have no effect on the lens' ability to resolve perfectly. This is *not* the case if the LHM is lossy; the consequence of the localization caused by the layers is to preferentially dissipate high $k_x h$ modes. The detrimental effect of this upon resolution is similar to a nonlinearly enhanced value of loss in the bulk LHM.

The last two chapters have shown that surface imperfections will have a substantial impact on the recovery of both propagating and, especially, evanescent modes. This will become more important as the losses in manufactured LHM decrease through improved materials-science techniques - the current levels of loss dominating any other effects that are present and therefore masking the effects of the boundaries. This substantial impact is due to the physics governing the operation of the perfect lens being singular in nature, even a small layer serves to move the system away from resonance, leading to substantial falls in system performance. Indeed, the deterioration in super-resolving power due to rough/diffuse surface effects will prove to be an exacting deficiency to overcome, even if values of dissipation can be achieved that are orders of magnitude smaller than those currently attainable.

To further investigate the detrimental effects that surface roughness can have on a LHMs performance an alternative approach to the GRIN model will be scrutinized. GRIN modelling is advantageous in that it produces exact analytical results, but requires a deterministic approximation to the rough surface, replacing it with an effective medium. The next chapter will be concerned with true random surface profiles, prescribed by Gaussian statistics, and will utilize the short-wavelength limit of ray optics to explore the spatial effects given by a rough interface between RHM and LHM. The combination of these two methods, each given under different regimes of validity, will give a more complete picture of negative refraction and its interaction with surface aberrations.

Chapter 4

Negative refraction and rough surfaces: A new regime for lensing

4.1 Introduction

In the last two chapters non-perfect boundaries were approximated by GRIN layers. In this chapter the first steps are taken towards the interaction of a true rough surface with LHM: the action of a rough, but differentiable, interface upon the passage of rays between air and a left-handed medium is considered within the geometrical optics limit. It is shown that negative refraction brings rays to a focus at distances closer to the boundary than can be attained by conventional refraction. This effect enables a new mechanism for reflection to occur, even in media that are impedance matched. This is caused principally by rays undergoing two interactions with the interface via paths that pass exclusively through air or the left-handed medium. This new mechanism also enables the interesting result that a single roughened, impedance matched, interface can exhibit reflection. This is completely unique to LHM.

All of the key physics contained within this chapter can be investigated with the interactive demonstration included on the additional media CD appended to this thesis. The result of this chapter form the basis for the paper [63].

4.2 Focussing with negative refraction

The essence of the new focussing regime can be appreciated with reference to the cartoon of Figure 4.1. Locally the boundary between air and a medium of refractive index n is denoted by the smooth curve, $f(x)$. Pairs of rays, each distance $d/2$ from the apex of the curve

impinge upon the interface at angle θ to the local normal, where $\sin\theta = f'\left(1+f'^2\right)^{-1/2}$. A ray's direction incident upon the interface can be characterized by a unit vector $\mathbf{s_i}$ with components perpendicular and tangential to the local normal. If the second medium is right-handed, then Snell's Law stipulates that the sign of the components of the refracted ray, $\mathbf{s_r}$, do not change. Figure 4.1(a) shows this familiar situation with rays entering an optically denser medium with $n = 2$, with the rays being refracted towards the local normal to the surface. As $n \to \infty$, the direction of the ray becomes parallel to the normal but cannot pass through it, hence the point of confluence of rays has an asymptote, as shown by Figure 4.1(b). This can be seen qualitatively with the additional media CD's ray program - selecting an amplitude of 20 with n_2 varying between +1 and +20. For large values of n_2 the focal distance is insensitive to the precise value of n_2 as the focus' asymptote is approached.

The situation is different for LHM, for then the components of $\mathbf{s_r}$ tangential to the surface have different signs. Consequently rays are refracted to the other side of the normal, and move *away* from the normal with decreasing $|n|$. Figure 4.1(c) illustrates this for when the second medium has $n = -1$, where the focal distance is smaller than that attainable by *any* right-handed medium. The close focussing from a fashioned surface has also been demonstrated experimentally [64]. Indeed, as $|n| \to 0$ the focus moves arbitrarily close to the interface, as indicated by Figure 4.1(d).

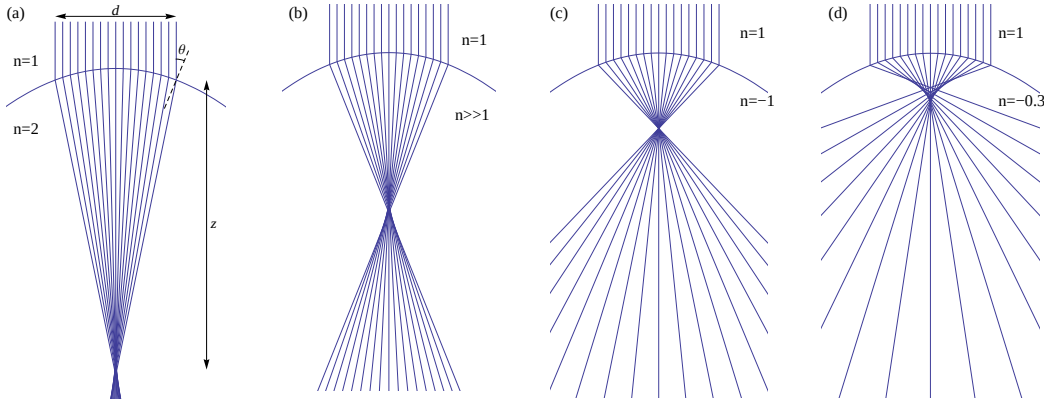

Figure 4.1: Ray propagation over a parabolic lenticular boundary going from air ($n = 1$) into $n = 2$, (a); an optically dense RHM, (b); $n = -1$, (c) and $n = -0.3$, (d).

4.3 Quantifying the focal length

The focal point of a pair of rays can be calculated by, c.f. Fig. 4.1(a),

$$\tan\Big(\frac{\pi}{2} - \theta + \varphi\Big) = -\frac{2z}{d} \tag{4.3.1}$$

where φ is the refracted angle. Using Snell's law, φ can be expressed in terms of θ:

$$\sin\theta = n\,\sin\varphi, \tag{4.3.2a}$$

$$\cos\varphi = \left(1 - n^{-2}\sin^2\theta\right)^{1/2} \tag{4.3.2b}$$

then the focal distance can be calculated through employing the trigonometric formulae in (4.3.1):

$$\frac{2z}{d} = \frac{\sin\theta + n\,\cot\theta\left(1 - n^{-2}\sin^2\theta\right)^{1/2}}{\cos\theta - n\left(1 - n^{-2}\sin^2\theta\right)^{1/2}}, \tag{4.3.3}$$

therefore

$$\frac{z}{d} = \frac{n\sin\theta + n^2\,\cot\theta\left(1 - n^{-2}\sin^2\theta\right)^{1/2}}{2\,n\,\cos\theta - 2\,n^2\left(1 - n^{-2}\sin^2\theta\right)^{1/2}} \tag{4.3.4}$$

which then implies that

$$\frac{z}{d} = \frac{n\sin\theta + \cot\theta\left(n^4 - n^2\sin^2\theta\right)^{1/2}}{2\,n\cos\theta - 2\left(n^4 - n^2\sin^2\theta\right)^{1/2}}. \tag{4.3.5}$$

In Figure 4.2, equation (4.3.5) is plotted as a function of n for different values of θ, the angle between the incoming ray and the local normal to the surface. A cursory inspection of (4.3.5) shows that it exhibits quantitatively different behaviours for n positive and negative. When $n > 1$, the disposition of the normals can bring the rays to a focus by customary means. The asymptote for the focus' location as $n \to \infty$ is $-\frac{1}{2}\cot\theta$ which is shown by the horizontal dashed lines. When $0 < n < 1$, the pair of rays either have angle of incidence that is greater than the local normal and undergo total internal reflection within the air, or enter the second medium but diverge from each other (c.f. the ray program with a surface amplitude of 52 and $n_2 = 0.6$).

When $n < 0$, the rays are refracted to the other side of the normal, and the asymptote for the focus when $n \to -\infty$ is the same as that for the right-handed case. However, as $|n|$ decreases, the focal point moves closer towards the interface. Indeed, there is a critical angle for which the rays traverse each other's paths and exit the second medium back into air; i.e. a double-passage path, symptomatic of enhanced backscatter [65, 66].

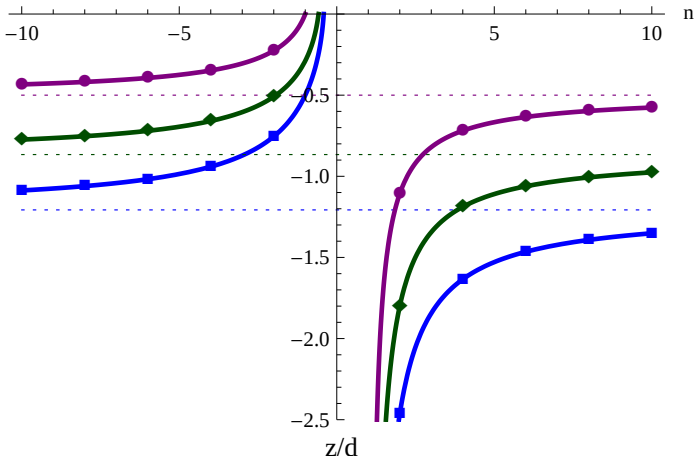

Figure 4.2: The focal length z of two rays separated by d, incident from air onto the surface at angle θ from the normal, shown as a function of the refractive index of the second medium, n. Shown are the cases $\theta = \pi/8$ (Blue Squares), $\pi/6$ (Green Diamonds), $\pi/4$ (Purple Circles). Also shown by the dashed line for each case is the large n asymptote, $-\frac{1}{2}\cot\theta$.

4.4 Backscatter and Reflection

Figure 4.3(a) depicts the two mechanisms by which double passage geometries can occur. The case for when the second medium can be left- or right-handed but has $|n| < 1$ is shown in Fig. 4.3(a)-(i). Here the ray undergoes total internal reflection on each encounter with the second medium, the ray remaining in air throughout. Figure 4.3(a)-(ii) shows the geometry for another class of double-passage for rays that can only occur if $n < 0$ where the ray is refracted into the second medium and passes through it before its second encounter with the interface, whereupon it is refracted back into air. Henceforth we shall refer to these paths as being of type (i) and (ii) respectively. These two types of mechanisms can both be observed in the multiple ray tracing program: for an example of solely type (i) paths - try a surface amplitude = 69, $n_2 = 0.5$; whereas for solely type (ii) paths - amplitude = 96, $n_2 = -1.4$. For an example containing both types of paths - select an amplitude = 68, $n_2 = -0.4$. In the last example changing to the option showing a single ray path and laterally varying the ray location shows the full range of rays that are generated by this interface.

The relative importance of these two mechanisms can be assessed using a ray tracing simulation from a 1-dimensional corrugated Gaussian random surface with a Gaussian autocorrelation function $\rho(x) = \sigma^2 \exp\left(-\frac{1}{2}x^2/\ell^2\right)$, formed from 3000 realizations with ~ 5000 rays in each case. The surface has zero mean, variance σ^2 and correlation length ℓ. When

$n > 1$, reflection cannot occur through interactions with the interface alone; rays can only pass back through the interface into air via some other agency, like a reflecting surface located in the second medium. Because these situations have been considered elsewhere, e.g. [67], we confine discussion to the regime $n < 1$. As the case of impedance matched media has been examined in the preceding chapters it will again be adopted here, accordingly a ray is either completely transmitted or reflected (due to total external reflection). Consequently, within the ray approximation, the reflected intensity is essentially the same as the density of the ray paths themselves.

All paths that contribute to the reflected direction have been enumerated and are displayed as a function of the refractive index of the second medium in Figure 4.3(b). A ray is considered to be backscattered if its final trajectory is within θ_ϵ of a true backscattered ray, in the case of Figure 4.3(b) $\theta_\epsilon = 0.1$ radians. The curve labelled by (yellow) diamonds in Figure 4.3(b) is for $\sigma/\ell = 0.25$. This exhibits a peak for $n \approx -0.5$ caused principally by those paths of type (ii). As the surface roughness increases, shown by the (purple) circles corresponding to $\sigma/\ell = 0.5$, the fraction of rays in the back-scattering direction increases

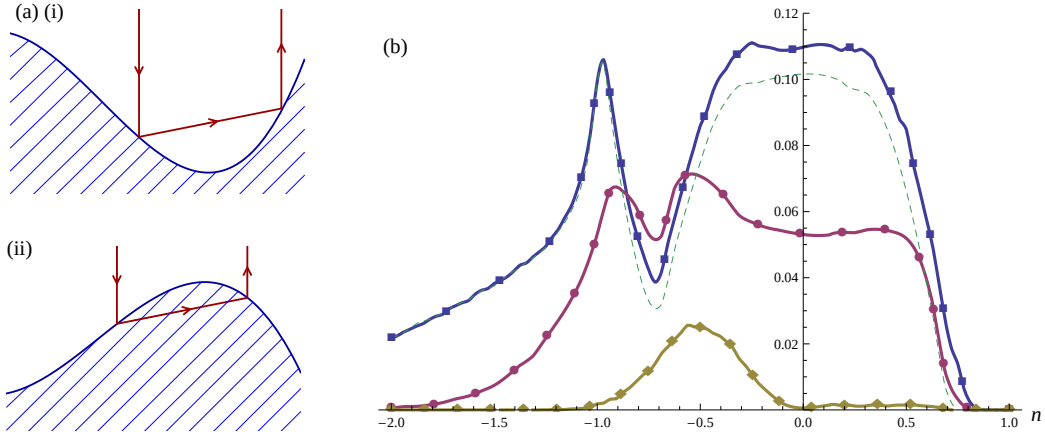

Figure 4.3: (a) Illustrations of, (i), traditional reflection which can occur when $|n| < 1$ and, (ii), the new backscattering mechanism which can only occur for $n < 0$. (b) Numerical simulations of the average reflection from a normal incidence beam on a one dimensional Gaussian rough surface as a function of the refractive index in the second medium, n. Reflection is measured as the average percentage of rays that return to the observer within a cone of angle, $\theta_\epsilon = 0.1$, with specular scattering near $n = 0$ removed for clarity. Shown in the figure are the cases $\sigma/\ell = 0.25$ (Yellow Diamonds), 0.5 (Purple Circles), 1.0 (Blue Squares), for this last case the contribution due solely to double scattering is shown by the dashed line. Symbols are used to delineate the curves and do not indicate data points.

overall but now comprises two features. The peak occurring around $n \approx -0.9$ is formed predominantly by paths of type (ii). The combination of paths of type (i) and (ii) are the cause of the second peak at $n \approx -0.5$, whereas the plateau region for values of n greater than this is due exclusively to paths of type (i). Increasing the average slope further to $\sigma/\ell = 1$, shown by the (blue) squares, causes the density to increase again, with the peak due to paths of class (ii) occurring at the slightly smaller value of $n \approx -1.1$. However the broader peak due to paths of type (i) has become distinct from those of type (ii), being essentially constant over the range $|n| \leq 0.5$. The dotted (green) line shows the contribution due to double-passage rays alone, and these comprise the greatest proportion of the total. This is also true for the other cases but these are not shown for clarity.

The propensity for the type (ii) peak to move towards more negative values of n with increasing slope can be understood with reference to Figure 4.2. The steeper the surface slopes, the wider is the range of incident angles θ into the second medium, and it can be seen in Figure 4.2 that the intercept of the curves on the n-axis occurs at increasingly negative values of n as θ increases.

4.5 Angular distribution of transmitted and reflected ray density

An angular plot of the ray density is shown in Figure 4.4(a) for rays incident upon a surface at $\pi/20$ (9^o) from the normal direction. The two overlaying plots correspond to the second medium having $n = +0.25$ (dotted blue) and $n = -0.25$ (solid red) and for a very large surface slope $\sigma/\ell = 8$, chosen to illustrate the new mechanism at work rather than as a model of an actual case. Both cases show some transmission into the second medium, but this is substantially reduced for the left-handed case. Both curves have almost identical backscattering characteristics for large angles where shadowing effects dominate, and feature a broad enhancement in the ray density occurring in the specular direction, but this is *increased* for the left-handed case. Both show a back-scattering enhancement and again this is increased for the left-handed case because paths of both types can occur whereas for the RHM contributions arise only from those paths of type (i). The broader backscattering lobe centred at $\approx -15^o$ occurs only for the left-handed case and is attributable to paths of type (ii).

Figure 4.4(b) shows the angular distribution of the ray density for rays that are incident

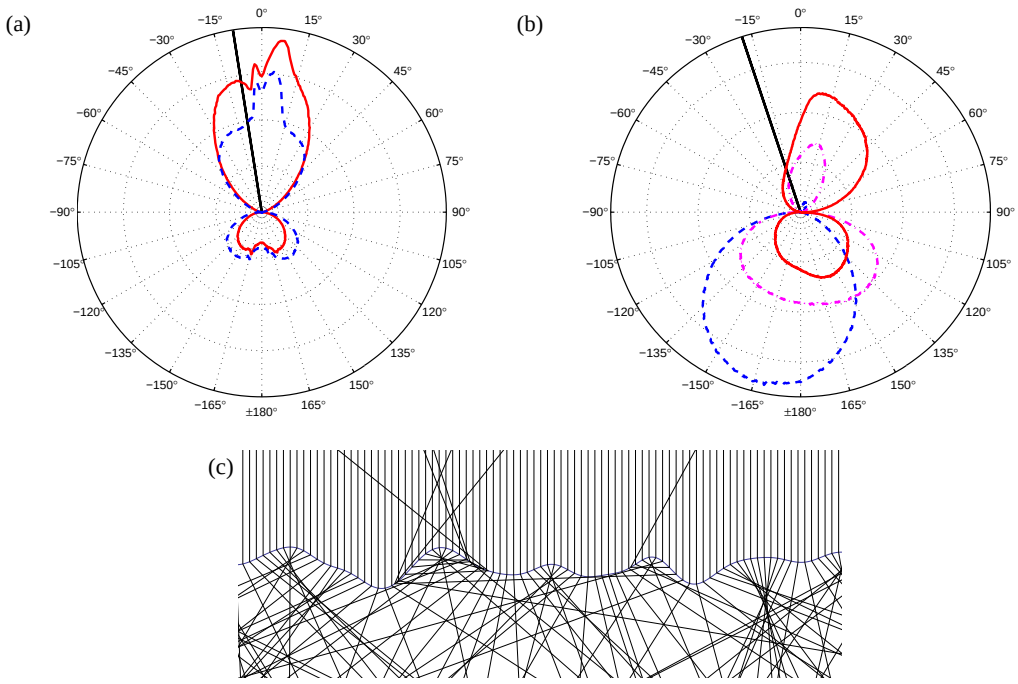

Figure 4.4: Mean angular ray scattering from a Gaussian rough interface. (a) between air and $n = 0.25$ (dotted blue) and $n = -0.25$ (solid red), here $\sigma/l = 8$; also shown (black line) is the angle of incidence, $\pi/20$. (b) between air and $n = -1$ for $\sigma/l = \frac{1}{4}$ (dotted blue), $\frac{1}{2}$ (dot-dashed purple) and 1 (solid red); also shown (black line) is the angle of incidence, $\pi/10$. (c) an instance of a Gaussian surface with $\sigma/l = 0.25$ and $n = -1$, with the ray density decreased for illustrative purposes, showing examples of type (ii) scattering and near-surface focusing.

from air at an angle $\pi/10$ (18^o) from the normal direction onto a half-space of $n = -1$ with Gaussian random interfaces of different rms slopes. When $\sigma/\ell = \frac{1}{4}$, shown by the dotted (blue) curve, most of the rays pass into the LHM with the density spread about the negative refraction direction. There is also a very small reflection in the specular direction which is barely discernible in the plot. Increasing the rms surface slope to $\sigma/\ell = \frac{1}{2}$, shown by the dotted-dashed (purple) curve reduces the density of rays passing into the LHM, but these are spread through a greater angular range with tendency to be centred about the incident direction rather than the negative refractive direction. The reflection into air is increased and is in the specular direction. Increasing the slope further $\sigma/\ell = 1$, shown by the solid (red) curve, further reduces the rays passing into the LHM and narrows their spread about the incident direction at the expense of the increased reflection which also broadens further. The reason for transmission occurring in the incident direction with increasing roughness is essentially a shadowing effect - the fraction of the illuminated surface being increasingly

perpendicular to the incident direction.

The essential novelty of the results displayed in Figure 4.4(b) is that reflection can occur in media that are impedance matched through the mechanism of *multiple refractions* with the roughened interface, and this has its roots in the extreme bending of the rays when they interact with a LHM, as quantified earlier. No such mechanism exists for right-handed media even if they are of magnetic character and impedance matched.

4.6 Conclusions

This chapter has identified a new focussing regime for rays that interact with a roughened but differentiable interface between left- and right-handed media. The rays can focus at smaller distances from the interface due to the negative refractive effects, this being especially pronounced if $|n| < 1$. This is an effect distinct from the familiar total internal reflection caused by the interaction of light from an optically denser medium with a less dense one, principally because of the negative refraction caused by LHM. Moreover, non-Fresnel reflection can occur if $n < 1$, principally through multiply refracted paths of the rays. Consequently an *impedance matched* configuration involving a LHM (such as the perfect lens) with a roughened interface can still display reflection. Distinct reflection signatures are produced depending on whether the ray paths pass through the second medium or air before leaving the vicinity of the interface. Insofar as transmission into the second medium is concerned, increasing the rms surface slope erodes the negative refraction effect. The refracted ray behaves increasingly as if it is in a RHM with increasing σ/ℓ. Here we have assumed that the second medium is lossless to illustrate the novel effects, but the presence of losses will significantly attenuate those rays with long path-lengths in the LHM, and will suppress the enhanced back-scattering effect.

Geometrical optics gives a qualitative picture of light propagation into both LHM and RHM, giving information on both the focal points and approximate intensity profiles, through the ray density. However it cannot encapsulate diffraction and interference effects - geometric optics occurring through the small λ, or large k, limit. The next chapter addresses this issue by relaxing the high k approximation. This will be done firstly through the use of the physical-optics approximation of, small σ, Rice theory [68] and secondly via large-scale Monte-Carlo simulations that can treat larger surface deformations. These two routes will give more accurate results for lensing and also enable higher order intensity statistics to be calculated within the second media, illustrating fluctuation effects.

Chapter 5

Enhanced twinkling within the perfect lens

5.1 Introduction

The last chapter demonstrated that a random boundary, when treated within the geometrical optics limit, causes incident rays to focus at distances closer to the interface than can be attained by any right-handed medium [63] and introduces a mechanism whereby light is back-scattered through multiple refraction, so less light enters the lens. This chapter removes the short-wavelength approximation and instead addresses the effects of surface roughness using physical-optics and in so doing it highlights several unexpected and critical differences between the optics of right- and left-handed media that are introduced by randomness.

The methodology of this chapter is twofold: firstly, after deriving Huygens' principle for magnetic media, the solution to the Rice (perturbation) approximation for magnetic media is obtained. This shows that a rough boundary on a LHM (when compared to its RHM counterpart) causes greater scintillations, or 'twinkling' within the medium, and that the scattered field converges to Gaussian noise over shorter optical propagation distances. When the surface is a Gaussian process, the scattered field is shown to evolve from a real Gaussian process near the surface into a complex Gaussian process as distance into the second media increases.

The second approach of this chapter is to utilise large-scale Monte-Carlo simulations to determine the intensity statistics within the second media for larger surface roughnesses than can be treated by Rice theory. These simulations show that illuminating a roughened

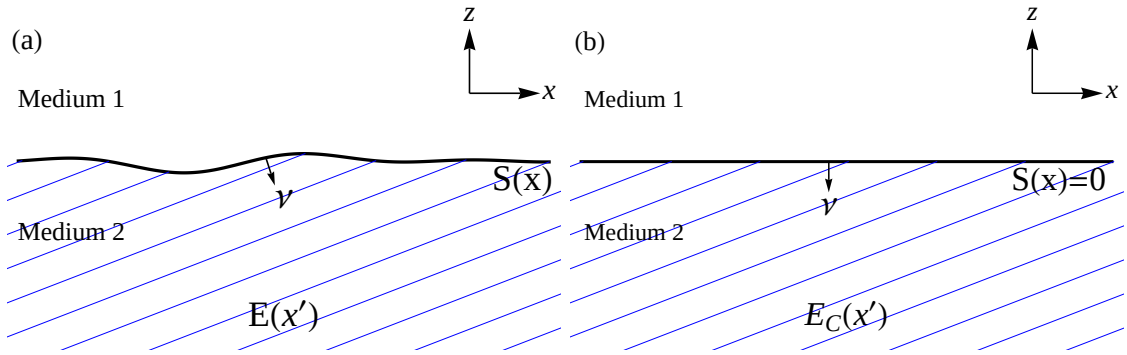

Figure 5.1: Illustrations of the surface, $S(x)$, and its inward normal, ν, for both (a) a rough interface and (b) a planar boundary.

interface between air and a LHM produces a regime for enhanced focussing of light close to the boundary, this generates caustics that are brighter, fluctuate more, and cause Gaussian speckle at distances closer to the interface than in right-handed matter.

5.2 Magnetic Huygens' Principle

The novel features of LHM, such as negative refraction and perfect lensing, occur through the *combined* effect of the permeability and permittivity [2], therefore to apply physical-optics to quantify the diffractive and interference effects produced by a roughened surface that separates right- and left-handed half-spaces requires reformulating Huygens principle [8] to account for the (necessarily) magnetic nature of LHM. Appendix B detailed the calculation of the Green's function in this situation. Green's theorem then gives the exact expression for the field E at any location $\mathbf{x}'$ to be,

$$E(\mathbf{x}') = \int_S \left(E_2(\mathbf{x}) \frac{\partial \psi(\mathbf{x}, \mathbf{x}')}{\partial \nu} - \psi(\mathbf{x}, \mathbf{x}') \frac{\partial E_2(\mathbf{x})}{\partial \nu} \right) dl \tag{5.2.1}$$

where $\psi(\mathbf{x}, \mathbf{x}')$ is the free-space Green's function

$$\psi(\mathbf{x}, \mathbf{x}') = \left(\frac{-1}{4\,i} \right) \mathrm{H}_0^{(1)}(k_2 \left| \mathbf{x} - \mathbf{x}' \right|); \tag{5.2.2}$$

$\mathrm{H}_0^{(1)}$ being the Hankel function of the first kind; S is the surface between the two media as shown in Fig. 5.1 (the integral taken just inside the second medium); $\boldsymbol{\nu}$ is the normal to S pointing into the second medium; l is the arc-length along the surface; E_2 is the electric field measured arbitrarily close to the surface, but within the second medium; k_2 is the wavenumber in the second medium.

To express the electric field E_2 that appears in the integral of (5.2.1) in terms of the incident field, the continuity equations (2.3.1) give that

$$E \quad \text{and} \quad \frac{1}{\mu}\frac{dE}{d\nu} \tag{5.2.3}$$

must be continuous across an interface. Therefore

$$E_1 = E_2 \quad \text{and} \quad \frac{1}{n_1}\frac{dE_1}{d\nu} = \frac{1}{n_2}\frac{dE_2}{d\nu}, \tag{5.2.4}$$

for impedance matched media, i.e. where $\mu = \epsilon = n$, and where E_1 is the incident electric field measured arbitrarily close to the surface, but within the first medium. Combining (5.2.1) and (5.2.4) gives the electric field in the second medium as a integral of the incident field along the surface:

$$E(\mathbf{x}') = \int_S \left(E_1(\mathbf{x}) \frac{\partial\, \psi(\mathbf{x}, \mathbf{x}')}{\partial \nu} - \frac{n_2}{n_1} \psi(\mathbf{x}, \mathbf{x}') \frac{\partial E_1(\mathbf{x})}{\partial \nu} \right) dl. \tag{5.2.5}$$

The additional effects of magnetism can now be seen to originate from the influence of the ratio n_2/n_1 appearing in the second term in (5.2.5) which derives from matching the electric displacement vector at the surface. Moreover, the refractive index, n_2, also appears within the Green's function. Thus it is the change of the sign of these terms that enables negative refraction and perfect lensing to occur. The formulation stated above is for impedance matched media, in accord with the scope of this chapter, however this condition can easily be relaxed by the inclusion of a reflected term and a transmission coefficient in the boundary conditions, whereupon the magnetic Fresnel coefficient [69] then multiplies the integrand in (5.2.5):

$$E(\mathbf{x}') = \int_S T(\mathbf{x},\, E_1,\, S(\mathbf{x})) \left(E_1(\mathbf{x}) \frac{\partial\, \psi(\mathbf{x}, \mathbf{x}')}{\partial \nu} - \frac{\mu_2}{\mu_1} \psi(\mathbf{x}, \mathbf{x}') \frac{\partial E_1(\mathbf{x})}{\partial \nu} \right) dl, \tag{5.2.6}$$

where $T(\mathbf{x},\, E_1,\, S(\mathbf{x}))$ is the transmission coefficient [69], dependent on the incident field, the surface profile and its slope at the point $\mathbf{x}$.

5.3 Rice Theory

Rice theory treats those surfaces where the rms surface height, σ, is small compared with the wavelength of the incident field, λ, [68]. This section first treats the scattered electric field, E_S - defined as being the difference between the observed field, E and the field that would derive from a perfect planar interface ($\sigma = 0$) - termed the coherent field, E_C, i.e.

$$E_S = E - E_C. \tag{5.3.1}$$

As such E_S measures the perturbation of the coherent field that produces the observed field, with $E_S \to 0$ as the surface imperfections are removed ($\sigma \to 0$).

To calculate the statistics of E_S within the Rice approximation the Huygens' principle, modified to include magnetic media - (5.2.5), will be utilized. From this both E and E_C can be calculated analytically. Equation (5.3.1) then gives E_S and by applying the Rice approximation $\sigma \ll \lambda$, the scattered intensity, I_S, and second scattered intensity moment, $\langle I_S^2 \rangle / \langle I_S \rangle^2$, can be calculated. From this the intensity for the total field, I, and the second total intensity moment, $\langle I^2 \rangle / \langle I \rangle^2$, within the Rice limit are developed.

5.4 Scattered Rice Field

A corrugated interface will now be examined under the Rice approximation. The interface is characterised by the profile function $z = S(x)$ which is illuminated by a harmonic plane-electromagnetic wave $\mathbf{E}_i = \exp(-i\,(\omega t + kz))\,\hat{\mathbf{y}}$ that propagates in the negative z-direction with wave-number $k = \omega/c$ through a right-handed medium with refractive index $n = 1$, and with polarization state oriented parallel to the surface corrugations. The refractive index in the second medium is n_2, which can be of either sign, and the wavenumber is $k_2 = n_2\, k$. The electric field then can then be written as

$$E(\mathbf{x}') = \int \left(e^{-ikS(x)} \frac{\partial \psi(\mathbf{x}, \mathbf{x}')}{\partial \nu} - \frac{n_2}{n_1} \psi(\mathbf{x}, \mathbf{x}') \left. \frac{\partial e^{-ikz}}{\partial \nu} \right|_{z=S(x)} \right) dl, \tag{5.4.1}$$

the normal and unit normal that points into medium 2, being given by

$$\boldsymbol{\nu} = \big(S'(x), 0, -1\big) \quad \text{and} \quad \hat{\boldsymbol{\nu}} = \frac{(S'(x), 0, -1)}{(S'(x)^2 + 1)^{1/2}}. \tag{5.4.2}$$

Utilizing

$$\frac{\partial e^{-ikz}}{\partial \nu} = \nabla\Big(e^{-ikz}\Big) \cdot \hat{\boldsymbol{\nu}} = \Big(0, 0, -ike^{-ikz}\Big) \cdot \hat{\boldsymbol{\nu}} = ik \exp(-ikz) \left(S'(x)^2 + 1\right)^{-1/2} \tag{5.4.3}$$

and that the line element can be written as $dl = \left(S'(x)^2 + 1\right)^{1/2} dx$, then the electric field in the medium can be written as

$$E(\mathbf{x}') = \int \left(e^{-ikS(x)} \left(\nabla \psi \cdot \boldsymbol{\nu}\right) - \frac{n_2}{n_1} \psi \left(ike^{-ikS(x)} \right) \right) dx. \tag{5.4.4}$$

The aim of this section is to derive the scattered electric field, E_S, given by the electric field, E - (5.4.4), with the coherent field, E_C, subtracted from it. The coherent field is the field produced when the rough boundary is replaced by a perfect planar interface, i.e.

$S(x) = 0$ for all x and therefore $\boldsymbol{\nu} = -\mathbf{e_z}$. Using (5.4.4), with $S(x) = 0$ for all x, the coherent field can be calculated to be

$$E_C(\mathbf{x}') = \int \left(- \left(\nabla\psi \cdot \mathbf{e}_z\right)|_{S(x)=0} - ik\frac{n_2}{n_1}\, \psi|_{S(x)=0} \right) dx. \tag{5.4.5}$$

The scattered field is therefore

$$E_S = E - E_C = \int \left(e^{-ikS(x)} \left(\nabla\psi \cdot \nu\right) + \left(\nabla\psi \cdot \mathbf{e}_z\right)|_{S(x)=0} \right) - ik\frac{n_2}{n_1} \left(e^{-ikS(x)}\psi - \psi|_{S(x)=0} \right) dx \tag{5.4.6}$$

using

$$\boldsymbol{\nu} = \left(S'(x), 0, -1\right) = S'(x)\mathbf{e}_x + \boldsymbol{\nu}_s = S'(x)\mathbf{e}_x - \mathbf{e}_z. \tag{5.4.7}$$

Under the Rice approximation it is assumed that $S(x) \ll \lambda$ for all x, and this implies that

$$e^{-ikS(x)} \sim 1 - ikS(x) + O\left(\frac{S^2(x)}{\lambda}\right). \tag{5.4.8}$$

Therefore the small $S(x)$ expansion of (5.4.6) is given by

$$E_S = \int \left(S'(x)\, \left(\nabla\psi \cdot \mathbf{e}_x\right)|_{S(x)=0} + S(x) \left(- \left.\frac{d\left(\nabla\psi \cdot \mathbf{e}_z\right)}{dS}\right|_{S(x)=0} + ik\, \left(\nabla\psi \cdot \mathbf{e}_z\right)|_{S(x)=0} \right.\right.$$
$$\left.\left. - \; ik\frac{n_2}{n_1}\, \left.\frac{d\psi}{dS}\right|_{S(x)=0} - k^2\frac{n_2}{n_1}\, \psi|_{S(x)=0} \right) \right) dx, \tag{5.4.9}$$

where terms of order $S^2(x)$ or higher have been neglected.

5.5 Second Intensity Moment

With (5.4.9) the scintillation statistics can now be derived for Rice theory. The scintillation of a field is a measure of fluctuation, or 'twinkling', of the intensity of a field, defined by $\left\langle I^2 \right\rangle / \left\langle I \right\rangle^2 - 1$, [70]. In this section the closely related second intensity moment, $I^{[2]} = \left\langle I^2 \right\rangle / \left\langle I \right\rangle^2$, will be examined. Appendix C details the lengthy calculation required to determine the second intensity moment within the Rice approximation, this utilizes the notation

$$\mathrm{G}(i, X, Y) := \sigma^2 \iint g^{(i)}(x_2 - x_1) X(x_1) Y(x_2)\, dx_1\, dx_2 \tag{5.5.1}$$

and

$$E_S = \int \left(S(x)A(x) + S'(x)B(x) \right) dx, \tag{5.5.2}$$

with A and B being identified with terms appearing in (5.5.2) and (5.4.9) and the superscript on g denotes the order of differentiation. For a Gaussian rough surface with correlation

function $g(\tau) = \exp\left(-\frac{1}{2}\tau^2/\ell^2\right)$, where ℓ is the autocorrelation length, illuminated at normal incidence, the scintillation index components, for the scattered and total field are, (see Appendix C),

$$\frac{\langle I_S^2\rangle}{\langle I_S\rangle^2} = 2 + \frac{|\mathrm{G}(0,A,A)|^2 - 2\,\Re e(\mathrm{G}(2,B,B)\,\mathrm{G}^*(0,A,A)) + |\mathrm{G}(2,B,B)|^2}{\left(\mathrm{G}(0,A,A^*) - \mathrm{G}(2,B,B^*)\right)^2}, \tag{5.5.3}$$

$$\langle I_S\rangle = \mathrm{G}(0,A,A^*) - \mathrm{G}(2,B,B^*)\,, \tag{5.5.4}$$

$$\langle I\rangle = \langle I_S\rangle + I_C, \tag{5.5.5}$$

and

$$\begin{aligned}\langle I^2\rangle = \langle I_S^2\rangle \quad &+ \quad 4\,\mathrm{G}(0,A,A^*)\;I_C - 4\,\mathrm{G}(2,B,B^*)\;I_C + 2\,\Re e\Big(\mathrm{G}(0,A,A)\;(E_C^*)^2\Big) \\ &- \quad 2\,\Re e\Big(\mathrm{G}(0,B,B)\;(E_C^*)^2\Big) + I_C^2,\end{aligned} \tag{5.5.6}$$

with the scattered field, E_S, being the total field, E, minus the coherent field, E_C - the field resulting from a perfect planar surface. With this definition E_S can be viewed as the perturbation to E_C that produces the observed field, E. The equations above also make use of the quantities: I - the total intensity, σ - the standard deviation of the surface, I_C - the intensity of the coherent field and I_S - the intensity of the scattered field.

5.6 Scintillation Index result within the Rice Approximation

Figure 5.2 shows the total scintillation indices as a function of distance into the second medium for different values of n_2. As distance into the second medium increases from zero neighbouring parts of the surface constructively interfere resulting in larger scintillations. This continues until many independent portions of the surface contribute. The central limit theorem then applies and the scintillations eventually saturate to Gaussian noise.

Comparing the left-handed cases of $n_2 = -3$ and -2 with their right-handed counterparts ($n_2 = 3$ and 2), shown in Figure 5.2 (a) and (b), it can be seen that in each pairing the peak value occurs at the same optical depth but that the scintillations are greater for LHM. The scattered field then saturates faster to Gaussian noise and the scattered field then becomes negligible compared with the coherent field, in this limit the scintillation index tends to zero, implying that the intensity is dominated by the non-fluctuating coherent field. Comparing the far-field gradients in both cases shows that this process occurs with shorter optical depth for LHM than for RHM. In all cases the optical depth of the scintillation peak decreases as $|n|$ reduces.

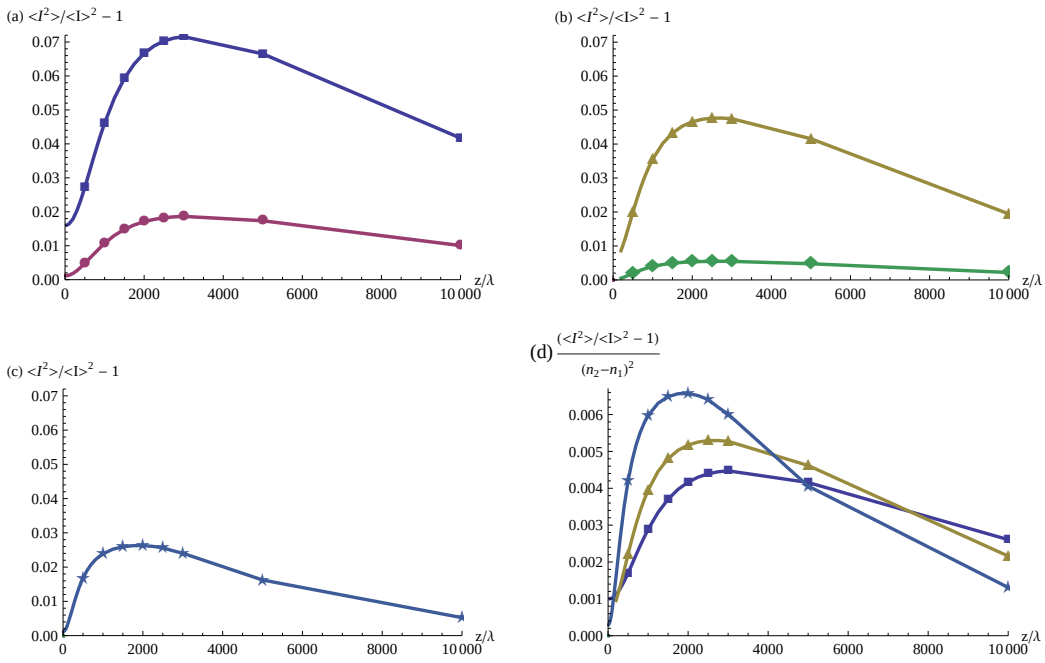

Figure 5.2: Scintillation index for the total field against optical depth into the second medium with $\ell = 10\lambda$ and $\sigma = 0.0125\lambda$ for the cases of (a) $n_2 = -3$ (dark blue squares) and 3 (purple circle); (b) $n_2 = -2$ (yellow triangles) and 2 (green diamonds); (c) $n_2 = -1$ (light blue stars). (d) shows the Scintillation index with a multiplicative factor of $(n_2 - n_1)^{-2}$, with this normalization the cases of $n_2 = -3$ and 3 become indistinguishable (dark blue squares) as do the cases of $n_2 = -2$ and 2 (yellow triangles). Also shown in (d) is the case of $n = -1$ (light blue stars). In all cases the marked data points are numerical evaluations of the functions involved, the curves comprising of interpolations between them.

A feature of the Rice approximation is that the peak value of the fluctuations coincides for right- and equivalent left-handed media. This can be explained by the following argument. Consider a ray incident on a surface inclined at a small angle $\delta\theta$ from a level plane. Assume that the angle of slope is constrained so that $|\delta\theta| < \theta_M$ where $\theta_M \ll 1$, c.f. Figure 5.3 (a). The resulting range of angles in the second medium will lie in a cone defined from Snell's law by the angle φ:

$$\begin{aligned} \varphi &= \arcsin\left(\tfrac{n_1}{n_2}\sin\theta_M\right) \\ &\sim \arcsin\left(\tfrac{n_1}{n_2}\theta_M\right) \\ &\sim \tfrac{n_1}{n_2}\theta_M. \end{aligned} \tag{5.6.1}$$

Although each individual ray takes a different path, depending on the sign of the refractive indices involved, the overall cone maintains the same shape and extent irrespective of the sign of n_2. Therefore interactions between two points on the surface can only occur after

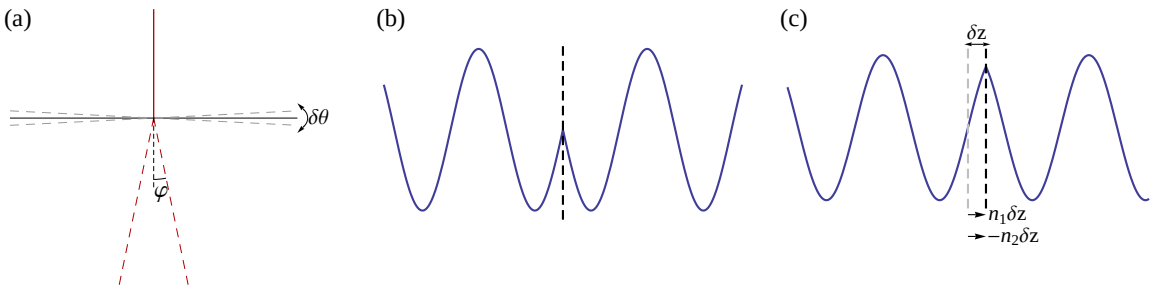

Figure 5.3: (a) An illustration that a change in slope angle, $\delta\theta$, causes a change, φ, in the resulting ray. (b) and (c) illustrate that a slight change in the placement of the surface, δz, means that the phase of the resulting wave loses a $n_2\,\delta z$ contribution and gains a $n_1\,\delta z$ contribution. Therefore the phase change in the resulting wave is $(n_1 - n_2)\delta z$.

traversing the same optical depth, irrespective of the sign of n_2, i.e. the closest possible interaction from two points on the surface, which occurs when the cones from the two points, as defined in (5.6.1), intersect. It should be stressed that this only occurs in the small σ limit, it will be seen in the next section that this does not hold for larger values of σ. Equation (5.6.1) also demonstrates why the peak occurs at distances closer to the surface as $|n_2|$ decreases, for then the cone of angles widens allowing surface interactions to occur closer to the surface.

The observation that LHM cause higher scintillations and decay faster as the optical depth increases is due to the scattered field being proportional to $(n_1 - n_2)$ times any surface perturbations, c.f. Figure 5.3 (b) and (c). Figure 5.3 (b) and (c) illustrates that a positive surface perturbation of size δz means the phase of the resultant wave changes by an amount $(n_2 - n_1)\,\delta z$. Consequently the scattered field can be expressed as

$$E_S = E - E_C = E_C \exp(ik(n_2 - n_1)\delta z) - E_C = E_C \left(\exp(ik(n_2 - n_1)\delta z) - 1\right). \tag{5.6.2}$$

Under the Rice approximation $k\,\delta z \ll 1$ so that

$$E_S \sim ik(n_2 - n_1)\,\delta z\, E_C, \tag{5.6.3}$$

i.e. that

$$E_S \propto (n_2 - n_1)\,\delta z. \tag{5.6.4}$$

Therefore any negative index serves to amplify the perceived surface perturbations, as compared with its right-handed counterpart. Fig. 5.2 (d) allows for this effect to be more clearly seen, by introducing a multiplicative factor of $(n_1 - n_2)^{-2}$ (the squared term since $I_S \propto (n_2 - n_1)^2$). The curves for $n = -3$ and 3 become indistinguishable, as do the curves

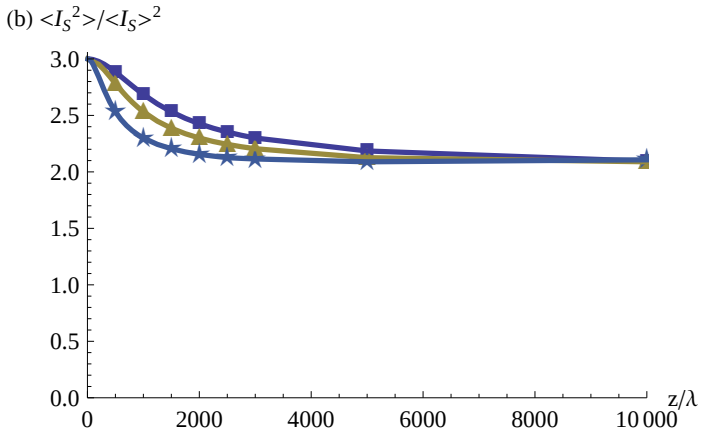

Figure 5.4: Second intensity moment for the scattered field with $\ell = 10\lambda$ for the cases of $n = -3$ and 3 (dark blue squares), $n = -2$ and 2 (yellow triangles) and $n = -1$ (light blue stars). The scattered scintillation index of (b) is insensitive to the sign of n, except in the singular case of $n = 1$. Again markers indicate data points.

for $n = -2$ and 2. This illustrates that, within the Rice approximation, the dependence on the sign of n_2 only enters into the scintillation index through the factor of $(n_2 - n_1)^2$ via the mechanism described above.

Figure 5.4 shows the scintillation index for the scattered field. In all cases this begins at 3 at the interface and then decreases towards 2 as optical depth increases. This shows the changing nature of the scattered field throughout the second medium: near the surface it is dominated by the surface statistics, which is a real Gaussian process giving rise to the scintillation index of 3 [71] whilst for larger distances the field derives from many independent contributions from the surface, a complex Gaussian process, resulting in Gaussian noise, giving a scintillation index of 2 [71]. As $|n_2|$ decreases the fields interact closer to the surface and the scattered scintillation index saturates to Gaussian noise faster, c.f. (5.6.1) and (4.3.5).

5.7 Numerical Calculation of the Field

The small σ asymptotic analysis of Rice theory has given rise to many interesting results that serve to highlight where differences between left- and right-handed media can be expected to occur. To treat larger σ requires a numerical approach however. This will be detailed in the following section.

The electric field is evaluated numerically by encoding in C++ Huygens' principle, as

expressed in (5.2.5). The computational method proceeds as follows: generate a Gaussian rough surface of prescribed correlation function, using the Fourier Transform method [70], the integral (5.2.5) is then computed using the trapezium rule with an adaptive mesh size. This code utilised the Gnu Software Library (GSL), used mainly in the Gaussian surface generation. The evaluation of the Hankel function was calculated in two different regions: for smaller arguments a series method was employed [58],

$$H_n^{(1)}(z) = J_n(z) + iY_n(z), \tag{5.7.1}$$

$$J_n(z) = \left(\tfrac{1}{2}z\right)^n \sum_{k=0}^{\infty} \frac{\left(-\tfrac{1}{4}z^2\right)^k}{k!\,\Gamma(n+k+1)}, \tag{5.7.2}$$

$$\begin{aligned} Y_n(z) = -\frac{\left(\tfrac{1}{2}z\right)^{-n}}{\pi} \sum_{k=0}^{n-1} \frac{(n-k-1)!}{k!} \left(\tfrac{1}{4}z^2\right)^k + \frac{2}{\pi}\ln\left(\tfrac{1}{2}z\right) J_n(z) \\ - \frac{\left(\tfrac{1}{2}z\right)^n}{\pi} \sum_{k=0}^{\infty} \left(\psi(k+1) + \psi(n+k+1)\right) \frac{\left(-\tfrac{1}{4}z^2\right)^k}{k!\,(n+k)!}, \end{aligned} \tag{5.7.3}$$

where J and Y are the first and second Bessel functions, respectively; $H_n^{(1)}$ is the Hankel function of the first order; Γ is the gamma function, ψ is the digamma function [58] and with the summations truncated once a predefined tolerance is reached (6 significant figures was used in the code). For larger arguments an asymptotic form involving the complex exponential functions [58] becomes more practical:

$$H_n^{(1)}(z) \sim \left(\frac{2}{\pi z}\right)^{\frac{1}{2}} \exp\left(i\left(z - \tfrac{1}{2}n\pi - \tfrac{1}{4}\pi\right)\right). \tag{5.7.4}$$

The program was then deployed on the University of Nottingham's high performance computing (HPC) facility, and was set to run over multiple Intel E5472 3.0GHz Harpertown processors.

To illustrate the massive reductions in the computational time that the HPC facility offers, the example of Figure 5.7, occurring later in this chapter, will be used. Each data point in the figure results from $120,000$ surface realisations with each realisation then integrated over a region of 5000 correlation lengths of the Gaussian surface to ensure the accuracy of the electric field. Each curve in Fig 5.7 would require $\sim$3 CPU months of calculation (on a standard desktop PC). This task can be completed in under 15 hours on the HPC facility.

Figure 5.5 shows the spatial intensity, $|E|^2$, formed in the second medium when the interface is a sinusoidal perturbation of half-wavelength amplitude and 10-wavelengths periodicity length - lighter and darker colours representing higher and lower intensities, respectively. In Figure 5.5(a & b), the second medium has refractive index $n_2 = 3 + \kappa i$ (with

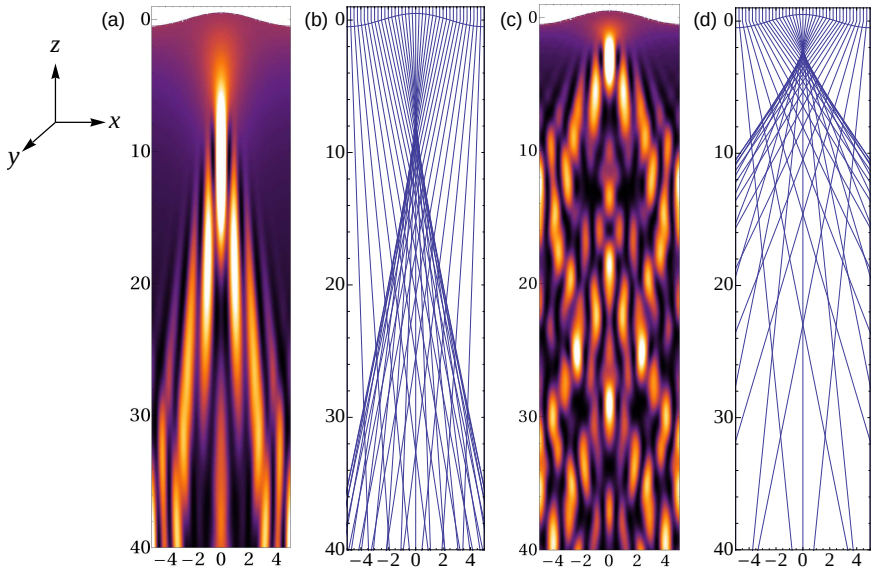

Figure 5.5: Intensity from physical- (a & c) and ray-optics (b & d) of a planar wave traversing at normal incidence to a sinusoidal interface, from air ($n = 1$) into $n = 3$ (a & b) or $n = -1$ (c & d). For clarity, only those rays resulting from one protuberance are drawn in (b) and (d). Lengths are calibrated in units of wavelength.

$\kappa \sim 10^{-5}$, which assists with the convergence of the numerical results). Figure 5.5(a) is the physical-optics solution whereas Fig. 5.5(b) shows the ray density resulting from the geometrical-optics approximation. Note that the location of the principal focus at about 10 wavelengths from the surface is captured by the ray approach, but the physical-optics analysis reveals the region of diffraction fringes beyond the focus. Figure 5.5(c & d) is for when the second medium has $n_2 = -1 + \kappa i$ ($\kappa \sim 10^{-5}$, which is optimistic for current LHM) so that the refractive index contrast between the two media is the same as that for the previous example. Note again the correspondence between the ray and wave representations, but that the principal focus now occurs at around two wavelengths from the interface, that the ray density is greater there, and that the region of diffraction fringes has wider extent that will lead to interference from different parts of the surface at shorter propagation distances. All these qualitative observations are in accord with what was found from Rice theory, and they will now be quantified.

5.8 Distance to the Principal Focus

Figure 5.6 shows the distance from the mid-plane of the interface to the principal focus plotted as a function of the refractive index of the second medium. The different data

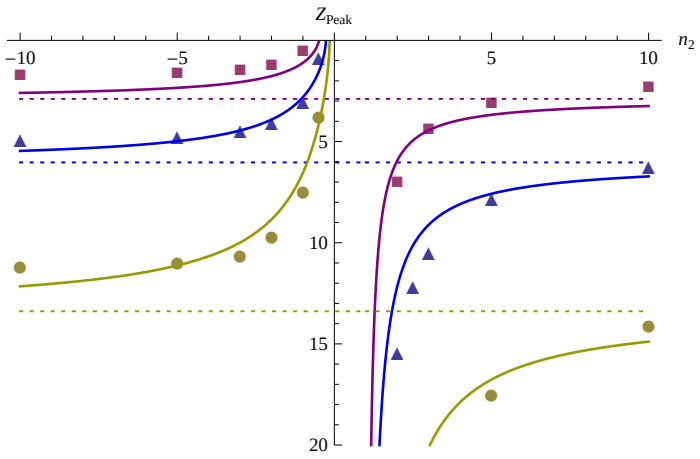

Figure 5.6: Distance from the mean plane of the surface to the point of maximum intensity, when the interface is given by a sinusoid of amplitude $\lambda/4$ (yellow circles), $\lambda/2$ (blue triangles) and λ (purple squares). Also shown by the solid lines are the results from ray optics of the previous chapter, where the parameters involved are chosen by utilising the (known) surface profile and determining an appropriate ray seperation distance, d, whose value is determined from the data to be $\lambda/4$: $d = 2.0$; $\lambda/2$: $d = 1.6$; λ: $d = 1.4$.

points and curves correspond to different amplitudes of the surface, this being a proxy for its roughness. The solid lines are predictions from geometrical-optics, obtained using equation (4.3.5) of chapter 4, whereas data represented by the symbols are derived from the physical-optics solution obtained from (5.2.5). The focus moves towards the interface with increasing positive values of n_2, but attains an asymptote whose value depends on the surface roughness shown by the horizontal dotted lines. This is because with increasing n_2 the direction of a ray becomes progressively more aligned with the local normal to the surface, but does not pass through it. However when $n_2 < 0$ the rays are refracted to the other side of the normal, although having the same asymptote for large $|n_2|$. As $|n_2|$ decreases, the focus moves towards the surface, accessing a region unattainable by any RHM. This is in accord with the findings of the previous chapter, the analytical ray-optics approach encapsulating qualitatively this aspect of the physical optics solution. Having established the location of the principle focus, its strength will now be determined through consideration of ensembles of random interfaces.

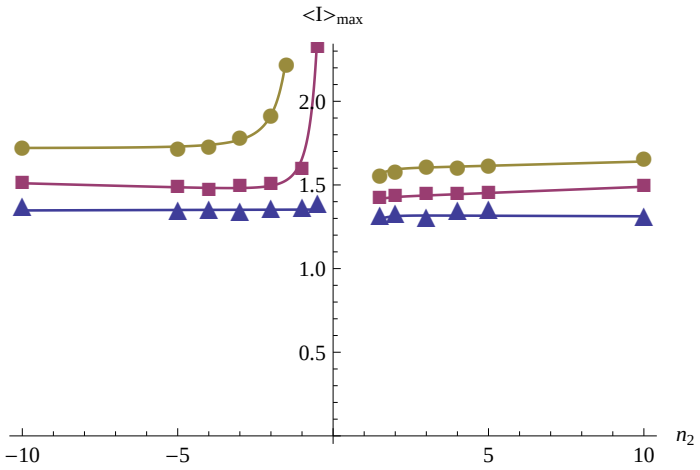

Figure 5.7: Maximum average intensity for a normally incident plane wave passing through a Gaussian rough surface into a medium of n_2. In all curves the correlation length $\ell/\lambda = 10$ and the roughness is given by $\sigma/\lambda = 5.0$ (yellow circles), 2.5 (purple squares) and 1.0 (blue triangles).

5.9 Intensity at the Principal Focus

The ray density at a focus is infinite, but diffraction broadens the caustic to give a finite value for the intensity there. Taking $S(x)$ to be a rough random surface with Gaussian statistics - having zero-mean, variance σ^2 and normalized Gaussian autocorrelation function $\rho(x) = \exp\left(-\frac{1}{2}x^2/\ell^2\right)$ with characteristic fluctuation length ℓ, enables the maximum average intensity $\langle I \rangle_{\max}$ to be calculated from $\sim 10^5$ realizations of the surface. The two dimensionless parameters that characterize the surface roughness in physical-optics are σ/λ and ℓ/λ. In all the results that follow, $\ell/\lambda = 10$ but σ/λ, and consequently the rms surface slope, varies.

The value of $\langle I \rangle_{\max}$ is shown in Figure 5.7 as a function of n_2, the different curves corresponding to different values of random surface roughness. Surfaces with $\sigma/\lambda = 1$, $\sigma/\lambda = 2.5$ and $\sigma/\lambda = 5$ are denoted by blue triangles, purple squares and yellow circles respectively. For positive values of n_2 the average maximum intensity is insensitive to n_2, but increases with increasing surface roughness. This is because, for a given roughness, the location of the focus attains its asymptote, and increasing the refractive index further does not affect the radiant flux at the focal point. Moreover, recall that both media are impedance matched and so the usual increasing reflection from an interface associated with increase in refractive index no longer occurs. This perspective also applies for negative values of n_2 provided the roughness is sufficiently small ($\sigma/\lambda \leq 1$), for then the light contributing to a particular focal point originates from an arc-length of the surface whose extent scales with

$\left(1+\sigma^2/\ell^2\right)$: The average arc-length per unit length being given by

$$\begin{aligned}\frac{\langle\text{Arc-Length}\rangle}{\text{Unit Length}} &= \left\langle\left(1+\left(S'(x)\right)^2\right)^{1/2}\right\rangle = \int_{-\infty}^{\infty}\left(1+S'^2\right)^{1/2}P(S')dS' \\ &= \int_{-\infty}^{\infty}\left(1+S'^2\right)^{1/2}\frac{\ell}{\sigma\,(2\pi)^{1/2}}\exp\left(-\frac{S'^2\ell^2}{2\sigma^2}\right)dS' \\ &= \frac{2^{1/2}\sigma}{\ell}U\left(-\frac{1}{2},\,0,\,\frac{\ell^2}{2\sigma^2}\right),\end{aligned} \tag{5.9.1}$$

such that under the limit σ tending to zero this becomes

$$\frac{\langle\text{Arc-Length}\rangle}{\text{Unit Length}} \sim 1+\frac{2^{1/2}\sigma^2}{\pi^{1/2}\ell^2}+O(\sigma^4) \tag{5.9.2}$$

with U being the Hypergeometric U function [58]. Increasing the roughness further shows that $\langle I\rangle_{\max}$ increases for sufficiently small $|n_2|$ and especially for values appropriate to the perfect lens. The reason for this is twofold. First, the principal focus moves progressively towards the interface with decreasing $|n_2|$ and so the radiant flux increases. Second, the arc-length of a section of surface contributing to the focus now increases as σ/ℓ:

$$\frac{\langle\text{Arc-Length}\rangle}{\text{Unit Length}} = \frac{2^{1/2}\sigma}{\ell}U\left(-\frac{1}{2},\,0,\,\frac{\ell^2}{2\sigma^2}\right) \sim \frac{2^{1/2}\sigma}{\pi^{1/2}\ell}+O\left(\sigma^{-1}\right) \tag{5.9.3}$$

as σ tends to infinity. Hence the diffraction broadened caustics in a LHM are brighter than those in a RHM with the same absolute refractive index and roughness, as indeed can be inferred qualitatively from inspection of Figure 5.5(a & c).

5.10 Intensity Fluctuations

The fluctuations in brightness can be gauged from the normalized second intensity moment $I^{[2]} = \langle I^2\rangle / \langle I\rangle^2$. The numerical calculations have been validated against the analytical (small σ) Rice theory of the section 5.4, which predicts the scintillations at the surface have value 3 - consistent with a *real* Gaussian process that characterizes the surface fluctuations, and declines monotonically with increasing distance from the surface to 2, which is consistent with a *complex* Gaussian process. The field in this latter saturated regime can be interpreted as comprising a superposition of many waves originating from statistically independent sections of the surface. These waves have completely randomised phases and their interference leads to the field being described by a complex Gaussian process giving an intensity speckle pattern [72]. Figure 5.8 shows the second intensity moment as a function

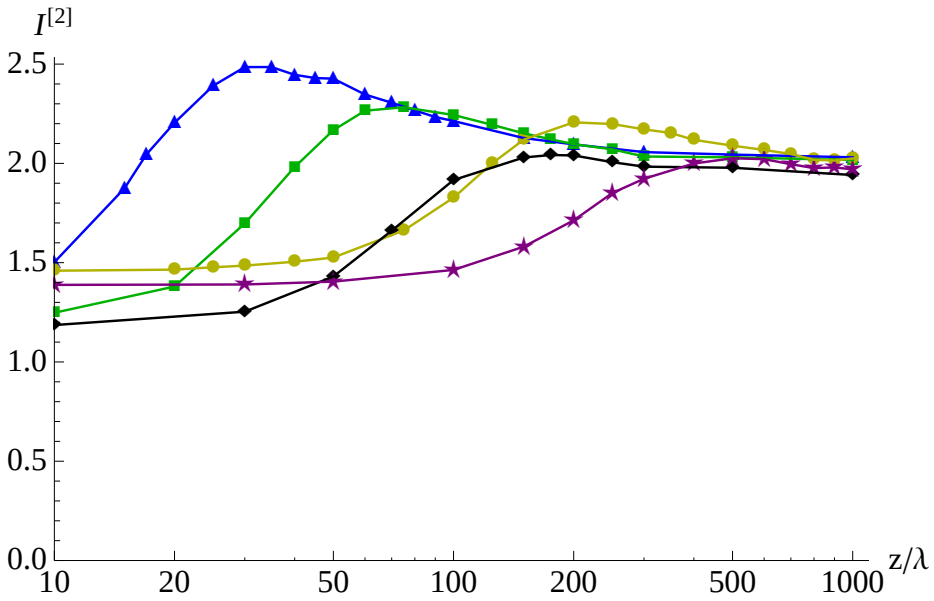

Figure 5.8: Scintillation index as a function of distance for a normally incident plane wave passing through a Gaussian rough surface, of transverse length $\ell/\lambda = 10$ and longitudinal roughness σ/λ, into a medium of n_2. The parameters for the curves given are $\sigma/\lambda = \frac{1}{4}$: $n_2 = -1 + 10^{-5}i$ (black diamonds), $n_2 = 3+10^{-5}i$ (purple stars); $\sigma/\lambda = \frac{1}{2}$: $n_2 = -1+10^{-5}i$ (green squares), $n_2 = 3+10^{-5}i$ (yellow circles); $\sigma/\lambda = 1$: $n_2 = -1 + 10^{-5}i$ (blue triangles).

of normalised distance z/λ into the second medium for different values of σ/λ. For comparison in what follows, scintillations of the order 2.5 are comparable with those observed in light from Sirius scattered by the turbulent atmosphere [73]. The different curves in Figure 5.8 correspond to the refractive index in the second medium being $n_2 = -1 + \kappa i$ (black - $\sigma/\lambda = 1/4$, green - $\sigma/\lambda = 1/2$, blue - $\sigma/\lambda = 1$) or $n_2 = 3 + \kappa i$ (purple - $\sigma/\lambda = 1/4$, yellow - $\sigma/\lambda = 1/2$), thereby comparing media with the same absolute refractive index *change* from air. Contrasting the scintillations of intensity for RHM and LHM with a weakly rough surface with the same value of $\sigma/\lambda = 1/4$ sees, for short propagation distances, the purple curve for the RHM rise uniformly from $\sim$1.4 compared with the equivalent LHM given by the black curve rising from a lower value of ~ 1.2. The trend for the scintillations being greater in the RHM than the LHM for *short* propagation distances is also the case for the rougher surface with $\sigma/\lambda = 1/2$ as can be seen by the complementary pair of yellow and green curves. The reason for this effect is because the phase of a wave changes with propagation distance in proportion to the local refractive index. For the examples shown this is three times greater in the RHM than in the LHM. Consequently wider excursions of the phase will occur in a shorter propagation distance in the RHM than in the LHM with

resultant increase in the variation of intensity. A focussing region is symptomatic of a peak appearing in the scintillation curve [74, 70]. When $\sigma/\lambda = 1/4$, a peak is barely observable in the RHM (purple), but the LHM has a weak peak of size ~ 2.1 centred around 175 wavelengths from the interface. Increasing the roughness to $\sigma/\lambda = 1/2$ causes a focussing peak to occur in both right- (yellow) and left- (green) handed media, but that the maximum value is respectively greater and occurs closer to the interface for the LHM. Beyond the focussing peak all the scintillation curves decline to an asymptotic value ~ 2. Note however that the saturation occurs at smaller propagation distances in the LHM than the RHM. With increasing roughness the trend is for progressively stronger fluctuations before the onset of speckle, as is illustrated by the blue curve which is for a LHM with the same optical parameters as before but with $\sigma/\lambda = 1$. Hence the caustics in a LHM twinkle more and at distances closer to the boundary than those in an equivalent RHM with the same refractive index contrast.

The results of this chapter have analysed an electromagnetic wave passing from $n = +1$ into $n = -1$ through a rough interface of prescribed statistics. Within this second medium the wave causes interference patterns and scintillations are generated by the random surface. An electromagnetic wave passing from $n = -1$ into $n = +1$ through a surface with the same statistics would generate the same scintillation statistics, as the wave undergoes the same negative refraction, c.f. (5.6.1). Finally, the addition of a planar boundary before this rough interface would not affect these statistics. Therefore the results of this section which refer to scintillations within $n = -1$ could equally refer to results deriving from a perfect lens with a planar front interface and a roughened rear interface, illuminated by an electromagnetic wave and with the measurements of the field being carried out in the vacuum beyond the perfect lens (distance in the case being measured from the rear surface). If, in addition, a perfect lens had a roughened front surface this would only contribute to the disruption to the wave by the lens.

5.11 Conclusion

The implications of this chapter for a perfect lens with imperfect boundaries are severe. Even sub-wavelength size undulations in the surface displacement generate caustics close to the interface which then interfere to produce saturated Gaussian speckle within about 200 wavelengths of the boundary. The addition of a second (imperfect) boundary to the lens would further disrupt the coherence of the evanescent modes that are required for the

lens to achieve its super-resolving capability. Consequently, realizing the perfect lens will require as much effort to achieve planar boundaries as presently attends reducing losses in the bulk.

Chapter 6

Summary and Conclusions

6.1 Overview

The overall aim of this thesis was to determine the response of LHM, and specifically the perfect lens configuration, to imperfect boundaries. This was done in the first instance though an analytical graded-index (GRIN) model and secondly through consideration of true realisations of a roughened interface between RHM and LHM, studied through ray- and physical-optics approaches. Many important implications for negative refraction and perfect lensing have been determined, the most pertinent of these are highlighted alongside future avenues of research.

6.2 Between Right- and Left-Handed Media

Chapter 2 investigated a LHM half-space with a roughened interface, modelled by a graded index boundary. The Chapter presented the analytical calculations for the propagation of electromagnetic radiation through this inhomogeneous layer. Significant field localization was generated in the layer that is caused by the coherent superposition of evanescent waves. The strength of the field localization and the transmission properties of the layer was investigated as a function of the layer width, losses and defects in the refractive index profile; the former two modelled by continuous changes, and the latter by discontinuous changes, in the index profile. In all cases within this chapter the reflected and transmitted wave properties were determined analytically.

6.3 Perfect lens with not so perfect boundaries

Chapter 3 developed the work of Chapter 2 by introducing a second interface to the LHM half-space, creating a perfect lens configuration which allowed for the investigation of evanescent mode propagation through a perfect lens with roughened boundaries modelled again by GRIN layers. A transitional layer on the boundary closest to the image was shown to have a greater detrimental effect on the resolving ability of the lens as compared to a similarly sized layer placed on the boundary closest to the source. However, the field localisations at the boundaries were not independent of each other and their effect combined to affect the resolving capability of the lens - which was quantified in terms of the layer thickness. If the LHM was lossless, then the layers had no effect on the lens' ability to resolve perfectly. This is *not* the case if the LHM was lossy; the consequence of the localization caused by the layers is to preferentially dissipate high wavenumber modes. Specifically the layers produced an effect that is qualitatively similar to a lens with nonlinearly increased losses.

The solution presented within Chapter 3 contained the polarization-state of the wave and as such the approach can be used to investigate, for example, the emission polarization effects of infra-red radiation, e.g. [75], from left-handed media.

6.4 Negative refraction and rough surfaces: A new regime for lensing

Chapter 4 investigates negative refraction through a roughened interface but instead of applying approximations to the boundary, the infinite k limit of ray-optics was used to derive results from rays passing into a LHM half-space through a roughened interface, prescribed by Gaussian statistics. Rays can focus at a smaller distance from the interface due to the negative refractive effects, this being especially pronounced if $|n| < 1$. Moreover, non-Fresnel reflection can occur if $n < 1$, principally through multiply refracted paths of the rays. This is an effect distinct from the familiar total internal reflection caused by the interaction of light from an optically denser medium with a less dense one, principally because of the negative refraction caused by LHM. Consequently an *impedance matched* configuration involving a LHM (such as the perfect lens) with a roughened interface can still display reflection. Distinct reflection signatures are produced depending on whether the ray paths pass through the second medium or air before leaving the vicinity of the interface. Insofar as transmission into the second medium is concerned, increasing the rms

surface slope erodes the negative refraction effect. The refracted ray behaves increasingly as if it is in a RHM with increasing rms surface slope.

To extend the work of the Chapter it would be interesting to investigate rougher, non-Gaussian, surfaces - for example those with sub-fractal slopes, where the production of caustics is prevented or impeded for RHM.

6.5 Enhanced twinkling within the perfect lens

Chapter 5 extended the work of Chapter 4 by relaxing the infinite k limit to probe the effects of phase and diffraction within LHM. This required formulating the Huygens' principle appropriate for magnetic media. Calculations were done in the first instances through the small σ/λ limit of Rice theory which showed that a rough boundary on a LHM (when compared to its RHM counterpart) causes greater scintillations and that the scattered field converges to Gaussian noise over shorter optical depths. When the surface is a Gaussian process, the scattered field was shown to evolve from a real Gaussian process near the surface into a complex Gaussian process as distance into the second media increases resulting in a classical speckle pattern.

The second approach of this chapter was to utilise large-scale Monte-Carlo simulations of the Huygens' integral to determine the intensity statistics within the second media for larger surface roughnesses than can be treated by Rice theory. These simulations verified the ray-optics result that illuminating a roughened interface between air and a LHM produces a regime for enhanced focussing of light close to the boundary. However the new physics that results is that this generates caustics that are brighter, fluctuate more, and cause Gaussian speckle to occur at distances closer to the interface than in right-handed matter. The addition of a second (imperfect) boundary to create a perfect lens configuration would further disrupt the imaging ability of the lens.

Nevertheless, the ability to achieve a focus very close to the interface could be turned to advantage for applications in near-field microscopy [76]. Moreover, the production of fully developed speckle in short propagation distances can have ramifications for optical signal processing applications.

6.6 Further Work

The natural extension of this work is to consider the perfect lens configuration with roughened boundaries through physical optics. In its full form this is, computationally, highly-problematic as the full three dimensional electric-field must be constructed for each reflection from an interface. Given that evanescent amplification within a perfect lens is due to the *infinite* summation of reflections, it is reasonable to assume that an extremely large number of reflections must be evaluated numerically to encapsulate the evanescent components of the field. To calculate the field for one realisation of the rough surface would prove to be orders of magnitude more complicated then the calculations performed in chapter 5. To obtain meaningful averages for quantities such as the scintillation index requires millions of realisations and would be beyond the current computing capabilities of even the high-performance computing facility.

One possible method for progression in this area is to investigate a perfect lens configuration with a planar front boundary and a weakly roughened second boundary. Given the closeness of this problem to a perfect lens with planar boundaries, it is reasonable to assume that the electric field produced will be a perturbation of the perfect case. French *et al* give the electric field throughout the perfect lens when the material properties deviate from $\epsilon = \mu = -1$ [54], which can then be used as the first approximation to the field within the layer thereby dramatically reducing the number of reflections needing to be considered. Whilst this procedure would be on the limit of the current computational ability it would give important information about the nature and spatial extent of the image generated by a perfect lens with roughened boundaries and including the effects on the evanescent components that are vital for super-resolution.

6.7 Conclusions

In summary this thesis has investigated the interactions of negative refraction, perfect lensing and roughened interfaces through a variety of techniques. In every situation the outlook for 'perfect' imaging is bleak, with any surface aberrations deteriorating the LHM performance. When a graded-index approximation to the surface is valid, then localisations are generated that lead to greatly reduced transmission into lossy LHM; when the high k limit of ray-optics is valid then backscatter effects diminish transmission even if the medium is, materially speaking, perfect; and even when these limits do not apply - negative refraction

serves to amplify any surface perturbations that are present, leading to interactions, and therefore generation of Gaussian noise, considerably closer to the surface. Whilst large dissipation currently masks the influence of surface aberrations, they form a profound and lurking danger - lying in wait until such a time when losses are reduced, whereupon their full disruptive effect will be realised.

Appendix A

Analytical Solutions to the magnetic GRIN model

Equation (2.2.5) has few analytical solutions in terms of tabulated special functions and all come from different substitutions for the independent variable in the differential equation. The following is a table of all profiles for which analytical solutions have been found to exist:

μ	ϵ	Substitution	Resulting Equation	
e^{mz}	$\eta\mu + A$	$\frac{du}{dz} = \mu$	$\frac{d^2E}{du^2} + \left(\frac{\omega^2\eta}{c^2} + \frac{A}{mu} - \frac{k_x^2}{m^2u^2}\right)E = 0$	(A1)
$mz + d$	$\eta\mu$	$\Lambda = \mu^2$	$\frac{d^2E}{d\Lambda^2} + \frac{1}{(2m)^2}\left(\frac{\omega^2\eta}{c^2} - \frac{k_x^2}{\Lambda}\right)E = 0$	(A2)
$m(z+d)^{-\frac{1}{3}}$	$\eta\mu$	$\frac{d\zeta}{dz} = \mu$	$\frac{d^2E}{d\zeta^2} + \left(\frac{\omega^2\eta}{c^2} - \frac{3k_x^2\zeta}{2m^3}\right)E = 0$	(A3)
$m(z+d)^{-\frac{1}{2}}$	$\eta\mu$	$\frac{d\psi}{dz} = \mu$	$\frac{d^2E}{d\psi^2} + \left(\frac{\omega^2\eta}{c^2} - \frac{k_x^2\psi^2}{4m^4}\right)E = 0$	(A4)

A.1 Exponential Profile: $\mu = e^{mz}$, $\epsilon = \eta\mu + A$

The solution is

$$E(z) = \left(\frac{\mathcal{Z}(z)\,c}{i\,\eta^{1/2}\,\omega}\right)^{\frac{\chi}{2}} \exp\left(-\mathcal{Z}(z)\right)\left(\alpha F(z) + \beta G(z)\right) \tag{A.1.1}$$

where α and β are constants of integration and

$$F(z) = \mathrm{U}\left(\frac{\chi + \frac{i\,A\,c}{m\,\eta^{1/2}\,\omega}}{2}, \chi, 2\,\mathcal{Z}(z)\right),$$

$$G(z) = \mathrm{L}\left(\frac{-\chi - \frac{i\,A\,c}{m\,\eta^{1/2}\,\omega}}{2}, \chi - 1, 2\,\mathcal{Z}(z)\right),$$

$$\chi = 1 + \left(1 + \frac{4\,k_x^2}{m^2}\right)^{1/2}, \quad \mathcal{Z}(z) = \frac{i\exp(m\,z)\eta^{1/2}\omega}{c\,m},$$

U is the confluent hypergeometic function of the second kind and L are the generalized Laguerre polynomials [58]. In the special case of $A = 0$ the functions reduce to the Bessel

functions of first and second kind.

A.2 Linear Profile: $\mu = m\,z + d,\ \epsilon = \eta\mu$

The solution is

$$E(z) = \frac{\exp\left(\frac{-i\,\gamma\,\Psi(z)}{2}\right)\Psi(z)}{4\,c^2\,m^2}\left(\alpha F(z) + \beta G(z)\right) \tag{A.2.1}$$

where α and β are again constants of integration,

$$F(z) = \mathrm{M}\left(1 - \frac{ik_x^2}{4\,m^2\,\gamma}, 2, i\,\gamma\,\Psi(z)\right),$$

$$G(z) = \mathrm{U}\left(1 - \frac{ik_x^2}{4\,m^2\,\gamma}, 2, i\,\gamma\,\Psi(z)\right),$$

$$\gamma = \frac{\eta^{1/2}\,\omega}{c\,m}, \quad \Psi(z) = (d + m\,z)^2$$

and M and U are the confluent hypergeometric functions of the first and second kind, respectively [58]. This is the solution that is analysed in chapter 2.

A.3 Algebraic Profiles: $\mu = (m\,z + d)^{-\frac{1}{3}},\ \epsilon = \eta\mu$

The solution is

$$E(z) = \alpha F(z) + \beta G(z)$$

where

$$F(z) = \mathrm{Ai}\left(\left(\frac{3}{2\,k_x^2}\right)^{\frac{2}{3}}\left(k_x^2\,(d+z)^{\frac{2}{3}} - \frac{\eta\,\omega^2\,m^2}{c^2}\right)\right),$$

$$G(z) = \mathrm{Bi}\left(\left(\frac{3}{2\,k_x^2}\right)^{\frac{2}{3}}\left(k_x^2\,(d+z)^{\frac{2}{3}} - \frac{\eta\,\omega^2\,m^2}{c^2}\right)\right),$$

and Ai and Bi are the first and second Airy functions [58].

A.4 Algebraic Profiles: $\mu = (m\,z + d)^{-\frac{1}{2}},\ \epsilon = \eta\mu$

The solution is

$$E(z) = e^{-k_x\,(d+z)}\left(\alpha\,F(z) + \beta\,G(z)\right)$$

where

$$F(z) = \mathrm{H}\left(-\frac{1}{2} + \frac{m^2\,\eta\,\omega^2}{c^2\,k_x}, (2\,k_x\,(d+z))^{1/2}\right),$$

$$G(z) = \mathrm{M}\left(\frac{1}{4} - \frac{m^2\,\eta\,\omega^2}{2\,c^2\,k_x}, \frac{1}{2}, 2\,k_x\,(d+z)\right),$$

H are the Hermite polynomials and M is the confluent hypergeomtric function of the first kind [58].

Of all these different results only the exponential and straight line profiles can traverse from a doubly positive to a doubly negative media, or vise-versa. However, to do this with the exponential profile necessarily involves having a complex m inevitably introducing, largely uncontrollable, losses. Therefore the straight line profile represents the most versatile GRIN model and consequently this was the model adopted for the development of chapters 2 and 3.

Appendix B

Calculation of the Green's function in 2D

B.1 Two-dimensional Green's function for the Helmholtz equation

We wish to determine the Green's function for the Helmholtz equation:

$$\nabla^2\psi + k^2\,\psi = 0 \tag{B.1.1}$$

in circular symmetry. The 2D Lapacian is then given by

$$\nabla^2\psi(r) = \frac{1}{r}\frac{d}{dr}\left(r\frac{d\,\psi}{dr}\right), \tag{B.1.2}$$

therefore the Green's equation in this situation is a solution of

$$\frac{1}{r}\frac{d}{dr}\left(r\frac{d\psi}{dr}\right) + k^2\,\psi = \delta(r). \tag{B.1.3}$$

Equation (B.1.3) is Bessel's equation with solutions

$$\psi = A\,J_0(k\,r) + B\,Y_0(k\,r)\,, \tag{B.1.4}$$

with $B \neq 0$ to satisfy the δ discontinuity at the origin. Choosing $A = 1$, $B = i$ gives

$$\psi = H_0^1(k\,r) \tag{B.1.5}$$

where H_0^1 is the first Hankel function of zeroth order.

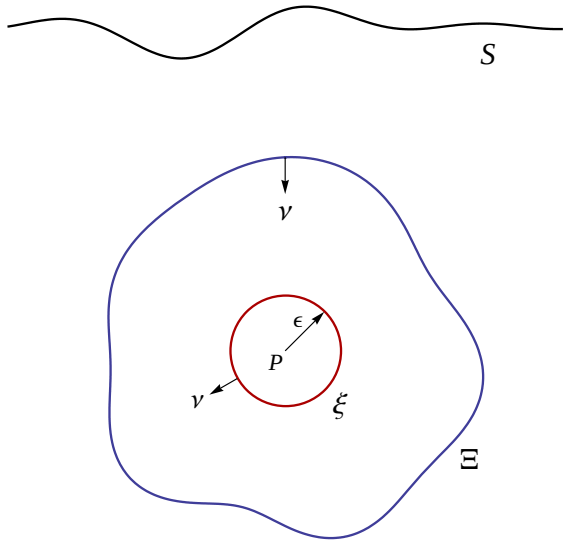

Figure B.1: An illustration of the outer integral, Ξ; the inner integral, ξ - radius ϵ; the inward normal ν and the observation point, P. Also shown is the interface between media S.

B.2 Calculation of the electric field within a given surface

Through the first and second Green's identities, the Helmholtz equation becomes the following equality, [77],

$$\oint_{\Xi} \left(E \frac{\partial \psi}{\partial \nu} - \psi \frac{\partial E}{\partial \nu} \right) d\Xi = - \oint_{\xi} \left(E \frac{\partial \psi}{\partial \nu} - \psi \frac{\partial E}{\partial \nu} \right) d\xi \tag{B.2.1}$$

where, as shown in Fig. B.1, Ξ is the outer surface encompassing ξ; ξ is a circle of radius ϵ, centred on the point of interest, P, and ψ is the Green's function (B.1.5). In the latter integral the normal, ν, is in the radial direction so that the second integral can be written

$$\oint_{\xi} \left(\psi \frac{\partial E}{\partial r} - E \frac{\partial \psi}{\partial r} \right) d\xi. \tag{B.2.2}$$

Letting $\epsilon \to 0$ then (B.2.2) becomes

$$\oint_{\xi} H_0^1(k\,\epsilon) \frac{\partial E}{\partial r} - E \left(-k\, H_1^1(k\,\epsilon) \right) d\xi \tag{B.2.3}$$

$$= \int_0^{2\pi} \left(H_0^1(k\,\epsilon) \frac{\partial E}{\partial r} + E \left(k\, H_1^1(k\,\epsilon) \right) \right) \epsilon \, d\theta. \tag{B.2.4}$$

where the surface element $d\xi$ has been replaced by $\epsilon\, d\theta$ given the circular nature of the surface ξ. As $H_0^1(k\,\epsilon) \ll H_1^1(k\,\epsilon)$ as $\epsilon \to 0$ [58] this then gives the limit of (B.2.2) as

$$\int_0^{2\pi} E \left(k\, H_1^1(k\,\epsilon) \right) \epsilon \, d\theta, \tag{B.2.5}$$

now

$$\epsilon\, H_1^1(k\,\epsilon) \to -\frac{2i}{k\pi} \text{ as } \epsilon \to 0, \tag{B.2.6}$$

so that

$$\int_0^{2\pi} E\left(k\, H_1^1(k\,\epsilon)\right) \epsilon\, d\theta \to 2\pi \left(k\left(-\frac{2i}{k\pi}\right)\right) E(P) = -4\, i\, E(P) \tag{B.2.7}$$

as $\epsilon \to 0$. Therefore the electric field (at a point within the surface Ξ) can be given by

$$E(P) = \frac{-1}{4\, i} \oint_{\Xi} \left(E\frac{\partial \psi}{\partial \nu} - \psi \frac{\partial E}{\partial \nu}\right) d\Xi. \tag{B.2.8}$$

The final step involves expanding Ξ until one half of the boundary becomes the surface S forming the interface between the media, and the second half moves out to infinity. The Sommerfeld radiation conditions [77] then give the requirements for this second half of the integral to be neglected, valid in most situations when dealing with lossy right-handed media. However, in the case of LHM it is possible to have evanescent modes that appear to grow away from the primary boundary - but only if there is a second interface to set-up the resonant effect [2]. For the purposes of this thesis the case of a LHM half-space will be considered, which encapsulates the negative refraction and phase effects of the propagating modes from a source but does not support evanescent amplification in accord with the Sommerfeld radiation conditions. As such, any focus within the LHM will be diffraction limited. It is left to future work to include these evanescent components of the field, pertinent to the study of a roughened perfect-lens.

Appendix C

Derivation of the Scintillation Index for the Rice Approximation

C.1 The average scattered intensity, $\langle I_S \rangle$

Equation (5.4.9) gives the electric field at a point in space. It is of the form

$$E_S(\mathbf{x}') = \int \left(S(x)A(x,\mathbf{x}') + S'(x)B(x,\mathbf{x}') \right) \, dx \tag{C.1.1}$$

with A and B given in (5.4.9):

$$A(x,\mathbf{x}') = \left(- \left. \frac{d\left(\nabla\psi \cdot \mathbf{e}_z\right)}{dS} \right|_{S(x)=0} + ik \left(\nabla\psi \cdot \mathbf{e}_z\right)|_{S(x)=0} - ik\frac{n_2}{n_1} \left. \frac{d\psi}{dS} \right|_{S(x)=0} - k^2 \frac{n_2}{n_1} \, \psi|_{S(x)=0} \right) \tag{C.1.2}$$

and

$$B(x,\mathbf{x}') = \left(\nabla\psi \cdot \mathbf{e}_x\right)|_{S(x)=0} \, , \tag{C.1.3}$$

with the quantities as defined in chapter 5. With this notation

$$\begin{aligned} &\langle I_S \rangle = \langle E_S E_S^* \rangle \\ &= \left\langle \iint \left(S(x_1)A(x_1,\mathbf{x}') + S'(x_1)B(x_1,\mathbf{x}') \right) \left(S(x_2)A(x_2,\mathbf{x}') + S(x_2)B(x_2,\mathbf{x}') \right)^* \, dx_1 \, dx_2 \right\rangle \end{aligned} \tag{C.1.4}$$

which on taking the average inside the integral gives

$$\begin{aligned} \langle I_S \rangle = \iint \big(&\langle S(x_1)S(x_2) \rangle \, A(x_1)A^*(x_2) + \left\langle S(x_1)S'(x_2) \right\rangle A(x_1)B^*(x_2) \\ &+ \left\langle S'(x_1)S(x_2) \right\rangle B(x_1)A^*(x_2) + \left\langle S'(x_1)S'(x_2) \right\rangle B(x_1)B^*(x_2) \big) \, dx_1 \, dx_2 \end{aligned} \tag{C.1.5}$$

where $A(x_i) \equiv A(x_i, \mathbf{x}')$ and $B(x_i) \equiv B(x_i, \mathbf{x}')$ for any x_i. Here it is useful to note that for a Gaussian process, $V(t)$, [70]:

$$\langle V(t)V(t+\tau)\rangle = \sigma^2 g(\tau), \tag{C.1.6a}$$

$$\langle V(t)V'(t+\tau)\rangle = \sigma^2 g^{(1)}(\tau), \tag{C.1.6b}$$

$$\langle V'(t)V(t+\tau)\rangle = -\sigma^2 g^{(1)}(\tau), \tag{C.1.6c}$$

$$\langle V'(t)V'(t+\tau)\rangle = -\sigma^2 g^{(2)}(\tau), \tag{C.1.6d}$$

where the superscript on g and the primes on V denote differentiation with respect to the argument of the function, g is the auto-correlation function of the process and σ the standard deviation of the process. Utilising this and introducing the notation to represent integrals of the form

$$\mathrm{G}(i, X, Y) := \sigma^2 \iint_{-\infty}^{\infty} g^{(i)}(x_2 - x_1) X(x_1) Y(x_2)\, dx_1\, dx_2, \tag{C.1.7}$$

again where the superscript on the auto-correlation function denotes the differention order, then the average intensity, (C.1.4), can be written as

$$\langle I_S\rangle = \mathrm{G}(0, A, A^*) + \mathrm{G}(1, A, B^*) - \mathrm{G}(1, B, A^*) - \mathrm{G}(2, B, B^*)\,. \tag{C.1.8}$$

This appendix makes extensive use of the notation (C.1.7), it is therefore prudent to study this integral further before progressing as there are several properties which lead to significant simplifications. The first feature is that a first order G acting on one A function and one B function is zero, e.g. that $\mathrm{G}(1, A, B) = 0$, and this is shown in section C.2. The second feature, which is detailed in section C.3, is that the complex conjugation of a G function is equivalent to the conjugation of its arguments, i.e. that $(\mathrm{G}(i, X, Y))^* = \mathrm{G}(i, X^*, Y^*)$.

C.2 The Function $\mathbf{G}(1, A, B)$

The first simplification property to be proved is that a first order G acting on one A and one B, irrespective of order and complex conjugation, is zero, e.g. $\mathrm{G}(1, A, B) = 0$. Below the case $\mathrm{G}(1, A, B)$ is examined, but analogous arguments extend this to different permutations and complex conjugations. When fully expanded in terms of their x dependence, equations (C.1.2) and (C.1.3) show that A is an even function and B an odd function in x:

$$A(x) = F(x^2) \tag{C.2.1a}$$

$$B(x) = x\, H(x^2) \tag{C.2.1b}$$

for some F and H. Now and throughout this appendix we will adopt the Gaussian autocorrelation function of the form [70]

$$g(\tau) = \exp\left(-\frac{\tau^2}{2\,\ell^2}\right), \tag{C.2.2}$$

where ℓ is the transverse correlation length. With this correlation function the first derivative is clearly

$$g^{(1)}(\tau) = -\frac{\tau}{\ell^2}\exp\left(-\frac{\tau^2}{2\,\ell^2}\right). \tag{C.2.3}$$

To prove that a first order G acting on A and B is zero the coordinate transformation $u = x_2$, $v = x_1x_2$ will be used to evaluate the integral. The proof comes in two parts: firstly the integrand is transformed revealing a hidden symmetry, then the change in the limits of integration are examined.

Transformation of the integrand

Using the notation of (C.2.1) the x_1 and x_2 dependence of the integrand appearing in $\mathrm{G}(1, A, B)$ can be written as

$$Q(x_1,\, x_2) = x_2\,(x_2 - x_1)\,F(x_1^2)\,H(x_2^2)\,\exp\left(\frac{-(x_2 - x_1)^2}{2\,\ell^2}\right), \tag{C.2.4}$$

and with the coordinate transformation

$$u = x_2, \quad v = x_1x_2 \tag{C.2.5}$$

the integrand can be written as a new function, W, defined by

$$u^{-1}\,W(u^2,\, v) = u^{-1}\,(u^2 - v)\,F\left(\frac{v^2}{u^2}\right)\,H(u^2)\,\exp\left(-\frac{v^2}{2\,u^2\,\ell^2}\right)\,\exp\left(-\frac{u^2}{2\,\ell^2}\right)\,\exp\left(\frac{v}{\ell^2}\right), \tag{C.2.6}$$

where the factor u^{-1} is derived from the Jacobian of the transformation. It is clear from (C.2.6) that the integrand is odd in u, it is this feature that will be exploited in the next section.

Change of limits

The coordinate transformation (C.2.5) reveals a hidden symmetry of $\mathrm{G}(1, A, B)$, but the symmetry must be linked with the change of limits associated with the coordinate transformation. Firstly the integrand will be integrated over a square domain of width $2a$. Then the limit as a tending to infinity will be used to obtain the integral found in (C.1.7). Fig.

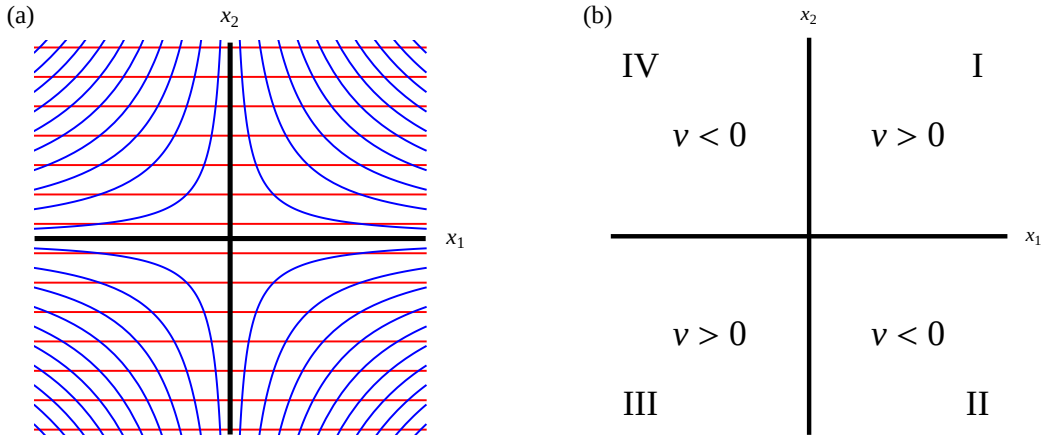

Figure C.1: (a) Lines of constant u (horizontal red lines) and v (cartesian hyperbola shown in blue), (b) the sign of v in the four quadrants of the integration, indicated by the roman numerals.

C.1 shows lines of constant u and v and the sign of v in each of the four quadrants. Treating each quadrant separately gives the change of limits as:

$$\text{Region I:} \quad \int_0^a \int_0^a Q(x_1, x_2)\, dx_1\, dx_2 = \int_{v=0}^{a^2} \int_{u=v/a}^{a} u^{-1}\, W\big(u^2, v\big)\, du\, dv, \tag{C.2.7a}$$

$$\text{Region II:} \quad \int_0^a \int_{-a}^0 Q(x_1, x_2)\, dx_1\, dx_2 = \int_{v=-a^2}^{0} \int_{u=-a}^{-v/a} u^{-1}\, W\big(u^2, v\big)\, du\, dv, \tag{C.2.7b}$$

$$\text{Region III:} \quad \int_{-a}^0 \int_{-a}^0 Q(x_1, x_2)\, dx_1\, dx_2 = \int_{v=0}^{a^2} \int_{u=-a}^{-v/a} u^{-1}\, W\big(u^2, v\big)\, du\, dv, \tag{C.2.7c}$$

$$\text{Region IV:} \quad \int_{-a}^0 \int_0^a Q(x_1, x_2)\, dx_1\, dx_2 = \int_{v=-a^2}^{0} \int_{u=v/a}^{a} u^{-1}\, W\big(u^2, v\big)\, du\, dv. \tag{C.2.7d}$$

Hence the integral over the whole square is

$$\int_{-a}^a \int_{-a}^a Q(x_1, x_2)\, dx_1\, dx_2 = \int_{-a^2}^{a^2} \left(\int_{-a}^{-v/a} u^{-1}\, W\big(u^2, v\big)\, du + \int_{v/a}^{a} u^{-1}\, W\big(u^2, v\big)\, du \right) dv. \tag{C.2.8}$$

Since the integrand is odd in u then

$$\int_{v/a}^{a} u^{-1}\, W\big(u^2, v\big)\, du = -\int_{-a}^{-v/a} u^{-1}\, W\big(u^2, v\big)\, du, \tag{C.2.9}$$

and therefore

$$\iint_{-a}^{a} Q(x_1, x_2)\, dx_1\, dx_2 = \int_{-a^2}^{a^2} 0\, dv = 0. \tag{C.2.10}$$

Finally taking the limit as $a \to \infty$ in (C.2.10) gives the required result that $\mathrm{G}(1, A, B) = 0$. Analogous arguments extend this to different permutations and complex conjugations, e.g. $\mathrm{G}(1, B^*, A) = 0$.

C.3 Commutative Conjugation

The second feature of $\mathrm{G}(i, X, Y)$ stems from the fact that $g^i(\tau)$ is always real (c.f. (C.2.2)):

$$\begin{aligned} \mathrm{G}(i, X^*, Y^*) &= \sigma^2 \iint g^i(x_2 - x_1) X^*(x_1) Y^*(x_2)\, dx_1\, dx_2 \\ &= \left(\sigma^2 \iint g^i(x_2 - x_1) X(x_1) Y(x_2)\, dx_1\, dx_2\right)^* \\ &= (\mathrm{G}(i, X, Y))^* = \mathrm{G}^*(i, X, Y)\,. \end{aligned} \tag{C.3.1}$$

Together the results of the last two sections will greatly aid in the calculation of the second intensity moment, $\left\langle I_S^2 \right\rangle$, which is presented in the next section.

C.4 The average squared scattered intensity, $\left\langle I_S^2 \right\rangle$

The quantity $\left\langle I_S^2 \right\rangle = \langle E_S E_S^* E_S E_S^* \rangle$, can be written as a four-fold integral over the various permutations of A, A^*, B and B^* acting on four independent variables. Taking the average and utilizing the fact that the fourth-order moment of a real Gaussian random variable can be expressed in terms of products of the second order moments [71]:

$$\frac{\langle V(x_1)V(x_2)V(x_3)V(x_4)\rangle}{\sigma^4} = g(x_2-x_1)g(x_4-x_3)+g(x_3-x_1)g(x_4-x_2)+g(x_4-x_1)g(x_3-x_2) \tag{C.4.1}$$

enables $\left\langle I_S^2 \right\rangle$ to be expanded in terms of G functions defined by (C.1.7), resulting in a 48 term equation with each term itself deriving from the product of two G functions. It is then a trivial but tedious matter to show that two thirds of the terms in $\left\langle I_S^2 \right\rangle$ equate to twice $\langle I_S \rangle^2$, given by

$$\langle I_S \rangle^2 = \mathrm{G}^2(0, A, A^*) - 2\,\mathrm{G}(0, A, A^*)\,\mathrm{G}(2, B, B^*) + \mathrm{G}^2(2, B, B^*)\,, \tag{C.4.2}$$

utilising the features of sections C.2 and C.3 to simplify the results given. Finally, again using the simplifications of sections C.2 and C.3, $\left\langle I_S^2 \right\rangle$ adopts the comparatively simple form

$$\left\langle I_S^2 \right\rangle - 2\,\langle I_S \rangle^2 = |\mathrm{G}(0, A, A)|^2 - 2\,\Re e(\mathrm{G}(2, B, B)\,\mathrm{G}^*(0, A, A)) + |\mathrm{G}(2, B, B)|^2 \tag{C.4.3}$$

or in the form of the second intensity moment:

$$\frac{\left\langle I_S^2 \right\rangle}{\langle I_S \rangle^2} = 2 + \frac{|\mathrm{G}(0, A, A)|^2 - 2\,\Re e(\mathrm{G}(2, B, B)\,\mathrm{G}^*(0, A, A)) + |\mathrm{G}(2, B, B)|^2}{\left(\mathrm{G}(0, A, A^*) - \mathrm{G}(2, B, B^*)\right)^2} \tag{C.4.4}$$

where $\langle I_S \rangle$ has also been simplified to

$$\langle I_S \rangle = \mathrm{G}(0, A, A^*) - \mathrm{G}(2, B, B^*)\,. \tag{C.4.5}$$

C.5 The Second Moment of the Total Intensity, $\langle I^2 \rangle$

It is beneficial to be able to contrast the statistics of the total field with the scattered field, since it is the physically measured quantity. In deriving the scattered electric field (5.4.9) the coherent field (5.4.5) was deducted. The total field is just an additional term in the integrand of the electric field, which will symbolically be denoted $C(x)$:

$$E = \int \big(S(x)A(x) + S'(x)B(x) + C(x)\big)\; dx \tag{C.5.1}$$

where $C(x)$ is given by the integrand of (5.4.5). We can now derive the average total intensity, $\langle I \rangle$, and its second moment, $\langle I^2 \rangle$. Firstly the average total intensity:

$$\begin{aligned}\langle I \rangle = \iint \big(&\langle S(x_1)S(x_2)\rangle\, A(x_1)A^*(x_2) + \langle S(x_1)S'(x_2)\rangle\, A(x_1)B^*(x_2) \\ &+ \langle S'(x_1)S(x_2)\rangle\, B(x_1)A^*(x_2) + \langle S'(x_1)S'(x_2)\rangle\, B(x_1)B^*(x_2) \\ &+ \langle S(x_2)\rangle\, C(x_1)A^*(x_2) + \langle S'(x_2)\rangle\, C(x_1)B^*(x_2) + \langle S(x_1)\rangle\, A(x_1)C^*(x_2) \\ &+ \langle S'(x_1)\rangle\, B(x_1)C^*(x_2) + C(x_1)C^*(x_2)\big)\; dx_1\, dx_2.\end{aligned} \tag{C.5.2}$$

However S is a zero mean Gaussian process, and therefore so is its derivative, S', [70] so that $\langle S \rangle = \langle S' \rangle = 0$ and the average intensity becomes

$$\langle I \rangle = \langle I_S \rangle + \iint C(x_1)C^*(x_2)\, dx_1\, dx_2 = \langle I_S \rangle + \left| \int C(x)\, dx \right|^2 = \langle I_S \rangle + I_C \tag{C.5.3}$$

where I_C is the intensity at the observation point for the case where the interface is a smooth planar boundary.

For the case of the average squared intensity, $\langle I^2 \rangle$, another notational short-hand will be utilised:

$$M(F_1, F_2, F_3, F_4) := \left\langle \iiiint F_1(x_1)F_2^*(x_2)F_3(x_3)F_4^*(x_4)\, dx_1\, dx_2\, dx_3\, dx_4 \right\rangle. \tag{C.5.4}$$

If there is any quantity which averages over an odd number of S and S''s, then that quantity does not contribute [70] (S and S' both being stationary zero-mean Gaussian processes), e.g. $\langle S(x_1)S'(x_2)S(x_3)\rangle = 0$. Utilising this, in conjuncture with the other simplifications of

this Appendix, then the average squared intensity can be given by:

$$\begin{aligned}\langle I^2 \rangle = \langle I_S^2 \rangle \;&+\; M(SA,SA,C,C) + M(SA,S'B,C,C) + M(S'B,SA,C,C) \\ &+\; M(S'B,S'B,C,C) + M(SA,C,SA,C) + M(SA,C,S'B,C) \\ &+\; M(S'B,C,SA,C) + M(S'B,C,S'B,C) + M(SA,C,C,SA) \\ &+\; M(SA,C,C,S'B) + M(S'B,C,C,SA) + M(S'B,C,C,S'B) \\ &+\; M(C,SA,SA,C) + M(C,SA,S'B,C) + M(C,S'B,SA,C) \\ &+\; M(C,S'B,S'B,C) + M(C,SA,C,SA) + M(C,SA,C,S'B) \\ &+\; M(C,S'B,C,SA) + M(C,S'B,C,S'B) + M(C,C,SA,SA) \\ &+\; M(C,C,SA,S'B) + M(C,C,S'B,SA) + M(C,C,S'B,S'B) \\ &+\; M(C,C,C,C)\,.\end{aligned} \tag{C.5.5}$$

Moreover all terms involving combinations of a single A and a single B are zero by the argument in section C.2 - the C components in the integral (C.5.4) factorize into a separate integral since they are independent of the surface profile. The remaining terms are

$$\begin{aligned}\langle I^2 \rangle = \langle I_S^2 \rangle + 4\,M(SA,SA,C,C) + 4\,M\big(S'B,S'B,C,C\big) + 2\,\Re e(M(SA,C,SA,C)) \\ + 2\,\Re e\big(M\big(S'B,C,S'B,C\big)\big) + M(C,C,C,C)\,,\end{aligned} \tag{C.5.6}$$

where additional simplification was made as the first and third (unconjugated) terms in M, or the second and fourth (conjugated) terms, can be exchanged:

$$M(F_1,F_2,F_3,F_4) = M(F_3,F_2,F_1,F_4) \tag{C.5.7}$$

and

$$M(F_1,F_2,F_3,F_4) = M(F_1,F_4,F_3,F_2)\,. \tag{C.5.8}$$

Finally it remains to write each term as a combination of the coherent field (the field measured when the boundary is a perfect planar interface), E_C, and combinations of G:

$$\begin{aligned}\langle I^2 \rangle = \langle I_S^2 \rangle \;&+\; 4\,\mathrm{G}(0,A,A^*)\;I_C - 4\,\mathrm{G}(2,B,B^*)\;I_C + 2\,\Re e\Big(\mathrm{G}(0,A,A)\;(E_C^*)^2\Big) \\ &-\; 2\,\Re e\Big(\mathrm{G}(0,B,B)\;(E_C^*)^2\Big) + I_C^2.\end{aligned} \tag{C.5.9}$$

Altogether (C.1.7), (C.4.3), (C.4.5), (C.5.3) and (C.5.9) allow for the scattered second intensity moment, $\langle I_S^2 \rangle / \langle I_S \rangle^2$ and the second intensity moment, $\langle I^2 \rangle / \langle I \rangle^2$, to be calculated for magnetic media under the Rice approximation.

Bibliography

[1] V.G. Veselago. The electrodynamics of substances with simultaneously negative values of ϵ and μ. *Sov. Phys. Usp.*, 10:509, 1968.

[2] J.B. Pendry. Negative refraction makes a perfect lens. *Phys. Rev. Letts.*, 85:3966, 2000.

[3] C.M. Soukoulis, S. Linden, and M. Wegener. Negative refractive index at optical wavelengths. *Science*, 315(5808):47–49, 2007.

[4] H.J. Lezec, J.A. Dionne, and H. A. Atwater. Negative refraction at visible frequencies. *Science*, 316:430–432, 2007.

[5] J. Yao, Z. Liu, Y. Liu, Y. Wang, C. Sun, G. Bartal, A.M. Stacy, and X. Zhang. Optical negative refraction in bulk metamaterials of nanowires. *Science*, 321:930, 2008.

[6] J. Valentine, S. Zhang, T. Zentgraf, E. Ulin-Avila, D.A. Genov, G. Bartal, and X. Zhang. Three-dimensional optical metamaterial with a negative refractive index. *Nature Letters*, 455:376–379, 2008.

[7] N. Garcia and M. Nieto-Vesperinas. Left-handed materials do not make a perfect lens. *Phys. Rev. Letts.*, 88:207403, 2002.

[8] Max Born and Emil Wolf. *Principles of Optics*. Cambridge University Press, 1995.

[9] J.A. Ferrari and C.D. Perciante. Superlenses, metamaterials, and negative refraction. *J. Opt. Soc. Am. A*, 26(1):78–84, 2009.

[10] J.B. Pendry. Negative refraction. *Contemporary Physics*, 45(3):191–202, 2004.

[11] G.W. 't Hooft. Comment on"negative refraction makes a perfect lens". *Phys. Rev. Letts.*, 87:249701, 2001.

[12] J. Pendry. Pendry replies: Comment on "negative refraction makes a perfect lens". *Physical Review Letters*, 87(24):249702, 2001.

[13] M. Nieto-Vesperinas. Problem of image superresolution with a negative-refractive-index slab. *J. Opt. Soc. Am. A*, 21:491–498, 2003.

[14] D.R. Smith R.A. Shelby and S. Schultz. Experimental verification of negative index of refraction. *Science*, 292:77–79, 2001.

[15] R.B. Greegor C.G. Parazzoli, K. Li, B.E.C. Koltenbah, and M. Tanielian. Experimental verification and simulation of negative index of refraction using snell's law. *Physical Review Letters*, 90(10):107401, 2003.

[16] A. Grbic and G.V. Eleftheriades. Experimental verification of backward-wave radiation from a negative refractive index metamaterial. *Journal of Applied Physics*, 92(10):5930–5935, 2002.

[17] N. Garcia and M. Nieto-Vesperinas. Is there an experimental verification of a negative index of refraction yet? *Optics Letters*, 27(11):885–887, 2002.

[18] S. Foteinopoulou, E.N. Economou, and C.M. Soukoulis. Refraction in media with a negative refractive index. *Physical Review Letters*, 90(10):107402, 2003.

[19] R.W. Ziolkowski and A.D. Kipple. Causality and double-negative metamaterials. *Physical Review E*, 68(2):026615, 2003.

[20] J. Brown. Artificial dielectrics having refractive indices less than unity. *Proceedings I.E.E.*, 100:51–62, 1953.

[21] D.R. Smith and J.B. Pendry. Homogenization of metamaterials by field averaging. *J. Opt. Soc. Am. B*, 23(3):391–403, 2006.

[22] G. Dolling, M. Wegener, C.M. Soukoulis, and S. Linden. Negative-index metamaterials at 780nm wavelength. *Optics Letters*, 32(1):53–55, 2007.

[23] J.B. Pendry, D. Schurig, and D.R. Smith. Controlling electromagnetic fields. *Science*, 312:1781, 2006.

[24] M. Rahm, D. Schurig, D.A. Roberts, S.A. Cummer, D.R. Smith, and J.B. Pendry. Design of electromagnetic cloaks and concentrators using form-invariant coordinate transformations of maxwell's equations. *Photonics and Nanostructures*, 6:87–95, 2008.

[25] Y. You, G.W. Kattawar, and P. Yang. Invisibility cloaks for toroids. *Optics Express*, 17(8):6591–6599, 2009.

[26] E. Cojocaru. Exact analytical approaches for elliptic cylindrical invisibility cloaks. *J Opt. Soc. Am. B*, 26:1119–1128, 2009.

[27] T. Chen and C. Weng. Invisibility cloak with a twin cavity. *Optics Express*, 17(10):8614–8620, 2009.

[28] J. Hu, X. Zhou, and G. Hu. Design method for electromagnetic cloak with arbitrary shapes based on laplace's equation. *Opt. Express*, 17(3):1308–1320, 2009.

[29] J. Hu, X. Zhou, and G. Hu. Design method for electromagnetic cloak with arbitrary shapes based on laplace's equation: erratum. *Opt. Express*, 17(15):13070–13070, 2009.

[30] Z. Ruan, M. Yan, C. W. Neff, and M. Qiu. Ideal cylindrical cloak: Perfect but sensitive to tiny perturbations. *Physical Review Letters*, 99(11):113903, 2007.

[31] S.A. Cummer, B. Popa, D. Schurig, S.R. Smith, and J.B. Pendry. Full-wave simulations of electromagnetic cloaking structures. *Physical Review E*, 74:036621, 2006.

[32] D. Schurig, J.J. Mock, B.J. Justice, S.A. Cummer, J.B. Pendry, A.F. Starr, and D.R. Smith. Metamaterial electromagnetic cloak at microwave frequencies. *Science*, 314:977–980, 2006.

[33] M. Yan, Z. Ruan, and M. Qiu. Cylindrical invisibility cloak with simplified material parameters is inherently visible. *Physical Review Letters*, 99:233901, 2007.

[34] P. Collins and J. McGuirk. A novel methodology for deriving improved material parameter sets for simplified cylindrical cloaks. *Journal of Optics A*, 11:015104, 2008.

[35] J. Li and J.B. Pendry. Hiding under the carpet: A new strategy for cloaking. *Physical Review Letters*, 101:203901, 2008.

[36] R. Liu, C. Ji, J.J. Mock, J.Y. Chin, T.J. Cui, and D.R. Smith. Broadband ground-plane cloak. *Science*, 323:366–369, 2009.

[37] J. Valentine, J. Li, T. Zentgraf, G. Bartal, and X. Zhang. An optical cloak made of dielectrics. *Nature Materials*, page NMAT2461, 2009.

[38] U. Leonhardt and T. Tyc. Superantenna made of transformation media. *New Journal of Physics*, 10:115026, 2008.

[39] B. Zhang, B. Wu, and H. Chen. Optical delay of a signal through a dispersive invisibility cloak. *Optics Express*, 17(8), 2009.

[40] A. Greenleaf, Y. Kurylev, M. Lassas, and G. Uhlmann. Electromagnetic wormholes and virtual magnetic monopoles. *Physical Review Letters*, 99(18):183901, 2007.

[41] H. Chen, B. Wu, L. Ran, T.M. Grzegorczyk, and J.A. Kong. Controllable left-handed metamaterial and its application to a steerable antenna. *Applied Physics Letters*, 89(5):053509, 2006.

[42] M. Rahm, S.A. Cummer, D. Schurig, J.B. Pendry, and D.R. Smith. Optical design of reflectionless complex media by finite embedded coordinate transformations. *Physical Review Letters*, 100(6):063903, 2008.

[43] Y. Lai, H. Chen, Z. Zhang, and C.T. Chan. Complementary media invisibility cloak that cloaks objects at a distance outside the cloaking shell. *Physical Review Letters*, 102(9):093901, 2009.

[44] Y. Lai, J. Ng, H. Chen, D. Han, J. Xiao, Z. Zhang, and C.T. Chan. Illusion optics: The optical transformation of an object into another object. *Physical Review Letters*, 102(25):253902, 2009.

[45] S.A. Ramakrishna and J.B. Pendry. Spherical perfect lens: Solutions of maxwell's equations for spherical geometry. *Physical Review B*, 69(11):115115, 2004.

[46] M.G. Silveirinha. Anomalous refraction of light colors by a metamaterial prism. *Physical Review Letters*, 102:193903, 2009.

[47] K.L. Tsakmakidis, A.D. Boardman, and O. Hess. 'Trapped rainbow' storage of light in metamaterials. *Nature*, 450(7168):397–401, 2007.

[48] N. Engheta. Circuits with light at nanoscales: Optical nanocircuits inspired by metamaterials. *Science*, 2007.

[49] P.C. Ingrey, K.I. Hopcraft, E. Jakeman, and O. French. Between right and left handed media. *Opt. Commun.*, 282:1020–1027, 2009.

[50] P.C. Ingrey, K.I. Hopcraft, O. French, and E. Jakeman. Perfect lens with not so perfect boundaries. *Optics Letters*, 34(7):1015–1017, 2009.

[51] O.E. French, K.I. Hopcraft, and E. Jakeman. Scattering by a left-handed particle on a left-handed slab or surface. *New Journal of Physics*, 9.

[52] L.D. Landau, E.M. Lifshitz, and L.P. Pitaevski. *Electrodynamics of Continuous Media*. Pergamon Press, second edition, 1984.

[53] John David Jackson. *Classical Electrodynamics*. Wiley, third edition, 1999.

[54] O.E. French, K.I. Hopcraft, and E. Jakeman. Perturbation on the perfect lens: the near-perfect lens. *New Journal of Physics*, 8:271, 2006.

[55] John Lekner. *Theory Of Reflection*. Martinus Nijhoff Publishers, 1987.

[56] N. Dalarsson, M. Maksimovic, and Z. Jaksic. A simplified analytical approach to calculation of the electromagnetic behavior of left-handed metamaterials with a graded refractive index profile. *Science of Sintering*, 39:185–191, 2007.

[57] N.M. Litchinitser, A.I. Maimistov, I.R. Gabitov, R.Z. Sagdeev, and V.M. Shalaev. Metamaterials: electromagnetic enhancement at zero-index transition. *Optics Letters*, 33(20), 2008.

[58] Milton Abramowitz and Irene A. Stegun. *Handbook of Mathematical Functions*. Dover Publications, 1965.

[59] U. Leonhardt. Notes on conformal invisibility devices. *New Journal of Physics*, 8:118, 2006.

[60] R. Ruppin. Surface polaritons of a left-handed medium. *Phys. Lett. A*, 277:61–64, 2000.

[61] J.B. Pendry and S.A. Ramakrishna. Refining the perfect lens. *Physica B*, 338:329–332, 2003.

[62] D.R. Smith, D. Schurig, M. Rosenbluth, S. Schulz, S.A. Ramakrishna, and J.B. Pendry. Limitations on subdiffraction imaging with a negative refractive index slab. *App. Phys. Letts.*, 82(10):1506, 2003.

[63] P.C. Ingrey, K.I. Hopcraft, and E. Jakeman. Negative refraction and rough surfaces: A new regime for lensing. *Optics Comms.*, 283:1188–1191, 2010.

[64] C.G. Parazzoli, R.B. Greegor, J.A. Nielsen, M.A. Thompson, A.M. Vetter K. Li, M.H. Tanielian, and D.C. Vier. Performance of a negative index of refraction lens. *App. Phys. Letts.*, 84:17, 2004.

[65] Y.A. Kravtsov and A.I. Saichev. Effects of double passage of waves in randomly inhomogeneous media. *Sov. Phys. Usp.*, 25:494–508, 1983.

[66] C. Macaskill. Geometric optics and enhanced backscatter from very rough surfaces. *J. Opt. Soc. Am. A*, 8(1):88–96, 1991.

[67] M. Pitter, E. Jakeman, and M. Harris. Heterodyne detection of enhanced backscatter. *Opt. Letts.*, 22:393, 1997.

[68] J.A. Ogilvy. *Theory of Wave Scattering from Random Rough Surfaces.* Adam Hilger, 1991.

[69] M.A. Dupertuis and M. Proctor. Generalization of complex snell-descartes and fresnel laws. *J. Opt. Soc. Am. A*, 11:3, 1994.

[70] E. Jakeman and K.D. Ridley. *Modelling fluctuations in scattered waves.* Taylor & Francis, New York, 2006.

[71] J.W. Goodman. *Statistical Optics.* Wiley and Sons, 2000.

[72] J.C. Dainty. *Laser speckle and Related Phenomena.* Springer-Verlag, Berlin, 1984.

[73] E. Jakeman, E.R. Pike, and P. Pusey. Photon correlation study of stellar scintillation. *Nature (Lond.)*, 263:215–216, 1976.

[74] R.P. Mercier. Diffraction by a screen causing large random phase fluctuations. *Proc. Camb. Phil. Soc.*, A58:382–400, 1962.

[75] P.C.Y. Chang, J.C. Flitton, K.I. Hopcraft, D. Jordan, and J.G. Walker. Importance of shadowing and multiple reflections in emission polarization. *Waves in Random Media*, 12:1–19, 2002.

[76] D. Courjon and C. Bainier. Near field microscopy and near field optics. *Rep. Prog. Phys.*, 57:989–1028, 1994.

[77] B. B. Baker and E. T. Copson. *The Mathematical Theory of Huygens' Principle.* Oxford, 1950.